UNIVERSITY OF CALIFORNIA

Santa Barbara

Dislocation Morphology and Mobility on the Slip Planes of Hexagonal Close-Packed Materials

A Dissertation submitted in partial satisfaction of

the requirements for the degree

Doctor of Philosophy in Materials

by

Claire Marie Albrecht

Committee in charge:

Professor Irene Beyerlein, Chair

Professor Matthew Begley

Professor Samantha Daly

Dr. Abigail Hunter, Los Alamos National Lab

September 2022

The dissertation of Claire Marie Albrecht is approved.

Professor Matthew Begley

Professor Samantha Daly

Dr. Abigail Hunter

Professor Irene Beyerlein, Committee Chair

August 2022

Dislocation Morphology and Mobility on the Slip Planes of Hexagonal Close-Packed Materials

Claire Marie Albrecht

typeset in LaTeX

Copyright Notice

Portions of this dissertation were reworked from our published research.

0.1 Elsevier

Section 1.1 and Chapter 2 on page 26 was reworked from our published research in the Journal of the Mechanics and Physics of Solids [1].

0.2 American Physical Society

Section 1.3 and Chapter 3 on page 71 was reworked from our published research in the Physical Materials Review Journal [2].

Acknowledgments

First and foremost, I give all thanks, glory, and honor to God, from whom all blessings flow, for the curiosity that motivates my research, for the gifts and abilities He's given me, for the patience and endurance required to complete this tremendous body of work through a global pandemic and family hardships. He has given me strength, peace, and encouragement throughout all the challenging moments of completing this dissertation. I am truly grateful for His unconditional and endless love, mercy, and grace.

As is the case with most graduate research, the results obtained during my time at UCSB were only made possible with the help of many brilliant and helpful scientists both inside and outside of UCSB. The collaboration between students, research groups, industry, and national laboratories is an invaluable asset of the UCSB scientific community. My development and research was greatly enriched with UCSB as my home institution.

I would like to sincerely thank my advisor, Dr. Irene J. Beyerlein, for coming to UCSB and enabling the world-class research performed throughout her group and collaborations, and for allowing me to be deeply involved in the development of the phase field dislocation dynamics (PFDD) model. Her renowned expertise and presence here at UCSB, drew in the world's top minds in PFDD modeling, who took sabbaticals here at UCSB, Dr. Bob Svensen and Dr. Abigail Hunter, who both contributed to my knowledge in important ways during their visits. Irene's collaborations with scientists at Los Alamos National Lab (LANL) also lead to my research being conducted there over the course of two summers under Dr. Abigail Hunter, who parallelized the PFDD model for faster, more powerful parallel processing, which was the version of the code I inherited at the start of this work.

I'd also like to thank collaborators Dr. Anil Kumar and Dr. Enrique

Matinez from LANL. Anil, for calculating the energy profiles, using density functional theory, for many of the materials and slip planes I then studied by inputting them into the PFDD model. Enrique, for coding the PFDD model, which was originally written in the C coding language, to C++, I especially have really benefited from going through the modular coding process together, which gave me a deeper understanding of the PFDD framework and it's capabilities. Our group now has two powerful PFDD codes with which to run simulations.

Professors Matthew Begley & Samantha Daly have positively challenged my understanding and provided helpful advice and direction during my preliminary and qualifying examinations, illuminating the path towards my defense. The professors in the structural group of the Material Science department have provided a broader scope of consideration for my research progress during my annual structural seminar presentations and have all contributed to my knowledge in important ways.

Being one of the first members in Irene's group and initially the only one to specialize in phase field dislocation dynamics (PFDD) modeling for the first couple of years, I am truly grateful for the addition of incoming students and post docs. The weekly group meetings have perhaps yielded some of the most fruitful insights. Members of the group also made significant contributions to the PFDD code development and capabilities. In particular, Dr. Shuozhi Xu added elastic anisotropy capabilities, coding the input of the full stiffness tensor and plane orientations into to the PFDD code. Lauren Fey formulated the Frank-Read source initialization set-up in the C++ PFDD code, which I coded into the C version of the PFDD code and used for much of my research. Morgan Jones and Ian Wise are the newest members of the PFDD group and my understanding has benefited greatly from teaching

them the PFDD model by putting together a summer PFDD workshop with Lauren Fey.

Of course, none of the acheivements made here would have been possible without support from the Department of Defense (DoD) through the National Defense Science & Engineering Graduate (NDSEG) Fellowship Program as selected by reviewers from the Air Force Research Lab (AFRL). Additional thanks to the Materials Science department for the block grant my first quarter at UCSB and to my advisor Dr. Irene Beyerlein, who funded the remainder of my graduate studies with an NFS grant.

Much credit goes to the world-class California NanoSystems Institute (CNSI) at UCSB, which houses the computer cluster BRAID on which I ran all of my simulations. The entire CNSI computing support staff are an invaluable resource. I'd like to give a very special thanks to the Co-Director Paul Weakliem, who taught me everything I now know about running simulations on a cluster. I had next to zero exposure to computational modeling when I came to UCSB and chose to focus on computational research. It was like flying to a foreign country without knowing any of the cultural practices or languages – Paul became my guide. He spent hours helping me troubleshoot every computing problem I encountered, from setting up my account, file transfers, installing the right compilers so the PFDD code would actually run, job submission, concatenating files, making sure I had job priority when I had deadlines coming up – the list goes on, needless to say, he was absolutely invaluable to me and performing my research, I could not have navigated the complexities of the computational world without him.

Penultimately, the fantastic community I have become involved in at Anthem Church, Isla Vista Church, and various connected ministries has really changed the way I experience life in Santa Barbara. Thank you God for

bringing me into such a beautiful community. Thank you to the Cohens and Struvens, for faithfully hosting the weekly young adults bible study, through which I have made some of my closest friends: Jesse, Justin, Johanna, Carly and Angelique. The Jesus Burgers home and ministry, special thanks to Courtney, Hannah, Emily, Jess, Bryanna, Matt, and Danny for their constant friendship and life giving conversations. Bonnie Johnson for discipling me. The Whaleys for opening their home as an office space from time to time while I worked on this dissertation. Mary and Rick Osgood for their warm meal ministry for the homeless in Isla Vista, I have been so rewarded by serving this amazing community of people. Azita and Demis John and their son Jacob, as well as Ethan Davis, for many good meals and conversations in their respective homes and at Mac 'n Jesus another warm meal ministry for the homeless. Special thanks to Demis for his mentorship as a fellow scientist and disciple of Christ, and for the template used to write this dissertation. And many more, who have all been extremely supportive.

Lastly, I would never have made it through graduate school without my extremely supportive family, who pray for me constantly and know how to pick me up every time I need encouragement. A big thanks to my mom + dad for their support on so many levels – more ways that I could count – but most recently for the regular texts and phone calls filled with love and encouragement that keep me on track. For my sisters Emmy and Tess, whose regular videos of my amazing nieces and nephews gave me the boost of dopamine to keep my brain going. And for my brothers Ryan and Jesse, who fuel the banter on the family group chat and kept me laughing. Thanks to my brothers-in-law Matt and Graham, my sister-in-law Karen, and my nieces and nephews Gabe, Gavin, Hudson, Evie, Veronica, Jude, and Gia for all the joy they have added to this family. My family has been my anchor

through life, especially in these last couple of years, I am filled with gratitude.

This dissertation is dedicated to my family:

My parents, Lynne & Rick Albrecht
My siblings, Tess, Emmy, Jesse, & Ryan

Vita of Claire Marie Albrecht

PERSONAL

Full Name: Claire M. Albrecht

Date of Birth: December 5, 1985, in Cincinnati, Ohio, United States

Nationality: United States of America

Email: claire_weaver@ucsb.edu (mail-forwarding address)

EDUCATION

Bachelor of Science in Physics, Physics Department, Hofstra University, Hempstead, New York, U.S.A., December 2015 (Summa Cum Laude)

Bachelor of Science in Applied Mathematics, Mathematics Department, Hofstra University, Hempstead, New York, U.S.A., December 2015 (Summa Cum Laude)

High School Diploma, Fairfield High School, Fairfield, Ohio, U.S.A., June 2004 (Summa Cum Laude)

CURRENT RESEARCH

Graduate Student Researcher–UCSB Materials department–Computational modelling with Professor Irene Beyerlein, 2016-present. Plasticity: Study of dislocation mediated plasticity in HCP materials. Computational: run parallelized Phase Field Dislocation Dynamics PFDD model on CNSI's Braid cluster, using zsh and bash shells, pbs job

submission script, and vi text-editor program. Advance PFDD model which is written C language to account for HCP crystallography, slip planes, and thermal fluctuations. Track and visualize data using excel, Matlab, Ovito, and Paraview. Write up and publish work using latex formatting language. Theoretical: parameterize HCP γ-surfaces and GSFE curves into equations for input into PFDD model. Derive Langevin force equations to model thermal fluctuations in PFDD model.

Graduate Computational Research Intern–Los Alamos National Laboratory (LANL) X Computational Physics Division–Computational modelling with Dr. Abigail Hunter, 2018. Computational: Development team for a modularized C++ PFDD code.

Graduate Computational Researcher Employee–Los Alamos National Laboratory (LANL) Theoretical Division–Computational modelling with Dr. Abigail Hunter, 2017. Computational: Learning and compiling the paralellized version of the PFDD code. Theoretical: Understanding the phase field framework, energetic contribution governing dislocation glide, the energy minimization equation (time-dependent Ginzburg Landau equation).

PAST RESEARCH

Undergraduate Nanofabrication Research Assistant–City University of New York (CUNY) Advanced Science Research Center–Nanofabrication Research with Dr. Jacob Trevino, 2015 - 2016. Nanoscience/Biophysics: assisted in the design and fabrication of microcone platforms that will

be tested with human oligodendrocyte progenitor cells (hOPCs) generated through the oligodendrocyte differentiation protocol. This is the first study that mimics the human myelination process in a dish. Trained in the nanofabrication process tools, including photolithography mask aligner (EVG620), 3D laser lithography (Nanoscribe Photonic Professional), and resist spin coaters (Brewer Science Cee Spin Coater). Nanophotonics/Nanoplasmonics: investigate the arrangement of metallic nano-cylinders in aperiodic spiral geometries for the enhancement of photonic-plasmonic coupling and increase light-matter interactions over broad frequency spectra. Trained in the nanofabrication process tools, including electron beam lithography (Elionix ELS-G100), scanning electron microscopy (FEI Nova NanoSEM) and sputter coating (Cressington 108 sputter coater).

Undergraduate Physics Research Assistant–Hofstra University Physics Department–Theoretical Research with Dr. Adam Durst, 2015. Theoretical Condensed Matter Physics: independent study of solid state physics, focusing on crystal structure and electronic band structure, based on the first half of Ashcroft Mermin. Worked examples for both nearly-free-electron and tight-binding analyses of electronic band structure; applied these techniques toward understanding a journal article about the electronic band structure of Bi2Se3, a topological insulator.

Undergraduate Experimental Research Assistant–Brookhaven National Laboratories, Superconductor Research with Dr. Meigan Aronson, 2014. Experimental Condensed Matter Physics: discovery and characterization of new compounds with strong electronic correlations using a variety of lab-based techniques. Focused on single crystal synthesis,

structure analysis, and preparations for characterization. Interested in compounds where different types of electronic order can be induced to occur exactly at zero temperature. Explored the unusual quantum critical phenomena associated with these T=0 phase transitions.

OTHER ACTIVITIES

Teaching Assistant–Defects in Engineering Materials Analysis ME125/225, UCSB Mechanical Engineering department–Professor Irene Beyerlein, 2021. Experience grading assignments and presentations, holding regular office hours, and giving lectures.

Grader–Mechanics and Measurements ME125/225, UCSB Mechanical Engineering department–Professor Sam Daly, 2017. Grader for assignments and exams.

PFDD Workshops, UCSB, 2019-2022. Develop and run PFDD workshops for visiting students and incoming new grad students in our group. Helping PFDD users set up all necessary accounts, compilers, and libraries necessary to run the code on their machine for their area of research.

Chapter President of the Society of Physics Students (SPS)–Hofstra University, 2014 - 2015. Launched a peer-mentoring program for all incoming Physics majors, which nurtured a sense of camaraderie within our community. Planned club events, including guest lecturers, seminars, faculty research presentations, undergraduate summer research presentations, astronomical observations, STEMinism conference at the Graduate Center in Manhattan, Conference for Undergraduate Women

in Physics (CUWiP) at Rutgers, and movie nights. Physics outreach within the Hofstra Community. Events were held at I.Fly Trapeze and Brooklyn Museum of Science.

Treasurer of Hofstra Astronomy Club, 2013 - 2014.

FELLOWSHIPS/AWARDS

National Defense Science and Engineering Graduate Fellowship (NDSEG), selected by Air Force Research Laboratory, 2017-2021.
https://tinyurl.com/NDSEG-fellow

2021 LMD Magnesium Technology Award–Best Poster Award–The Minerals, Metals Materials Society (TMS) international conference, 2020.
https://tinyurl.com/TMS-LMD-Award

City University of New York's Summer Undergraduate Research Program (C-SURP)–CUNY Advanced Science Research Center, 2015.

2015 Kirsten R. Lorentzen Award–National Society of Physics Students (SPS) and Association of Women in Science (AWIS)–given to an outstanding female in Physics.
https://www.spsnational.org/scholarships/lorentzen/recipients/2015
http://news.hofstra.edu/2015/08/17/physicsmath-major-receives-natl-award-for-women-in-science/

2015 James A. Moore Endowed Memorial Award–Hofstra University Physics and Astronomy Department–given to a physics major, showing the highest quality performance in course work, individual research and service to the Physics community as recommended by the faculty.

Summer Undergraduate Laboratory Internship (SULI) program–Brookhaven National Laboratory (BNL) and Department of Energy (DOE), 2014.

PUBLICATIONS

C. Albrecht, A. Kumar, S. Xu, A. Hunter, and I. J. Beyerlein, " Asymmetric equilibrium core structures of pyramidal-II c + a dislocations in ten hexagonal-close-packed metals ," *Phys. Rev. Mater.*, vol. 5, no. 4, p. 43602, 2021.

C. Albrecht, A. Hunter, A. Kumar, and I. J. Beyerlein, "A phase field model for dislocations in hexagonal close packed crystals," *J. Mech. Phys. Solids*, vol. 137, p. 103823, Apr. 2020.

Abstract

Dislocation Morphology and Mobility on the
Slip Planes of Hexagonal Close-Packed Materials

by

Claire Marie Albrecht

Hexagonal close packed HCP materials are already being widely used as structural materials in several key industries, and there is currently great interest in expanding their employment in many next-generation engineering applications. The use of HCP materials necessitates understanding and modeling their deformation response, whether in processing or in service. The plastic deformation response of materials with an HCP crystal structure is governed by the glide of dislocations on both low index and high index planes. For an HCP crystal, whether it deforms in a brittle or ductile manner depends on the relative amounts of moving dislocations contributed on these low index and high index planes. The ease of dislocation motion is largely a consequence of the characteristics of the dislocation core structure, such as number of planes on which it extends, whether it dissociates into smaller partial dislocations, its splitting distance, and the width of the individual partials. Therefore, understanding individual dislocations (at the nanoscale level) on the unique slip planes of HCP metals, sheds important insight onto the deformation of HCP materials.

Isolating individual dislocations is difficult to do experimentally and is

limited by length and time scales in many quantum/atomistic models. As such, we employ a phase field formulation that incorporates periodic potentials, from first principle calculations, to model individual dislocations on the distinct HCP slip planes. This work explores individual dislocations using the phase field dislocation dynamics PFDD model which had to go through several code developments to account for the lower symmetry of HCP crystallography and its unique slip plane energetics, elastic anisotropy, and thermal fluctuations. This work explores dislocation dissociation, morphology, and mobility on the basal, prismatic and pyramidal II slip planes in HCP materials, taking a special focus on the relatively unstudied pyramidal-II plane. 10 different HCP materials are modeled over the course of this work, but special attention is given to understanding dislocations in Mg for its promises in lightweighting applications, as well as Ti and Zr which are also commonly studied HCP materials. The temperature dependencies of dislocation glide are studied by the additional consideration of thermal fluctuations into the energy minimization framework of the model.

Since dislocation motion is largely a consequence of the characteristics of the dislocation core structure (number of planes on which is extends, whether it dissociates into smaller partial dislocations, its splitting distance, and the width of the individual partial cores) modeling dislocation dynamics in HCP requires a model that is capable of capturing these characteristics of dislocation core structure. Previously, the PFDD model was written for the symmetry of cubic crystal structures and had only been applied to face-centered cubic FCC materials. So for our work, the PFDD model is first extended to determine the static and dynamic properties of discrete dislocations belonging to all types of slip modes in the HCP crystal, such as the basal $\langle a \rangle$, prismatic $\langle a \rangle$, and pyramidal II $\langle c + a \rangle$ slip modes [1]. This is the first

time a phase-field based dislocation dynamics model has been used to model HCP materials, so we look at equilibrium dislocation cores and dislocation dissociation under no stress so we can compare our results with results from other atomistic models and experiments for validation. The dissociation simulations using the HCP capable PFDD method incorporate directly density functional theory DFT-calculated generalized stacking fault energy GSFE surfaces and curves for the different HCP slip planes and employ isotropic elasticity. The results demonstrated good agreement with available results from molecular statics MS, DFT, or experimental observations of dislocations structures in Mg.

We move forward into a deeper exploration of the pyramidal II plane, on which dislocation behavior remains elusive and the resulting material effects are unknown. We employ an elastically anisotropic version of the PFDD approach, to compute the equilibrium core structures of pyramidal-II $\langle c+a \rangle$ dislocations under zero externally applied stress conditions in ten HCP metals: Be, Co, Mg, Re, Ti, Zn, Cd, Hf, Y, and Zr. In all these metals, under zero applied stress, the initialized perfect $\langle c+a \rangle$ pyramidal dislocations dissociate into two partials that separate in plane, creating extended structures, with nanometer-sized splitting distances referred to as equilibrium stacking fault widths eSFW (that is the fully relaxed or equilibrated distance between partials under zero external applied stress). The eSFWs for these 10 metals scales inversely with their normalized intrinsic stacking fault energy I from their GSFE curves. In most cases, the dislocation partial core widths and Burgers vectors are not ideally equal. These asymmetries in the dislocation structures are explained by deviations in the pyramidal II GSFE landscape from that expected of a metal with an ideal c/a ratio and symmetric landscape. Metals with higher levels of elastic anisotropy have wider separation

distances (20–35%) for both screw and edge character dislocations than what would be expected with effective isotropic constants.

The discovery of the asymmetric dislocation cores on the pyramidal II plane prompted the following question: will the same energetics that result in asymmetric dislocation cores, also gives rise to asymmetric dislocation slip? We then applied an external shear stress that initiates dislocation glide along the slip plane of interest and note any changes in the splitting distances of the partial dislocations as they glide in tandem. If the partial dislocations and associated stacking fault glide while maintaining a consistent splitting distance between the two partial dislocations, we refer to this as the dynamic stacking fault width dSFW. We find glissile dislocations on the pyramidal II plane have dSFW that are directionally dependent. That is to say, if we apply a shear stress to initiate glide along one direction the measured dSFW differs from the dSFW measured when we apply a shear stress to induce glide in the opposite direction.The directional dependency of the dSFW is due to the asymmetries in GSFE curves and the decompostition of the Burgers vector for each partial dislocation. We explore this further by using a Frank-Read FR source to generate expanding dislocation loops. We calculate the critical shear stress σ_c for loop expansion for each FR source. We consider both screw and edge type initial dislocations in a FR source of different lengths on the basal and the pyramidal II plane and find the loop shape is dominated by screw type sections to minimize the line tension energy of the expanding loop. We also note large variations in the stacking faults throughout the FR loop expansion until the loop had expanded beyond its critical shape and a steady-state dSFW was reached. The evolution of the stacking faults during the FR dislocation loop expansion is due to the different energetic barriers to glide that governs each partial dislocation. Directional dependency is

also noticed for the FR source simulations of the pyramidal II plane, as the energetic barriers (e.g. from the asymmetric GSFE profile) associated with the leading and the trailing partial are "assigned" based on the directionality of the applied shear stress.

All of the simulations up to now are deterministic and carried out under an assumed temperature of 0K. However, the pyramidal planes are suspected to be temperature dependent more so than the other slip planes and many material processes and applications occur at or above room temperature. So in order to truly understand pyramidal II dislocation behavior we need to explore the temperature dependency of pyramidal slip. This necessitates the extension of the PFDD formulation to account for thermal activation. In our final PFDD development we derive the Langevin force equations for the phase field framework to account for thermal fluctuations at variable temperatures. This produces a stochastic thermal noise term that we can add to the energy minimization equation in the PFDD model. This advanced PFDD model with thermal capabilities is then used to explore how temperature affects the time to dislocation loop formation from a Frank-Read FR source. We study Mg, Ti, and Zr over various temperatures T ranging from $0 \leq T/T_m \leq 0.5$, where T_m is the melting temperature for each material. We also look at the velocity of infinitely long screw and edge type dislocations as they glide under the same shear stress we apply in the FR simulations. We find the leading partial for the screw dislocation "breaks away" at a greater velocity than the trailing partial at higher temperatures $T/T_m > 0.2$ creating a continuously growing stacking fault. We find that when we decrease the applied shear stress the leading screw partial does not breakaway at higher temperatures. This breakaway is not observed for the temperatures and stresses applied to edge dislocations. In the FR source simulations this results in the screw por-

tions "smearing" out at higher temperatures. This breakaway phenomenon observed on the pyramidal II plane is both dislocation character type, stress and temperature dependent.

Contents

Copyright Notice iv

0.1 Elsevier iv

0.2 American Physical Society iv

Acknowledgements vi

Vita of Claire Marie Albrecht xii

Abstract xviii

1 Introduction **1**

1.1 Motivated by light-weighting 1

1.2 Dislocations and stacking faults 3

1.3 Hexagonal close-packed crystallography 6

1.4 Promising ductility in slip activation on the pyramidal II plane 11

1.5 Temperature dependent deformation 16

1.6 Dissertation Outline 19

1.6.1 PFDD code development for HCP slip planes 20

1.6.2 PFDD application to R_e on pyramidal II plane in 10 HCP materials 21

1.6.3 Dynamics of dislocations in HCP 23

1.6.4 Thermally activated dislocation motion on the pyramidal II plane 24

2 Development of phase field model for dislocations in hexagonal close packed crystals 26

2.1 Methodology . . . 27

2.1.1 The Phase Field Approach for Dislocations . . . 27

2.1.2 PFDD extensions for HCP crystal structures . . . 31

2.1.3 DFT determined γ-surfaces and GSFE curves . . . 34

2.1.4 Lattice energy for the basal slip mode . . . 38

2.1.5 Lattice energy for prismatic and pyramidal II slip modes 44

2.2 Equilibrium dislocation structure . . . 46

2.2.1 Simulation configuration . . . 47

2.2.2 Dissociation on the Basal Plane . . . 51

2.2.3 Dissociation on the Prismatic Plane . . . 56

2.2.4 Dissociation on the Pyramidal-II Plane . . . 59

2.3 Summary . . . 65

2.4 Copyright . . . 68

Appendix . . . 69

2.A Grid spacing in HCP . . . 69

3 Asymmetric equilibrium core structures of pyramidal-II dislocations in ten HCP materials 71

3.1 Computational Methods . . . 72

3.1.1 DFT Methodology and Calculations . . . 72

3.1.2 PFDD formulation . . . 78

3.1.3 PFDD model for $\langle c+a \rangle$ pyramidal dislocations . . . 82

3.2 Results . . . 86

3.2.1 Disregistry across the core structure . . . 86

3.2.2 Be, Mg, Y . . . 89

3.2.3 Ti, Zr, Hf . . . 91
3.2.4 Re and Co . . . 93
3.2.5 Zn and Cd . . . 95
3.3 Discussion . . . 96
3.3.1 Scaling of core size with the intrinsic stacking fault energy 97
3.3.2 Origin of the asymmetric cores . . . 98
3.3.3 Effect of elastic anisotropy . . . 99
3.4 Conclusions . . . 105
3.5 Copyright . . . 106
Appendices . . . 107
3.A GSFE surface . . . 107
3.B Experimental elastic constants . . . 109
3.C Variation of R_e with the lower unstable stacking fault energy . 110
3.D Additional measures of elastic anisotropy . . . 110

4 Dynamic dislocation core structures in HCP materials 113
4.1 Directionally dependent dislocation glide on the pyramidal II plane . . . 114
4.2 Frank-Read source . . . 119
4.2.1 Basal dynamics . . . 121
4.2.2 Pyramidal II dynamics . . . 127
4.3 Summary . . . 137

5 Langevin thermal noise addition to the PFDD model 139
5.1 PFDD background . . . 140
5.2 PFDD formulation . . . 141
5.3 Langevin force equations . . . 144
5.4 Addition of thermal noise to the energy functional in PFDD . 146

5.5 Results . . . 149
5.5.1 FR simulation set-up . . . 150
5.5.2 Frank-Read results . . . 152
5.5.3 Straight edge and screw dislocations . . . 157
5.6 Conclusions . . . 158
Appendices . . . 161
5.A Steady-state time to loop formation . . . 161
5.B FR loop shape . . . 163

6 Conclusions **166**

7 Recommendations for future work **169**

References . . . 172

List of Figures

1.2.1 (a)Schematic of two common GSFE curve 4
1.3.1 HCP crystallography with slip planes and 7
1.3.2 GSFE curves of Mg for the basal, prismatic, ... 8
1.6.1 Multiscale modeling. PFDD bridges the scale 20

2.1.1 Comparison of γ-surfaces for the basal slip 41
2.1.2 Direct comparison of GSFE curves 43
2.2.1 Schematics showing (a) the initial simulation 48
2.2.2 Zoomed-in area of the slip plane showing the 49
2.2.3 Basal equilibrium stacking fault width 52
2.2.4 Prismatic equilibrium stacking fault width 56
2.2.5 Pyramidal-II equilibrium stacking fault width 60
2.2.6 Pyramidal-II GSFE curves for both Mg and 63
2.A.1 69

3.1.1 Comparison of GSFE profiles for (a) the 76
3.1.2 Schematics showing (a) the initial simulation 85
3.2.1 A schematic of the gradient of the order 87
3.2.2 The order parameter, ζ (dotted lines), and its 90
3.2.3 The order parameter, ζ (dotted lines), and its 93
3.2.4 The order parameter, ζ (dotted lines), and its 94

3.2.5 The order parameter, ζ (dotted lines), and its 96
3.3.1 The equilibrium partial separation distance 98
3.3.2 PFDD calculated SFWs (R_e) for edge (90 °) 101
3.3.3 The ratio of the anisotropic to the isotropic 104
3.A.1The standard (a) and relaxed (b) GSFE 107
3.C.1The equilibrium SFW R_e plotted against the 110
3.D.1The ratio of the anisotropic to the isotropic 112

4.1.1 The cross-section, showing the order 115
4.1.2 The generalized stacking fault energy GSFE 117
4.1.3 Snapshot of dislocation glide in Ti on the 118
4.2.1 The simulation setup for a Frank-Read source. 120
4.2.2 Screw, FR 20λ, +σ, basal plane in Mg. 123
4.2.3 Screw, FR 40λ, +σ, basal plane in Mg. 124
4.2.4 Edge, FR 20λ, +σ, basal plane in Mg. 125
4.2.5 Edge, FR 40λ, +σ, basal plane in Mg. 126
4.2.6 Screw, FR 20λ, +σ, pyramidal II plane in 129
4.2.7 Screw, FR 20λ, $-\sigma$, pyramidal II plane in 130
4.2.8 Screw, FR 40λ, +σ, pyramidal II plane in 131
4.2.9 Screw, FR 40λ, $-\sigma$, pyramidal II plane in 132
4.2.10Edge, FR 20λ, +σ, pyramidal II plane in Mg. 133
4.2.11Edge, FR 20λ, $-\sigma$, pyramidal II plane in Mg. 134
4.2.12Edge, FR 40λ, +σ, pyramidal II plane in Mg. 135
4.2.13Edge, FR 40λ, $-\sigma$, pyramidal II plane in Mg. 136

5.5.1 Schematic of the evolved, bowed-out 152
5.5.2 Snapshots of dislocation loops emitting from 154
5.5.3 The normalized time to loop formation for the 155

5.5.4 For each material Mg, Ti, and Zr we compare 156
5.5.5 The normalized velocity of edge and screw 157
5.A.1The normalized steady-state time to loop 162
5.A.2GSFE curves for Mg, Ti, and Zr. 163
5.B.1Snapshots of the complete dislocation loop 164
5.B.2Zr FR source at $T = 0K$, snapshots of the 165

List of Tables

2.1.1 Lattice constant (in Å) and elastic constants 38

2.1.2 Basal GSFE parameterization coefficients: 42

2.1.3 Prismatic and pyramidal-II GSFE 46

2.2.1 Basal equilibrium stacking fault widths in 55

2.2.2 Prismatic equilibrium stacking fault widths in 58

2.2.3 Pyramidal-II equilibrium stacking fault 61

2.2.4 The relationships between the absolute values 64

3.1.1 Number of valence electrons in 74

3.1.2 Lattice parameters (in Å) and elastic 75

3.1.3 The unstable SFEs, U_1 and U_2 and the 77

3.1.4 Interplanar spacing, d, normalized in terms of 83

3.2.1 The equilibrium SFW, R_e, the left and right 88

3.3.1 The ratio between the left and right partial 100

3.3.2 Log-Euclidean anisotropy index, A^L, ... 103

3.B.1 Experimentally determined elastic constants 109

3.D.1 Traditionally used anisotropic indices α, β, ... 111

5.4.1 Normalized quantities in the PFDD code. 149

5.5.1 Values used in PFDD. 150

Chapter 1

Introduction

1.1 Motivated by light-weighting

The world's pursuit of improved fuel efficiency has generated an interest in materials light weighting. This search for advanced materials with low density and high strength has focused attention on several promising hexagonal close packed (HCP) structured materials, specifically magnesium (Mg). This work will at times consider many HCP materials, but Mg will be a primary focus for examples throughout this work due to it's potential benefits in light-weighting applications and thus being one of the most studied HCP materials. Mg and its alloys have densities that are approximately two-thirds that of aluminum (Al) alloys and one-quarter that of steel [8]. The replacement of these prolifically used structural materials with Mg alloys results in a significant weight reduction. As such, Mg is the focus of light-weighting within the automotive and aerospace industries [9]. The reduction in weight of cars and airplanes would lead to a notable improvement in their fuel economy. Thus, future implementation of these Mg alloys in transportation methods on a global scale would result in a dramatic decrease in the world's energy

consumption, independent of the energy source (i.e. fossil fuels, solar, etc.). Additionally, Mg has full recyclability, thin wall capability, corrosion resistance, radiation resistance, resilience at high operating temperatures, biocompatibility, and is the 8^{th} most abundant element in the earth's crust, as well as trillions of tonnes of Mg in the oceans, from which most of the 850,000 tonnes/year are produced. So while advances are continually updating the latest in energy production and storage to reduce our dependency on fossil fuels and lower our carbon foot print, Mg-based alloys have the potential to be a long term and sustainable partner to any energy source, acting as a multiplier for many other energy reduction strategies.

According to a review by Yang et al. (2008) more than 90% of Mg-based alloy structural components are produced via casting process [10], which is far more energetically and cost expensive than the current production processes employed for most structural components in the car and aerospace industry i.e. cold-rolled Al-alloy sheet metal. Unfortunately, to this day sheet Mg is still hindered by poor room temperature formability, ductility, and it's highly anisotropic mechanical behavior; it is too brittle to be implemented in the wider structural applications of sheet Mg. In a 2014 paper by Sandlobes et al. it is shown that pure Mg deforms via strain localization into macro shear bands, along which early cracking occurs. These bands act as soft zones for dislocations to move quickly along like a dislocation highway as deformation proceeds [11]. Pure Mg completely fractures along these macroscopic shear bands after as little as a 20% reduction in thickness via cold-rolling. Plastic deformation in metals is mediated by dislocation nucleation, mobility, and interactions. Ductility is a slip sensitive property, which is governed by interactions between dislocations with other dislocations, stacking faults, solutes, grain boundaries, and other micro-structures. Thus, the development

of Mg alloys with ductility enhancement requires fundamental studies of dislocation energetics, nucleation, multiplication, dissociation, and annihilation processes, all of which behave differently in the unique HCP crystal lattice structure.

1.2 Dislocations and stacking faults

Dislocations are an important type of extended linear defect in the atomic lattice of a material. They are characterized by their orientation within the crystal structure, called the line sense, with respect to the magnitude and direction of the lattice distortion due to the presence of the dislocation, called a Burgers vector, $\vec{b}$. The lattice distortion due to the presence of a dislocation produces a stress field that depends on the character of the dislocation and the material. When the line sense and Burgers vector are parallel they are characterized as being a screw type dislocation, when they are perpendicular they are characterized as an edge type dislocation, and when the angle between the two is somewhere between 0° and 90° the dislocation is characterized as being of mixed character. The stress field around a dislocation produces interaction forces between other dislocations, defects, solutes, grain-boundaries and various other micro-structures. As such, dislocations are closely related to the plastic mechanical properties exhibited by a material (i.e. formability, ductility, strength). For this reason, there are many experimental and computational studies that focused on achieving a better understanding of dislocation slip and the deformation mechanisms.

Dislocation behavior (i.e. glide, core shape, dissociation into partials) depends on the energetics of it's slip system, which describes the set of sym-

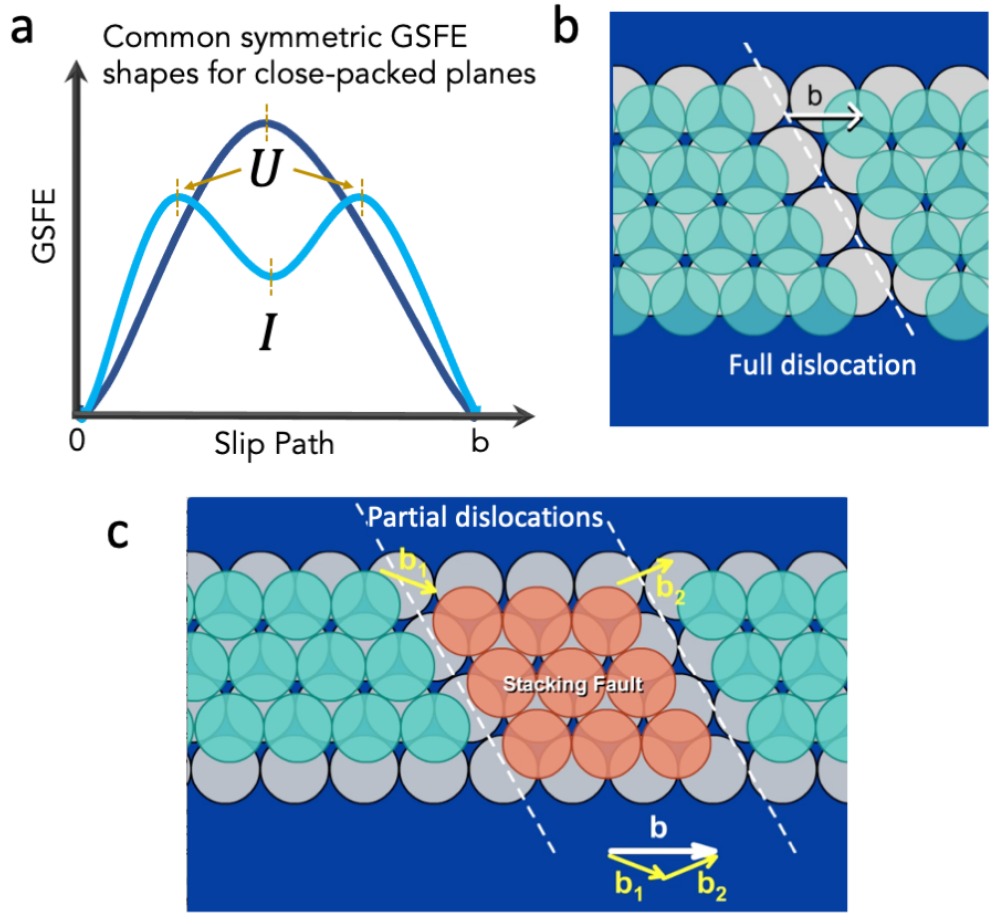

Figure 1.2.1: *(a)Schematic of two common GSFE curve shapes for a close-packed plane common in FCC and HCP materials (See Figure 1.3.1 (a) to see the close-packed planes of HCP). They are symmetrical with global minima at neighboring direct lattice sites a Burgers vector, b, apart. Notice the different critical energy points on each, one has only one unstable stacking fault energy, U, which means that it is more energetically favorable for the dislocation core to remain compact (as shown in (b)), while the other has two unstable stacking faults energies on either side of an intrinsic stacking fault energy, I, which indicates it is more energetically favorable for a dislocation to dissociate into two partial dislocations with an associated stacking fault in between (as depicted in (c)). Figures (b) and (c) are adapted from www.princeton.edu/∼maelabs/mae324/07/07mae_52a.htm*

metrically identical slip planes and the associated family of slip directions on which dislocation motion occurs. The full energetics of a slip plane containing one or more slip directions can be described by an energy landscape known as a γ-surface. The γ-surface is usually generated via ab initio methods by measuring the energy penalty between two adjacent slip planes during shear deformation in several directions mapping out the energetic surface of a given slip plane.

A dislocation's slip direction will follow the lowest energetic path. This energetically favorable cross-sectional path of the γ-surface is referred to as the generalized stacking fault energy (GSFE) curve. The GSFE curve begins and ends at neighboring direct lattice site that correspond to the Burgers vector displacement, but does not necessarily run parallel to the Burgers vector, as we will see on the basal plane in HCP materials. GSFE curves contain important energetic points (see Figure 1.2.1): (i) the unstable stacking fault energy, U, which is a local or global maximum and is the energetic barrier to dislocation glide and (ii) the intrinsic stacking fault energy, I, which is a local minimum and is an indication that a dislocation will dissociate into partial dislocations, forming a stacking fault in between (as shown in (c)). The Burgers vectors of the partial dislocations are a linear combination of the Burgers vector for the full dislocation (as is shown in (b,c)).

The stacking fault width is both slip plane and material dependent and is the result of balancing energies. Because of the local minimum in the GSFE curve along the slip path, it is energetically more favorable for a full dislocation to dissociate into two partial dislocations.

$$E_{full} > 2\,E_{partial} \tag{1.2.1}$$

Dislocations with like signed Burgers vectors (i.e. like the Burgers vectors

for the partial dislocations) repel one another reducing the elastic interaction (strain) energy, which is inversely proportional to the distance d between the two.

$$E_{disl-disl} \propto \frac{1}{d} \tag{1.2.2}$$

it is energetically favorable for partial dislocations to glide apart, however this comes at the expense of the stacking fault energy penalty. Every atom within the stacking fault is no longer at a direct lattice site with zero energy and incurs an energy penalty of I from the GSFE curve. Thus the energy penalty of the stacking fault scales with the area of the stacking fault.

$$E_{SF} \propto Area_{SF} \tag{1.2.3}$$

The balance of these three energies under no external stress produces what we refer to as an equilibrium stacking fault width eSFW. This eSFW is slip plane and material specific. Under an applied stress we refer it as a dynamic stacking fault width dSFW. We will explore these further in later chapters.

See Figure 1.3.1 which shows the unique slip planes in the HCP unit cell and Figure 1.3.2 to see corresponding GSFE curves for these planes in Mg.

1.3 Hexagonal close-packed crystallography

The plastic deformation response of materials with a hexagonal close packed (HCP) crystal structure is governed by the glide of dislocations on both low index and high index planes [12]. Each mode of slip is defined by the specific slip plane and slip direction of these dislocations [12, 13] (See 1.3.1). For an HCP crystal, whether it deforms in a brittle or ductile manner depends on the relative amounts of moving dislocations contributed by each mode [14]. The ease of dislocation motion is largely a consequence of the characteristics of

the dislocation core structure, such as number of planes on which it extends, whether it dissociates into smaller partial dislocations, its splitting distance, and the width of the individual partials.

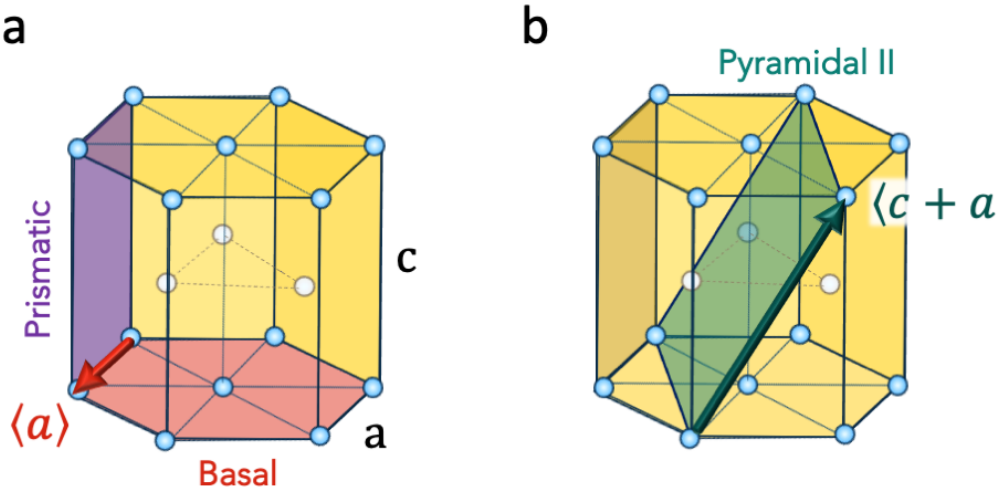

Figure 1.3.1: *HCP crystallography with slip planes and Burger vectors. a) Basal and prismatic plane both have an $\langle a \rangle$-type dislocations and can thus only produce deformation in the closed pack plane along the a-axes directions. b) Pyramidal II plane contains $\langle c + a \rangle$-type dislocations, which can accommodate deformation along the c-axis direction.*

For HCP crystals, the structure of the dislocation core depends on the type of glide plane and Burgers vector, the elastic strain, and the strain energy that the dislocation core generates in the surrounding material outside the core region. Most dislocation cores can be described as being dissociated into partial dislocations with a smaller Burgers vector and a stacking fault in between [12, 15, 16, 17]. The spreading distance between the partials is governed primarily by the balance between the interaction strain energy between the partials and the energy required to form or grow the stacking

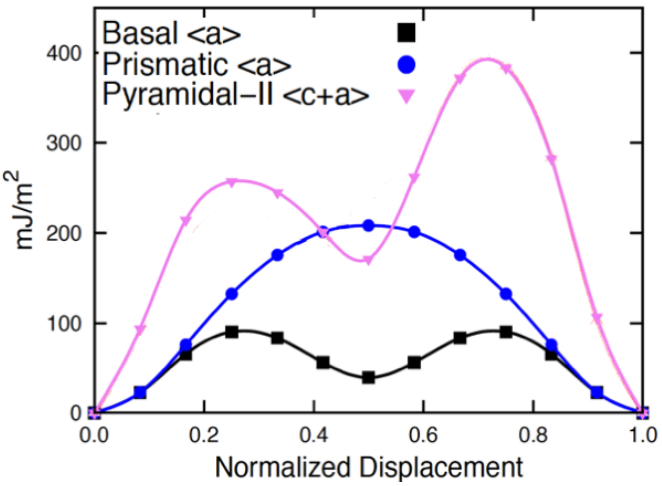

Figure 1.3.2: *GSFE curves of Mg for the basal, prismatic, and pyramidal II planes. The x-axis is normalized by the respective Burgers vector for each plane. From the critical energy points we can determine that dislocations on the prismatic plane will remain compressed, which dislocations on the basal and pyramidal II plane will dissociate into two partial dislocations, forming a stacking fault.*

fault [18]. For the HCP Mg crystal, recent density functional theory (DFT) and Molecular Dynamics (MD) studies have calculated the core structures of dislocations of edge and screw character belonging to the basal $\langle a \rangle$, prismatic $\langle a \rangle$, and pyramidal $\langle c + a \rangle$ modes [15, 16, 19, 20]. They are all shown to be planar, with the partials and associated core displacements predominantly acting in the slip plane. The basal $\langle a \rangle$ dislocation dissociates into two partials with an intrinsic stacking fault in between, the prismatic $\langle a \rangle$ dislocation remains compact, i.e., undissociated, and the pyramidal $\langle c + a \rangle$ dislocation splits into two partials of equal Burgers vector separated by a stacking fault. For other structurally relevant metals, such as HCP Ti and Zr, far fewer

DFT and MD studies on core structures currently exist [21, 22, 23, 24].

Apart from core structures, atomistic simulations have been successful in modeling the motion of individual HCP dislocations [25, 26]. Due to size limitations, the dynamics of dislocations have not been simulated by DFT. MD, given an interatomic potential, has been used to study the motion of a wide range of HCP crystals, such as Mg and Mg alloys, Zr, and Ti [16, 17, 20, 21, 26, 27]. Yet still, it is widely recognized that length and time scale limitations prevent the study of traditional size crystals ($>$ microns) and typical laboratory test conditions ($> 10^{-3}$/s). These limitations also make it prohibitive to model collections of dislocations.

As an alternative to atomic-scale simulations are continuum mechanics models that attempt to model directly an individual dislocation or dislocations moving on specific planes. These models are often referred to as mesoscale models, due to the length and/or time scales of the phenomenon they model as opposed to the theory or formulation on which they are based. The discrete dislocation dynamics (DDD) technique is one such example and has, for several decades, proven to be a powerful and effective tool for modeling from a few to several hundreds of individual dislocations, propagating within a number of crystal structures, including HCP crystals [28, 14]. However, in DDD, dislocations are modeled as linear objects and the structure of the dislocation core is not resolved. Another class of continuum models are Peierls-Nabarro (P-N) models, or more recently generalized PN models (GPN), that calculate core structures of dislocations based on minimizing the elastic strain and lattice energies. But to date, these have been applied mostly to face-centered cubic (FCC) and body-centered cubic (BCC) crystals, with exception of [29], which investigated dislocations lying in the basal plane in Mg.

A third type of continuum mechanics models are those that adopt the framework of phase field (PF) theory and apply it to simulate the motion of discrete dislocations in single and polycrystalline systems [30, 31, 32, 33]. Traditionally, PF theory has been used to predict the temporal and spatial evolution of domain structures, whose distinguishing property is indicated by a set of order parameters, ζ (e.g., representing solute concentration, atomic order, polarization, dislocation slip) [31, 33, 34, 35]. In PF-based discrete dislocation modeling, the general free energy density E of Cahn and Hilliard (1958) [36] is made to depend on the total strain energy and stacking fault energy (SFE). The phase field order parameter, ζ_α, corresponds to the crystallographic shift caused by a gliding dislocation on the slip plane α. A coupled set of time-dependent Ginzburg-Landau equations is then employed to solve for ζ_α, at every time step. Accordingly, with this methodology, the values of ζ_α correspond to non-negative dissipation and gradient flow toward thermodynamic equilibrium. Like DDD and P-N/GPN models, PF dislocation mechanics models have primarily been employed to study dislocations in FCC crystals. Recent application of the PF approach to dislocation processes has seen treatment of the nucleation and motion of defects, such as dislocations and twins, and their interactions with surfaces, boundaries, and interfaces in FCC single crystals and polycrystalline materials [37, 38, 31, 32, 39]. Only recently has PFDD been applied to BCC crystals, to study misfit dislocations in a BCC twist boundary or anisotropy in loop expansion under stress [40, 41]. For glide processes relevant to HCP stacking, a few notable exceptions are the work by [42], who investigated the transition of the FCC to HCP structure via the glide of FCC Shockley partial dislocations, and by [43], who recently modeled slip transmission of Shockley partial dislocations on the basal plane in a Ti alloy across an HCP/BCC interface.

Reference Section 1.6.1 outlining our work studying these unique HCP slip planes by building upon the 3D phase field dislocation formulation, called phase field dislocation dynamics (PFDD).

1.4 Promising ductility in slip activation on the pyramidal II plane

Hexagonal close packed (HCP) materials are already being widely used as structural materials in several key industries, and there is currently great interest in expanding their employment in many next-generation engineering applications. HCP Hf, Zr, and Be and their alloys are frequently used in many nuclear and defense industries [44, 45, 46, 47]. In the biomedical industry HCP Ti and Zr and their alloys have long been the materials of choice, but additional alloys of Mg and Zn currently being considered [48, 49]. Many HCP Co-based alloys are in development for use in newer high-temperature aerospace applications [50, 51]. Employment of HCP materials in these technologies necessitates understanding and modeling their deformation response, whether in processing or in service.

With respect to the HCP lattice, HCP materials slip easiest in their compact $\langle a \rangle$ direction on their compact planes, either basal or prismatic. Deformation in their $\langle c \rangle$ axis requires pyramidal $\langle c+a \rangle$ slip, which is more difficult, and the degree of plastic ansitropy scales with the difference in activation energies between $\langle a \rangle$ slip and pyramidal $\langle c+a \rangle$ slip modes [52, 53, 54, 55, 56, 57, 58]. Another inelastic mode of deformation that occurs easily in HCP materials is deformation twinning and it competes directly with pyramidal $\langle c+a \rangle$ slip in accommodating $\langle c \rangle$ axis deformation [59, 49]. Ductility of HCP metals is thought to be limited by plastic anisotropy and/or

deformation twinning [58]. Therefore, enabling wider use of HCP metals and improving ductility resides in understanding pyramidal $\langle c+a \rangle$ slip [60, 61, 62, 12].

Pyramidal $\langle c+a \rangle$ dislocations can be difficult to move due to the combined effect of a relatively large Burgers vectors (36–46% longer than $\langle a \rangle$ Burgers vectors) and some atomic shuffling, as a consequence of the atomically rumpled pyramidal plane [12, 15]. Based on Frank's rule, it is energetically preferable for a full $\{\bar{1}\bar{1}22\}$ $\langle c+a \rangle$ dislocation to dissociate into two equal partial dislocations rather than remain whole by the following reaction [12]:

$$\frac{1}{3}[2\bar{1}\bar{1}3] \rightarrow \frac{1}{6}[2\bar{1}\bar{1}3] + \frac{1}{6}[2\bar{1}\bar{1}3] \ . \tag{1.4.1}$$

The products of this reaction, the two like-signed partials, repel. In their attempt to glide away, their motion is limited by the stacking fault they create across the glide plane. Their equilibrium separation R_{e} can be estimated by a balance of their repulsive interaction energy and penalizing energy of their stacking fault in between them [63]:

$$R_{\mathrm{e}} = \frac{Kb^2}{8\pi I} \tag{1.4.2}$$

where b is the magnitude of the Burgers vector of the undissociated, compact dislocation, I is the intrinsic stacking fault energy (SFE), and K is the anisotropic energy factor from Ref. [4], which depends only on dislocation character and the five independent elastic constants.

The extent of the stacking fault R_{e} plays an important role not only in the partial dislocation mobility, but also in key dislocation-based processes, such as grain boundary migration, interactions between grain boundaries and interfaces, dislocation network formation, and dislocation-dislocation reactions [64, 65, 66, 67, 57]. They may be responsible for the choice of prevalent dis-

location reactions, preferred glide planes, and mechanisms for overcoming obstacles, such as cross slip or climb [68, 69, 70, 71]. Dislocation theory and atomistic simulations suggest that dissociation of dislocations with relatively large Burgers vectors, such as pyramidal dislocations, can play a role in twin embryo formation or twin boundary migration in HCP metals [72, 13, 73, 74].

The dissociated core structure of the pyramidal-II $\{\bar{1}\bar{1}22\}$ plane is, in part, a consequence of its complex fault energy landscape, the energy associated with shearing across the glide plane. The energy along the $\langle 11\bar{2}3\rangle$ slip direction, called the generalized stacking fault energy (GSFE) curve, has a single local minimum corresponding to I. The displacement, x_I, to reach this local minimum is related to the Burgers vector of the partials. Density functional theory (DFT) calculations for the GSFE curve on the pyramidal-II plane have been reported in a number of works for Mg [17, 15, 75], Ti [17, 1, 76], Zr [17, 1, 77], as well as Cd, Zn, and Re [17]. For Mg, Dou et al. [75] studied the peaks and valley in the relevant displacement path, finding that the two peaks were unequal and the local minimum I does not occur at half shift between stable points. The asymmetry suggests asymmetric split of the perfect dislocation and overall core structure, deviating from the geometric model in Equation 1.4.2. Recent DFT work on Mg, as well as the other metals Zr, Ti, Cd, Zn, and Re, noted similar asymmetries, but further indicated that these asperities varied with the metal [1, 17, 77]. Kumar et al. [15, 78] demonstrated that allowing for additional relaxations, during the calculation of the pyramidal GSFE curve, caused changes in the peaks and local minimum and the displacements needed to achieve them. In the case of pyramidal-II in Mg, the displacement shift became closer to $0.5b$, and consistent with Equation 1.4.2. They explained that for the pyramidal planes in Mg and Zr additional atomic shuffles were needed to reach the lowest energy

minimum state. The same was not true for the basal or prismatic planes, whose atomic structures are flat and symmetric about the glide direction. However, for other metals, curves from fully relaxed DFT calculations still show that an asymmetry persists [78, 17].

A few experimental studies have identified moving or dissociated $\langle c+a \rangle$ dislocations in Mg, otherwise identification or characterization of dislocation cores is challenging and requires high resolution microscopy. Slip trace analyses of deformed Mg and Mg alloy crystals have provided evidence of profuse pyramidal slip [54, 56, 52, 79, 80]. *In-situ* microscopy in nanocrystalline Mg witnessed pyramidal slip dislocations in motion [58]. Early room temperature experimental observations from transmission electron microscopy (TEM) by Stohr and Poirier [81] reported that pyramidal dislocations are dissociated into two equal length $(1/2)\langle c+a \rangle$ dislocations, in agreement with the analytical picture in Equation 1.4.1. More recently high-resolution TEM (HR-TEM) studies revealed the stabilization of a single $(1/2)\langle c+a \rangle$ partial dislocation on the pyramidal-II $\{\bar{1}\bar{1}22\}$ plane [15].

In addition to the $\{\bar{1}\bar{1}22\}$ plane, pyramidal $\langle c+a \rangle$ dislocations can possibly glide on the first-order $\{\bar{1}\bar{1}01\}$ pyramidal plane. The preferred pyramidal plane for a given HCP material currently relies on experimental observation and is not yet understood. Second-order (or type II) pyramidal glide is commonly expected in most HCP metals with the exception of Ti and Zr. However, pyramidal type II has been observed in Zr [82, 83, 84] and Ti [85, 86], while the other type I glide has been reported more recently in Mg [87, 88, 80].

Computational studies of dislocation core structures have been carried out via a number of methods. The large size of Burgers vectors most often limits application of DFT for calculating the equilibrium core structures of pyrami-

dal dislocations. The relatively larger length scales accessible with molecular dynamics methods makes it suitable; however, the largest body of work to date focuses on the one HCP metal, Mg, for which interatomic potentials have been developed specifically for studying defects. Alternatively, a number of continuum models based on continuum mechanics, such as the phase-field microelasticity (PFM) [89], phase-field dislocation dynamics (PFDD) [90], semidiscrete variational [91], and generalized Peierls-Nabarro (GPN) models [92], have been employed to compute dislocation core structures. They are formulated to capture long-range stress fields of dislocations, while sacrificing atomic-scale physics and fidelity. This class of models are developed primarily for simulating dislocation processes, involving one or more discrete dislocations, and their application to core structures is one problem they share with *ab initio* and atomistic methods [90, 93].

The PF-based methods and GPN models minimize an energy functional at every point in the system and the order parameters are usually chosen to identify a slipped phase and un-slipped phase. Dislocation core structures are calculated by relating discrete atomic displacements with a continuum disregistry field. The input parameters for the energies associated with these displacements can be obtained from *ab initio* calculations, experimental measurements, molecular dynamics, or molecular statics (MS), provided that reliable potentials exist [94]. In Chapter 2 the PFDD model is extended to determine the static and dynamic properties of discrete dislocations belonging to all types of slip modes in the HCP crystal, such as the basal $\langle a \rangle$, prismatic $\langle a \rangle$, and pyramidal $\langle c + a \rangle$ slip modes [1]. Previously, the PFDD methodology was predominantly applied to dislocations in materials with cubic crystal structures, namely face-centered cubic (FCC) [94, 95, 31], and body-centered cubic (BCC) [41, 96] structures. The dissociation simulations

using the HCP PFDD method incorporated directly DFT-calculated GSFE surfaces and curves for the different HCP slip planes and employed isotropic elasticity [1]. The results demonstrated good agreement with available results from MS, DFT, or experimental observations of dislocations structures in Mg. Moving forward into a deeper exploration of the pyramidal II plane, we employ an elastically anisotropic version of the PFDD approach, developed in Reference [95], to compute the equilibrium structures of pyramidal-II $\{\bar{1}\bar{1}22\}\langle 11\bar{2}3\rangle$ dislocations in ten HCP metals: Be, Co, Mg, Re, Ti, Zn, Cd, Hf, Y, and Zr (See Section 1.6.2).

1.5 Temperature dependent deformation

With the incredible advances in computational and experimental capabilities, the constant pursuit of structural materials exhibiting high strength-to-weight characteristics has lead researchers to return their attention to Mg and its alloys in hopes to elucidate the half a century old, unresolved questions surrounding its plasticity. In addition to being the lightest structural metal, Mg has been shown to exhibit a high damping capacity [97] as well as excellent fatigue resistance [98]. One of the main technical challenges, limiting the structural applications of Mg alloys, is the need to improve the strength and creep resistance at elevated temperatures [99]. Surprisingly, the number of studies that report on the thermo-mechanical response of Mg and its alloys, is only a small fraction compared to other metallic alloys. As a result, there remain many open questions regarding the effects of temperature on the deformation of Mg and its alloys that have yet to be addressed.

Crucial insight into expanding structural manufacturing capabilities and improving the formability of Mg and Mg alloys at higher temperatures may

come from understanding the plastic deformation mechanisms in Mg at elevated temperatures. The HCP lattice structure of Mg induces high anisotropy, which results in low formability at room temperature, making plastic working of Mg and Mg alloys difficult [100]. In the 1960s Wonziewicz and Backofen [101] studied the plain strain compression of four hard orientations of bulk Mg single crystals at various temperatures from room temperature to 307 °C, and have shown a strong temperature dependence on the critical resolved shear stress (CRSS) for non-basal slip (e.g. prismatic and pyramidal $\langle c+a \rangle$ slip). Interestingly, in 2001 Yoo et al. [66] reported an anomalous increase in the CRSS of pyramidal $\langle c+a \rangle$ slip during c-axis compression of single crystals at $T_H \sim 0.4$ (T_H is the homologous temperature defined as the material temperature, T, divided by the melting temperature, T_m). Furthermore, in addition to this thermal-hardening, in 2010 Ando et al. [102] reported a decrease in ductility with an increase in temperature. These contradictory observations are indicative of a transformation in deformation modes at elevated temperatures and merits further investigation. There is clearly a need for a more systematic study of the temperature effects on various slip systems in Mg (and other HCP materials).

The mechanical behavior of HCP metals is determined by the core structures and energies of dislocations and planar defects, including twin boundaries and stacking faults. The variety of possible structures, along with the corresponding energetics, for these defects results in several competing deformation modes. The shortest Burgers vector in HCP cyrstallography, $\mathbf{b} = \langle a \rangle = 1/3 \langle 11\bar{2}0 \rangle$ lies on the primary slip system, either on the basal plane for Mg, Be, Cd, and Zn, or on the prismatic plane in Ti, Zr, and Hf. Non-basal slip with a Burgers vector of $\mathbf{b} = \langle c+a \rangle$ on the pyramidal plane provides a secondary or an additional slip system. The low crystal symme-

try of HCP materials limits the number of active independent slip systems, which necessitates that twinning deformation be activated especially at and below room temperature, where non-basal slip is restricted due to its high CRSS [60]. It is also observed that sensitivity of non-basal dislocation slip to temperature is high, while that for deformation twinning is much lower [103, 104, 105]. Some HCP metals, like Ti and Zr, have exhibited deformation by mechanical twinning far more readily than in Mg and Be [60]. As a result, different HCP materials have dramatically different mechanical properties, particularly in single-crystal deformation [99, 106]. In the case of Mg, twins formed by c-axis compression are all very thin and do not seem to contribute very much to the ductility [107]. In general HCP metals show unlimited ductility at high temperatures, but the contribution of twinning decreases with increasing temperature [107]. Therefore, it is highly probable that some slip system (the pyramidal $\langle c+a \rangle$ plane) is active in Mg, giving c-axis deformation, and its ductility strongly depends on this deformation mechanism [107]. It is also observed that sensitivity of non-basal dislocation slip to temperature is high, while that for deformation twinning is much lower [103, 104, 105]. Therefore, at elevated temperatures, the CRSS for dislocation mediated plasticity becomes lower than that for deformation twinning [99, 104, 105]. As a result, non-basal slip is expected to be activated at elevated temperatures and provide sufficient slip systems for arbitrary shape change [66]. Despite this diverse behavior, little is understood mesoscopically about the mechanisms of non-basal deformation modes, specifically $\langle c+a \rangle$ dislocation slip on the pyramidal plane at high enough temperatures to influence plasticity and their impact on material properties. The thermo-mechanical responses in HCP materials will be broken down and further explored in two chapters. Chapter 4 explores the deterministic dynamics of dislocation mobility at 0K.

And in Chapter 5 we add stochastic thermal considerations.

1.6 Dissertation Outline

This work follows the evolution and application of the phase field dislocation dynamics (PFDD) model, through several stages of development to accommodate: i) the dislocation-governing energetics of the lower symmetry HCP crystallography with its unique slip planes, ii) the full stiffness tensor to account for elastic anisotropy in a material, and iii) the addition of a Langevin force term to the PFDD formulation to account for the thermodynamic driving forces on dislocation behavior in a material at variable temperatures.We will be using the PFDD model for simulations on the microscale, however the model is capable of reaching mesoscopic lengths and timescales (See Figure 1.6.1). Each chapter covering the stages of the PFDD model development will review the PFDD methodology through the lens of the focused development and applications. As such the PFDD formulation will be expressed using various notations that the author felt was most suitable for highlighting the focus of that work.

These iterations of the PFDD model are applied to study: i) the equilibrium dislocation core (compact or dissociated and the resulting stacking fault widths, R_e) on the basal, prismatic, and pyramidal II plane of several HCP materials with assumed elastic isotropy, ii) a more in depth study of the partial dislocation cores and R_e on the pyramidal II plane in 10 different HCP materials each with very unique GSFE curves and accounting for elastic anisotropy, iii) dynamic stacking fault widths R_d on the basal and pyramidal II plane and critical stress required for dislocation emission from a Frank-Read (FR) source, along with a study of the Burgers vectors of the

partial dislocations and the associated stacking fault, and iv) temperature dependency of dislocation velocities and loop formation from a FR-source on the pyramidal II plane.

In addition to developing a greater understanding of the aforementioned, we hope that the important material dependent properties calculated using PFDD will help bridge computational methods across the multiscale modeling lengths and times (See Figure 1.6.1).

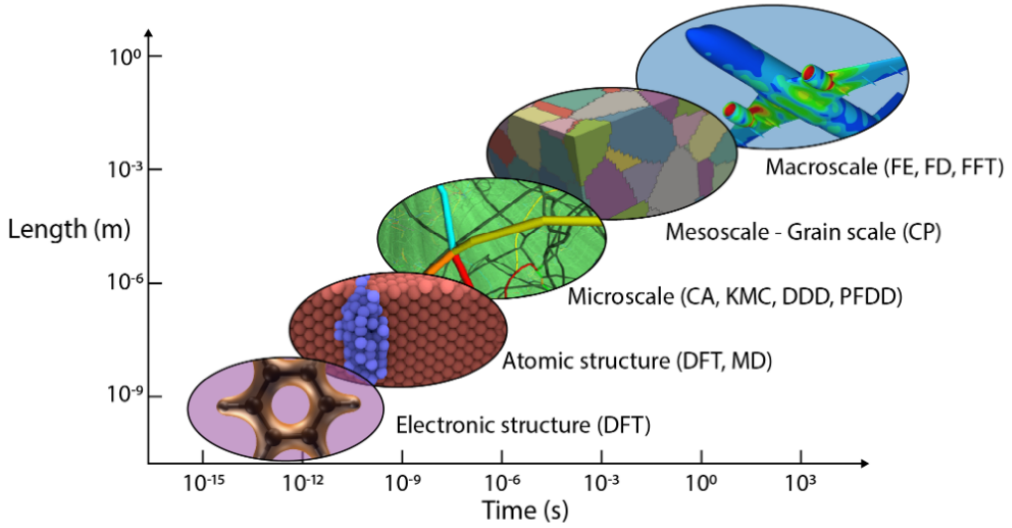

Figure 1.6.1: *Multiscale modeling. PFDD bridges the scale by using input calculated from density functional theory (DFT) and its output can be used to better inform larger continuum models. This figure is adapted from http://www.dierk-raabe.com/multiscale-modeling/*

1.6.1 PFDD code development for HCP slip planes

Chapter 2 reviews our work exploring dislocations on various planes in HCP materials, which was published in Reference [1]. We build upon the 3D

phase field dislocation formulation, called phase field dislocation dynamics (PFDD), presented in [39, 108, 109, 41] and adapt it to treat dislocations on slip systems belonging to distinct slip modes in an HCP crystal. To demonstrate the method, we carry out calculations for a small selection of materials, Mg, as well as an MgY alloy, Ti and Zr that would be potentially distinct in the structures of their dislocation cores. The choice of Mg is particularly important since dislocations in Mg have been heavily studied by a number of other computational methods. It is nearly elastically isotropic and the dislocations belonging to the different slip modes are sufficiently distinct. The PFDD model requires as input the stacking fault energies on the different slip planes of HCP crystals, and here, the slip-plane energetic landscapes, called the generalized stacking fault energies, are calculated using DFT for Mg, Ti, and Zr. Use of DFT advantageously circumvents the need for reliable interatomic potentials from atomic-scale simulation. The extended HCP phase field dislocation model is applied to calculate the core structures of dislocations on the three common HCP slip modes: basal, prismatic, and pyramidal-type II, under zero applied stress. We compare these results with similar calculations by MD and DFT available in the literature to verify the model extensions. This 3D phase field method will be suitable for calculating the formation, motion and interaction of extended defects in strained HCP crystals.

1.6.2 PFDD application to R_e on pyramidal II plane in 10 HCP materials

Chapter 3 reviews our work exploring the pyramidal II plane, published in Reference [2], we employ an elastically anisotropic version of the PFDD ap-

proach, developed in Reference [95], to compute the equilibrium structures of pyramidal-II $\{\bar{1}\bar{1}22\}\langle 11\bar{2}3\rangle$ dislocations in ten HCP metals: Be, Co, Mg, Re, Ti, Zn, Cd, Hf, Y, and Zr. All input parameters including the lattice parameters, elastic constants, and GSFE curves are computed from first principles to avoid any dependence on interatomic potentials. These ten metals exhibit anisotropic elasticity to varying degrees [7]. For the DFT GSFE calculations, we apply the same method with full relaxation to all ten and show that their energetic landscapes exhibit with a single local minimum and two unequal maxima, featuring a wide range of intrinsic SFEs. We show that achieving a single local minimum in the GSFE for Co requires accounting for its ferromagnetic properties.

In all these metals, the $\langle c+a\rangle$ pyramidal dislocations dissociate into two partials that separate in plane, creating extended structures, with nm-sized splitting distances. For the screw dislocation, Zn has the widest splitting distance and Ti the narrowest, and for the edge dislocation, Hf has the widest and Be the narrowest. Considering all ten metals, the separation distances scale inversely with the normalized intrinsic SFE, $I/(Kb)$, where K is an anisotropic energy factor dependent on elastic constants and dislocation character. In most cases, the dislocation partial core widths and Burgers vectors are not ideally equal. These asymmetries in the dislocation structures can be explained by deviations in the $\{\bar{1}\bar{1}22\}$ GSFE landscape from that expected of a metal with an ideal c/a ratio and symmetric landscape. Metals with higher levels of elastic anisotropy have wider separation distances for both screw and edge character dislocations than expected with effective isotropic constants, being 20–35% broader for Zn, which is highly anisotropic but having no effect on Re, Y, and Mg, which are all nearly isotropic. These findings on the equilibrium structure of $\langle c+a\rangle$ pyramidal-II dislocations across a broad range of

HCP metals are important for understanding their motion and interactions with other dislocations or interfaces.

1.6.3 Dynamics of dislocations in HCP

At least 5 active independent slip systems are required for plastic deformation, but research shows that many HCP materials only have 3 active independent slip systems available at room temperature that allow for only $\langle a \rangle$ type dislocation glide, meaning the necessary $c-$axis deformation is not accommodated by slip at these temperatures. Given the need for more active independent slip systems beyond those mentioned on the basal plane to improve ductility and the temperature sensitivity of non-basal plane activation for $\langle c+a \rangle$ dislocation slip we need a better understanding of what is going on in the pyramidal II plane when it is under external shear stresses. Thus, the broader goal in Chapter 4 is to fill the gaps in our understanding of the dynamic $\langle c+a \rangle$ dislocation behavior on the pyramidal II plane.

Isolating the pyramidal II plane for study via experimental approaches is incredibly sensitive to sample preparation and orientation, thus it is difficult if not impossible to limit the influence of basal and twinning deformation. Therefore, PFDD model and its ability to isolate dislocation glide to one slip plane, is the perfect tool to consider dynamic dislocation behavior on the pyramidal II plane. In this Chapter 4 we will build upon the work in the previous chapters, which considered $\langle c+a \rangle$ dislocation behavior, including dissociation, partial core spreading, and the equilibrium stacking fault widths on the pyramidal II plane in 10 different HCP materials [1, 2], by now applying an external shear stress in these simulations.

We first look for directional dependencies in the applied stress for dislocation mobility on the pyramidal II plane, since the previous work showed

strong asymmetries in the partial cores, it would follow that these might have an impact on their mobilities and dynamic stacking fault widths dSFW. We do find that the dSFW have a directional dependency that corresponds to the GSFE asymmetries and the magnitude of the partial Burgers vectors. We use an infinitely long dislocation dipole set-up for these simulations.

Next we use a Frank-Read source set-up to explore the behavior of expanding dislocation loops of various lengths, initial characters, and their corresponding critical shear stress σ_c. For comparison, we first start with simulations isolating dynamic dislocation loop behavior on the basal plane, which does not have any directional dependencies, but does evolve ununiformly due to the decompsition of the Burgers vectors into partials. Then we explore the pyramidal II plane in greater depth. The colinear nature of the Burgers vector decomposition results in uniform, symmetrical dislocation loop expansion, but we see directional dependencies in the applied stress, and loop shape variations depending on the character of the initial dislocation. This is the result of the loop shape minimizing to total energy from the dislocation line tension by minimizing the edge type portions of the loop and maximizing the screw type portions of the loop since they have a lower line tension penalty. All of this work is simulated using the deterministic version of the PFDD model

1.6.4 Thermally activated dislocation motion on the pyramidal II plane

As what just covered, at least 5 active independent slip systems are required for plastic deformation, but many HCP materials have 3 active independent slip systems available at room temperature that allow for only $\langle a \rangle$ type

dislocation glide, meaning the necessary $c-$axis deformation is not accommodated by slip at these temperatures. Deformation twinning can help to accommodate $c-$axis deformation at room temperature, but some of these HCP materials, including Mg, exhibit limited deformation twinning, the combined effect resulting in low ductility. Both basal slip and deformation twinning are relatively temperature insensitive and yet increases in the ductility of HCP materials are observed at higher temperatures, thus there must be a transition in deformation modes that can accommodate $c-$axis compression/tension from deformation twinning to $\langle c+a \rangle$ dislocation slip at higher temperatures. Thus, the broader goal in Chapter 5 is to fill the gaps in our understanding of how temperature affects $\langle c+a \rangle$ dislocation behavior on the pyramidal II plane.

We do this by deriving the Langevin force equations for the phase field framework to account for thermal fluctuations at variable temperatures. This produces a thermal noise term that we can add to the energy minimization equation in the PFDD model. This advanced PFDD model with thermal capabilities is then used to explore how temperature effects the time to dislocation loop formation from a Frank-Read FR source. We study Mg, Ti, and Zr. We also look at the velocity of infinitely long screw and edge type dislocations under the same applied shear stress. We find the leading partial for the screw dislocation "breaks away" at a greater velocity than the trailing partial at lower temperatures creating a growing dSFW. In the FR source simulations this results in the screw portions "smearing" out at higher temperatures. This breakaway phenomenon observed on the pyramidal II plane is both stress and temperature dependent.

Chapter 2

Development of phase field model for dislocations in hexagonal close packed crystals

In this stage of the phase field dislocation dynamics PFDD model development, which was published in Reference [1], we build upon the 3D phase field dislocation formulation presented in [39, 108, 109, 41] and adapt it to treat dislocations on slip systems belonging to distinct slip modes in an HCP crystal. To demonstrate the method, we carry out calculations for a small selection of materials, Mg, as well as an MgY alloy, Ti and Zr that would be potentially distinct in the structures of their dislocation cores. The choice of Mg is particularly important since dislocations in Mg have been heavily studied by a number of other computational methods. It is nearly elastically isotropic and the dislocations belonging to the different slip modes are sufficiently distinct. The PFDD model requires as input the stacking fault energies on the different slip planes of HCP crystals, and here, the slip-plane energetic landscapes, called the generalized stacking fault energies,

are calculated using DFT for Mg, Ti, and Zr. Use of DFT advantageously circumvents the need for reliable interatomic potentials from atomic-scale simulation. The extended HCP phase field dislocation model is applied to calculate the core structures of dislocations on the three common HCP slip modes: basal, prismatic, and pyramidal-type II. We compare these results with similar calculations by MD and DFT available in the literature to verify the model extensions. This 3D phase field method will be suitable for calculating the formation, motion and interaction of extended defects in strained HCP crystals.

2.1 Methodology

The PFDD formulation is general and application to different material systems falls largely on choice of energetic terms, and their parameters and functional forms. Up to now research has focused on cubic systems, and the energetic terms in the master energy functional have been selected to apply best to cubic crystal structures. Due to the symmetry of cubic materials, some simplifying assumptions could be made and here for the low symmetry of HCP crystals, these need to be re-evaluated. In this section we briefly review the PFDD approach and in the next section, we detail the energetic terms applicable for dislocations in HCP crystals.

2.1.1 The Phase Field Approach for Dislocations

Phase field formulations treat a 3D discretized system where every point is a thermodynamic system, whose free energy is specified as a function of the field variables of interest. A scheme is used to minimize the total system energy and solve for the corresponding values for the field variables. The

field variables, or order parameters, are scalar-valued and evolve within the system. In the case of dislocations, the order parameters, ζ_α, represent the location of slip by dislocations in the slip system α. A physically based definition for these order parameters associates one order parameter with slip made by each slip system. In the case of an FCC crystal, there are 12 order parameters needed to fully describe dislocation dynamics in an FCC crystal [90, 89, 31]. A mathematically based definition, however, considers a reduced set of order parameters associated with slip made by independent directions. For an FCC crystal, using this definition produces eight order parameters, consisting of a set of slip by both perfect and partial slip systems [110].

In the dislocation problems of interest, the total free energy of the system consists of three contributions [90, 89, 31]:

$$E = E^{strain} + E^{ext} + E^{lattice} \tag{2.1.1}$$

where E^{strain} is the elastic strain energy generated by a dislocation and dislocation-dislocation interactions, E^{ext} is work done to the system through an applied stress, and $E^{lattice}$ describes the energy expended as a dislocation glides through the crystal lattice breaking and re-forming atomic bonds. Some, but not all, phase field dislocation formulations [89, 110] include an energy term associated with the gradient in the order parameter. It is particularly relevant at the dislocation line, at the boundary between the slipped and unslipped region and its functional form depends on the configuration of the core, e.g., whether it is planar or non-planar, spread or compact. It is best informed by atomic-scale calculations, and in practice the term has introduced fitting parameter(s) to be adjusted according to an atomic scale core calculation. The impact of the additional gradient energy term has been reported in a few studies, each having focused on its effects for a particular

FCC metal [111, 94, 3, 112]. In this work, we elect to make independent comparisons between our dislocation structure calculations and those from other methods and to not add fit parameters. Therefore, in this first presentation of the HCP formulation, we neglect the gradient energy term, bearing in mind that it would straightforward to include it in later treatments.

Traditionally, the strain energy E^{strain} can be expressed as

$$E^{strain} = \frac{1}{2}\int C_{ijkl}\epsilon^e_{ij}(\mathbf{x},t)\epsilon^e_{kl}(\mathbf{x},t)d^3x \tag{2.1.2}$$

where C_{ijkl} is the elastic moduli tensor. Through transformation into Fourier space, the elastic strain, ϵ^e, can be expressed in terms of the plastic strain, ϵ^p. The strain energy can then be written as

$$E^{strain} = \frac{1}{(2\pi)^3}\frac{1}{2}\hat{A}_{mnuv}(\mathbf{k})\hat{\epsilon}^p_{mn}(\mathbf{k})\hat{\epsilon}^{p*}_{uv}(\mathbf{k})d^3k \tag{2.1.3}$$

where a superposed ($\hat{}$) denotes the Fourier transform, $\hat{A}_{mnuv}(\mathbf{k}) = C_{mnuv} - C_{kluv}C_{ijmn}\hat{G}_k(\mathbf{k})k_jk_l$, $\mathbf{k}$ is the wavenumber vector, $\hat{G}_k(\mathbf{k})$ is the Fourier transform of the Green's tensor of linear elasticity, denotes the principal value of the integral, and the superscript $(*)$ denotes the complex conjugation.

The plastic strain ϵ^p results from the motion of dislocations and, therefore, can be expressed as a function of the order parameters [90, 89]

$$\epsilon^p_{ij} = \frac{1}{2}\sum_{\alpha=1}^{N} b\zeta_\alpha(\mathbf{x},t)\delta_\alpha(s^\alpha_i m^\alpha_j + s^\alpha_j m^\alpha_i). \tag{2.1.4}$$

The sum is taken over all slip systems from 1 to N included in the material, b is the magnitude of the Burgers vector, $\mathbf{m}$ is the slip plane normal, $\mathbf{s}$ is the slip direction (normalized Burgers vector), and δ_α is a Dirac distribution supported on the active slip planes. Considering again, as an example, the FCC crystal structure, wherein there are 12 slip systems belonging to the $\{111\}\langle 110\rangle$ slip mode and hence 12 order parameters. Dislocations on these

systems are referred to as perfect dislocations since their Burgers vector corresponds to a lattice translation vector. The slip plane normals are of the $\{111\}$ type, slip directions are of the $\langle 110 \rangle$ type, and $N = 12$ for all possible glide systems.

The external energy is given by

$$E^{ext} = \int \sigma_{ij}^{appl} \epsilon_{ij}^{p} d^3x \tag{2.1.5}$$

where σ^{appl} is the applied stress tensor. Similar to the strain energy, the dependence on the order parameters comes through the expression of the plastic strain shown in Equation 3.1.1.

The lattice energy $E^{lattice}$ represents the expenditure of breaking and reforming interlayer atomic bonds as a perfect or partial dislocation moves through the crystal lattice. This lattice energy depends on the material and on the crystallographic plane under consideration. In general, the lattice energy $E^{lattice}$ can be written as

$$E^{lattice} = \sum_{\alpha=1}^{N} \int \phi_\alpha(\zeta_1(\mathbf{x}), \zeta_2(\mathbf{x}), ..., \zeta_N(\mathbf{x})) d^2x \tag{2.1.6}$$

where $\phi_\alpha(\zeta_1(x), \zeta_2(x), ...)$ is a periodic potential and the equation is integrated over the slip plane. It is also possible that this potential could be a function of multiple order parameters from slip systems, $\zeta_1(x)$, $\zeta_2(x)$ ... $\zeta_N(x)$.

The time-dependent Ginzburg-Landau (TDGL) equation is used to evolve the total system energy to equilibrium and determine the order parameters corresponding to the equilibrium state. It relates the time variation of the order parameters to the variation in the total system energy with respect to each order parameter α as follows:

$$\frac{\partial \zeta_\alpha(\mathbf{x}, t)}{\partial t} = -L \frac{\delta E(\zeta)}{\delta \zeta_\alpha(\mathbf{x}, t)} \tag{2.1.7}$$

where L is related to the convergence speed (or mobility) of the system and has a non-negative coefficient that is constant for all order parameters. We arbitrarily set $L = 1$ and chose a time step small enough to resolve the evolution of the system. (In Chapter 5 we have to account for the material specific value of L as it is used in the thermal noise term, which is added to the TDGL equation.) For calculations involving multiple order parameters, Equation 2.1.7 becomes a set of N coupled integro-differential equations, where N equals the number of order parameters, that must be solved numerically to evolve the system. Additionally, the solution of this equation requires the use of a Fast Fourier Transform in order to determine the contribution of the strain energy (as shown in Equation 3.1.4) to the total energy.

2.1.2 PFDD extensions for HCP crystal structures

The PF formulation for an HCP crystal structure departs from the foregoing one in two main aspects, first by taking into account the low symmetry of the HCP crystal structure, and second, the multiplicity of slip modes. These aspects affect the development of all energetic terms in the master energy functional, which in the present study, are the elastic strain energy, external energy, and lattice energy in Equation 3.1.3.

The first important departure from the cubic systems is that the basis for the lower symmetry HCP system is not Cartesian. Directions in the HCP unit cell are conventionally expressed using the Miller-Bravais four-index notation {hk.l} or Miller three-index notation {hkl}. Unlike FCC metals, the Miller three-index notation for HCP slip systems has a 120° angle between the first two indices. Further one axis, the c-axis, is longer than the other two axes. The c/a ratio depends on the HCP metal. In the present code, we elect to first transform all slip plane normals and slip directions expressed in the

HCP basis to a Cartesian coordinate system, so that that usual mathematical manipulations, utilizing dot and cross-products, can be used.

The second aspect concerns the multiplicity of slip modes, which involves specifically appreciating the differences in the atomic structure and crystallography among the common slip modes in the HCP system. Every slip mode in the HCP crystal has its own value of the Burgers vector, slip plane, and number of slip systems. Within a mode, the slip systems share the same crystallography but are independently oriented. Here we demonstrate the method by modeling dislocations on three of the most frequently observed modes in deformed HCP crystals: the basal, prismatic, and pyramidal-II slip modes. Both the basal ((0001) plane) and prismatic ($\{\bar{1}010\}$ type planes) slip modes accommodate glide of $\langle a \rangle$-type dislocations, which are dislocations with $\langle a \rangle$ Burgers vectors. The prismatic and basal slip modes also each have three slip systems. The pyramidal-II mode ($\{\bar{2}112\}$ type planes), however, can accommodate strain in the $\langle c \rangle$ direction through the motion of $\langle c + a \rangle$ dislocations. The Burgers vector is aligned along a specific $\langle c + a \rangle$ direction lying in the glide plane. Six slip systems belong to the pyramidal-II mode. Apart from these three modes, a few other slip modes have been observed in the deformation of HCP crystals (such as the pyramidal-I mode) but are not considered in the present examples. These can be incorporated using the same methodology as developed here.

Redefinition of the slip planes and slip directions for the HCP crystal affect the formulation of the plastic strain, ϵ^p, which is used directly in the calculation of the elastic strain energy and external energy, Equations 3.1.4 and 5.2.4. To accommodate the different slip modes and their distinct Burgers vectors, Equation 3.1.1 is re-written to consider a slip plane-dependent

Burgers vector

$$\epsilon_{ij}^{p} = \frac{1}{2}\sum_{\alpha=1}^{N} b_\alpha \zeta_\alpha(\mathbf{x},t)\delta_n(s_i^\alpha m_j^\alpha + s_j^\alpha m_i^\alpha) \tag{2.1.8}$$

As before, the slip plane normal and slip direction are slip system-dependent, but in the above, the dependency of the magnitude of the Burgers vector on the slip mode is also taken into account. N is the total number of slip planes. Considering the three slip modes, we define N_b, N_{pr}, and N_{py} as the number of slip systems available in the basal, prismatic, and pyramidal-II slip modes, respectively. Hence, $N_b + N_{pr} + N_{py} = N$ and $\alpha = 1$ to N, where $N = 12$.

The expression for $E^{lattice}$ will also differ substantially from one slip mode to another within the same HCP crystal. First, as in the other terms, the crystallography of the slip planes and slip directions associated with preferred slip in the HCP crystal must be defined. Second, the lattice energies for each slip mode need to be considered individually, since the atomic density and configuration of the atoms differ among the glide planes of these modes. The general form of the lattice energy presented in Equation 5.2.5 is still appropriate; however, the functional form of the periodic potential will depend on the atomic interactions across the particular slip plane of interest. The total $E^{lattice}$ will consist of the energy contributions from dislocations that may be present on any or all of these three slip modes at a time.

In the present formulation, slip by each slip system is defined physically and so a unique order parameter is associated with each slip system. Consequently, the lattice energies associated with different systems are mutually

exclusive, permitting us to write the lattice energy as follows:

$$\begin{aligned} E^{lattice} &= E^{basal} + E^{prism} + E^{pyrII} \\ &= \sum_{\alpha=1}^{N_b} \int \phi_\alpha^{basal}(\zeta_1(\mathbf{x}), ..., \zeta_{N_b}(\mathbf{x}))d^2x \\ &+ \sum_{\alpha=1}^{N_{pr}} \int \phi_\alpha^{pr}(\zeta_1(\mathbf{x}), ..., \zeta_{N_{pr}}(\mathbf{x}))d^2x \\ &+ \sum_{\alpha=1}^{N_{py}} \int \phi_\alpha^{pyrII}(\zeta_1(\mathbf{x}), ..., \zeta_{N_{py}}(\mathbf{x}))d^2x \end{aligned} \tag{2.1.9}$$

where E^{basal} is the lattice energy for dislocations gliding on basal slip planes, E^{prism} the lattice energy for dislocations gliding on prismatic planes, and E^{pyrII} for the lattice energy for dislocations gliding on pyramidal-II planes. At a given point in the computational volume, lattice energies will for the most part correspond to one plane and hence order parameters on that plane. The sum of two or more lattice energies will occur when glide planes from different slip modes intersect. In addition, as exemplified in Equation 5.2.5, the periodic potentials may be a function of order parameters from multiple slip systems.

2.1.3 DFT determined γ-surfaces and GSFE curves

The $E^{lattice}$ is a material-specific and slip-plane-specific function of the order parameters, associated with the energy expended when bonds are broken across the plane in dislocation glide. In prior works, the models used for $E^{lattice}$ originate from simple functions, such as a single parameter sine-squared function [38] to multi-parameter piece-wise quadractic function [90], to more complex sinusoidal functions modeling in detail a generalized stacking fault energy (GSFE) curve [113, 114], or Fourier sine series [3, 115, 31, 116], modeling a 2D γ-surface. The parameters associated with these func-

tions are usually informed by an atomistic calculation particular to the material. When the energy landscape is too complex to be described reliably by a function, an alternative approach has been to employ look-up tables comprised a large set of pre-calculated energies corresponding to a fine grid of points on the energetic landscapes [110, 94]. Obtaining the energy associated with dislocation glide on a particular plane has been derived by considering an ideal situation of cutting a perfect crystal in half across the glide plane of interest and calculating the excess energy per unit area incurred by shifting one crystal half with respect to the other half [117, 118]. The γ-surface is the energy landscape associated with all possible shifts in the two in-plane dimensions. The energy associated with shifting this plane in solely one crystallographic direction lying on the plane (one slice of the γ-surface) corresponds to a curve, referred to as a generalized stacking fault energy (GSFE) curve. In the case of slip in an FCC crystal, γ-surface is usually calculated for the $\{111\}$ slip plane, the one glide plane of interest, and the energy associated with shifting this plane in either the $\langle 110 \rangle$ or $\langle 112 \rangle$ directions are the common GSFE curves. GSFE curves and γ-surfaces do not directly represent a dislocation, but they represent the energy associated with the changes in atomic positions that a dislocation would cause as it glides on that plane. These energetic quantities have been adopted in $E^{lattice}$ since they are undeniably more convenient to calculate than the Peierls barrier.

Here, as mentioned, we apply the model to different glide planes in four HCP crystals, Mg, MgY, Ti, and Zr, and we will adopt GSFE curves or γ-surfaces in $E^{lattice}$ for them. These energetic quantities are commonly calculated with atomic-scale methods, such as DFT or MD [111, 20]. However, most DFT γ-surfaces and GSFE curves apply to cubic materials and not to planes in HCP materials [119, 120]. The most common cases for HCP

metals are the GSFE curves for the basal slip mode in Mg and Mg alloys [121, 16, 20]. Here we will use the GSFE for the basal plane in $Mg_{47}Y$ from [122]. For the prismatic slip plane in Mg, Zr and Ti, the DFT-calculated GSFE curves that we will use have been calculated in [16, 77, 123, 21, 124]. The γ-surface for the pyramidal-I plane in Mg has already been presented in [15, 16, 125].

For the PFDD calculations presented in this work, we performed additional DFT calculations for the GSFE curves for the HCP crystalline planes that are not available in the literature, which include γ-surfaces and GSFE curves for the basal plane in Mg and the pyramidal-II planes in Mg and Ti. For all DFT calculations here we use the code as implemented in Vienna *Ab-initio* Simulation Package (VASP) [126, 127] and utilize the generalized gradient approximation (GGA) for the exchange correlation functional with the Perdew-Burke-Ernzerhof (PBE) parameterization [128]. The interaction between valence electrons and ionic cores was treated using PAW potentials. The number of valence electrons in Mg potential taken is 2 and in the Ti potential 4. A plane wave energy cutoff of 400 eV was employed and the structure was optimized until the force on each atom became smaller than 0.01 eV/A. We used a 19x19x19 Gamma-centered Monkhorst Pack k-point mesh to integrate the Brillouin Zone of the primitive HCP unit cells to calculate the lattice constants and elastic constants.

The lattice parameters and elastic constants are presented Table 2.1.1. All values were calculated here using our DFT methods but the moduli for $Mg_{47}Y$, which were obtained from [122]. Overall, these are in good agreement with previous DFT calculations and experimental measurements [77, 15]. These values will be used in the PFDD calculations that follow. For the sake of simplicity, the elastic strain energy generated around the dislocation is

calculated under the assumption that the material is a linear elastic, isotropic solid. The isotropic elastic stiffness tensor is given by:

$$\mathbf{C} = \begin{bmatrix} \lambda+2\mu & & & & & \\ \lambda & \lambda+2\mu & & & & \\ \lambda & \lambda & \lambda+2\mu & & \text{Symm} & \\ & & & \mu & & \\ & & & & \mu & \\ & & & & & \mu \end{bmatrix} \tag{2.1.10}$$

where μ is the shear modulus and λ is Lamé's first parameter, which are related by

$$K_{\mathrm{b}} = \lambda + \frac{2}{3}\mu \tag{2.1.11}$$

We calculate μ and K_{b} using the following Voigt equations for hcp [129]

$$\mu = \frac{1}{15}[(2C_{11} + C_{33}) - (C_{12} + 2C_{13}) + 3(2C_{44} + C_{66})] \tag{2.1.12}$$

$$K_{\mathrm{b}} = \frac{1}{9}[(2C_{11} + C_{33}) + 2(C_{12} + 2C_{13})] \tag{2.1.13}$$

The DFT determined and isotropic averages used in the calculations for Mg, Ti, and Zr are presented in Table 2.1.1.

In the DFT calculation of the generalized stacking fault energies, we used the relaxed method [15], wherein for each displacement step, minimization of the energy of the system is ensured by fixing all atomic positions along the glide direction and allowing positions along the plane normal and the in-plane direction lying normal to the glide direction to relax. For each slip plane, the supercell dimensions are chosen based on the minimum number of layers along the z-direction for which convergence in system energy is attained. For Mg, the periodic model for basal slip plane contains 52 atoms and its dimensions are 3.19 Å along x, 5.53 Å along y and 77.17 Å along z.

Table 2.1.1: *Lattice constant (in Å) and elastic constants (units of GPa) for bulk HCP-Mg, Ti, and Zr obtained from DFT and isotropic averages for the shear modulus, μ, and Lamé's parameter, λ.*

Material	a (Å)	c/a	C_{11}	C_{33}	C_{12}	C_{13}	C_{44}	C_{66}	μ	λ
Magnesium	3.190	1.625	63.3	65.7	25.9	20.8	18.0	18.7	19.26	23.53
$Mg_{47}Y$	3.206	1.626	63.3	65.7	25.9	20.8	18.0	18.7	19.26	23.53
Titanium	2.923	1.581	159.4	191.7	108.9	83.9	37.6	25.2	35.68	94.43
Zirconium	3.231	1.601	135.1	166.1	80.3	70.7	26.1	27.4	30.23	77.59

The periodic model for pyramidal-II slip plane in Ti contains 60 atoms and its dimensions are 5.063 Å along x, 5.467 Å along y, and 51.960 Å along z. All supercells contain a thick vacuum layer of 15 Å along the z-direction.

2.1.4 Lattice energy for the basal slip mode

On the basal plane, there are three possible directions of slip, each corresponding to an order parameter for that plane, ζ_1, ζ_2, and ζ_3. For the basal plane, the lattice energy E^{basal} can be expressed as

$$E^{basal} = \sum_{\alpha=1}^{N_b} \int \phi_\alpha^{basal}(\zeta_1, \zeta_2, \zeta_3) d^2x \,, \tag{2.1.14}$$

where ϕ_α^{basal} is the periodic potential and $\alpha = 1$ to N_b, the number of basal slip systems. As mentioned, here we characterize this potential with the GSFE surface, or γ-surface, the excess energy associated with shift one crystalline half relative to another about the basal plane. Using DFT for set of in-plane shear displacement, this surface has been calculated for Mg. Figure 2.1.1 presents the γ-surface for the basal plane calculated from DFT. First, it is

recognized that the location of the maxima and minima in this basal plane γ-surface coincide well with those of the $\{111\}$ plane in an FCC crystal. In prior PFDD work on FCC γ-surfaces, a common approach is to parameterize a continuous function for the $\phi(\zeta)$ from a discrete set of DFT calculations on a γ-surface. In this way derivatives were directly calculable and less DFT calculations were required overall to construct the potential. A function that fit the FCC plane well is the seven-coefficient complex Fourier series function [115, 3, 116]. Here we adopt this function for the ϕ_α^{basal} and parameterize it for the basal plane using the seven DFT calculated points on the basal plane γ-surface. This function is given by

$$\begin{aligned}
\phi^{basal}(\zeta_1,\zeta_2,\zeta_3) = {} & j_0 + j_1[\cos 2\pi(\zeta_1-\zeta_2) + \cos 2\pi(\zeta_2-\zeta_3) + \cos 2\pi(\zeta_3-\zeta_1)] \\
& + j_2[\cos 2\pi(2\zeta_1-\zeta_2-\zeta_3) + \cos 2\pi(2\zeta_2-\zeta_3-\zeta_1) + \cos 2\pi(2\zeta_3-\zeta_1-\zeta_2)] \\
& + j_3[\cos 4\pi(\zeta_1-\zeta_2) + \cos 4\pi(\zeta_2-\zeta_3) + \cos 4\pi(\zeta_3-\zeta_1)] \\
& + j_4[\cos 4\pi(3\zeta_1-\zeta_2-2\zeta_3) + \cos 4\pi(3\zeta_1-2\zeta_2-\zeta_3) \\
& + \cos 4\pi(3\zeta_2-\zeta_3-2\zeta_1) + \cos 4\pi(3\zeta_2-2\zeta_3-\zeta_1) \\
& + \cos 4\pi(3\zeta_3-\zeta_1-2\zeta_2) + \cos 4\pi(3\zeta_3-2\zeta_1-\zeta_2)] \\
& + k_1[\sin 2\pi(\zeta_1-\zeta_2) + \sin 2\pi(\zeta_2-\zeta_3) + \sin 2\pi(\zeta_3-\zeta_1)] \\
& + k_3[\sin 4\pi(\zeta_1-\zeta_2) + \sin 4\pi(\zeta_2-\zeta_3) + \sin 4\pi(\zeta_3-\zeta_1)]
\end{aligned} \tag{2.1.15}$$

where the coefficients $j_0 - j_4, k_1, k_3$ define the material-dependent local maximum, local minimum, and curvature of the 2D energy surface. These coefficients correspond to particular points taken from the γ-surface, G, G_1, G_2, G_3, T, T_1

and are related to the coefficients via the following expressions [115]:

$$
\begin{aligned}
j_0 &= 0.823(4G - 6G_1 + 6G_2 - 7.392G_3 + 0.804T + 0.804T_1) \\
j_1 &= 0.274(-8G + 12G_1 - 12G_2 + 14.785G_3 - 1.608T + 0.215T_1) \\
j_2 &= 0.091(23.072G - 29.138G_1 + 32.785G_2 - 42.215G_3 + 2.569T - 2.412T_1) \\
j_3 &= 0.137(-8G + 12G_1 - 12G_2 + 14.785G_3 + 0.215T - 1.608T_1) \\
j_4 &= 0.023(1.856G - 13.723G_1 + 6.431G_2 - 4.277G_3 - 0.962T + 3.531T_1) \\
k_1 &= 0.137(-32G + 48G_1 - 48G_2 + 62.785G_3 - 4.608T - 2.785T_1) \\
k_3 &= 0.046(17.072G - 19.292G_1 + 31.923G_2 - 34.708G_3 + 3.341T - 8.354T_1)
\end{aligned}
\tag{2.1.16}
$$

Figure 2.1.1 compares the DFT calculated γ-surface for pure Mg and the surface calculated with the Fourier series approximation presented in Equation 2.1.15. The points, G, G_1, G_2, G_3, T, T_1, taken from the γ-surface to parameterize the approximation, are also shown on both energy landscapes. The pathway starting at point A and traveling through points T and T_1 (in $\langle 11\bar{2}0 \rangle$ type directions) represents a perfect Burgers vector translation. The other two pathways (one starting at A and traveling through G_1, G_2, G_3 to point G, and the other starting at point G), represent the two partial dislocation translations in $\langle 1\bar{1}00 \rangle$ type directions. In the case of basal slip, the six points shown in Figure 2.1.1 from the material γ-surface determine the coefficients needed in Equation 2.1.15. These values for pure Mg are: $G = 29.32\ mJ/m^2$, $G_1 = 57.70\ mJ/m^2$, $G_2 = 88.49\ mJ/m^2$, $G_3 = 66.08\ mJ/m^2$, $T = 262.73\ mJ/m^2$, and $T_1 = 151.53\ mJ/m^2$. The greatest deficiency of the Fourier series approximation is labeled by M in the top figure of Figure 2.1.1. The M point represents a global energetic maximum where two atoms are located directly on top of each other, and is incorrectly represented by Equation 2.1.15. However, this atomic configuration is not located along a

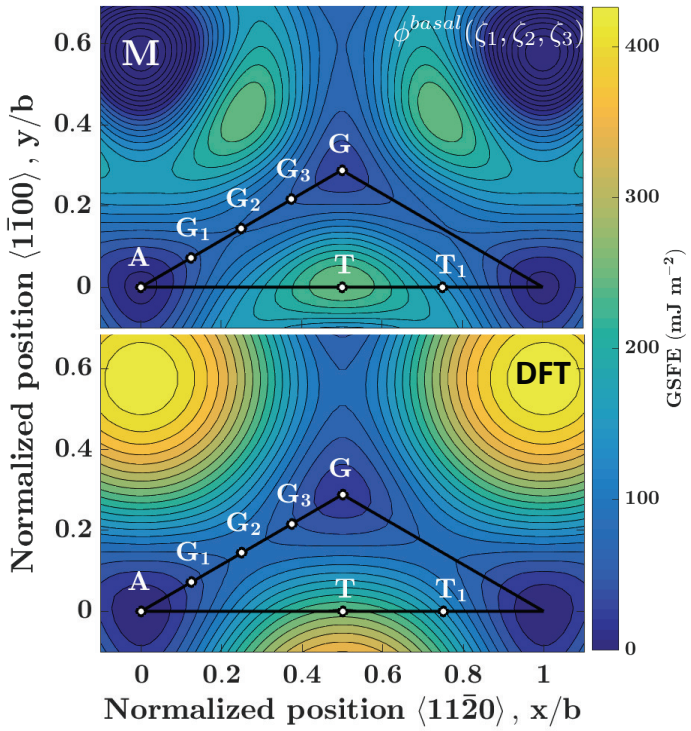

Figure 2.1.1: *Comparison of γ-surfaces for the basal slip plane in Mg as determined with DFT (bottom) and the parameterization (top) presented in Equation 2.1.15. The points used from the material γ-surface to determine the coefficients calculated with Equation 2.1.16 are labeled on both plots.*

pathway that would be involved in the dissociation of the perfect dislocation.

In order to model basal slip in $Mg_{47}Y$, we determined a parameterized γ-surface from the same seven points lying along the $\langle 11\bar{2}0 \rangle$ and $\langle 1\bar{1}00 \rangle$ GSFE curves calculated by DFT by [122]. From their work, we obtained the following values for $Mg_{47}Y$: $G = 27.80\ mJ/m^2$, $G_1 = 44.46\ mJ/m^2$, $G_2 = 83.82\ mJ/m^2$, $G_3 = 61.65\ mJ/m^2$, $T = 214.69\ mJ/m^2$, and $T_1 = 124.34\ mJ/m^2$. Using these values in Equation 2.1.16, the coefficients needed to inform ϕ^{basal} are calculated and presented in Table 2.1.2. Figures 2.1.2(a) and (b) directly compare the GSFE curves in a $\langle 1\bar{1}00 \rangle$ type direction as determined with DFT and the Fourier series approximation, showing reasonable agreement for this

particularly important slice of the energetic landscape.

Table 2.1.2: *Basal GSFE parameterization coefficients: Inter-planar spacing d normalized in terms of the Burgers vector b and the calculated coefficients for the lattice energy potential function (Equation 2.1.15) for the basal slip mode. All coefficients are shown in units of* mJ/m^2.

Material	d	j_0	j_1	j_2	j_3	j_4	k_1	k_3
Mg	0.81250	120.7223	-4.6751	-53.0878	25.4338	-3.8782	13.6261	-21.5761
$Mg_{47}Y$	0.81305	143.6364	-33.1868	-18.2934	5.6344	-0.9729	-44.8569	-6.2832

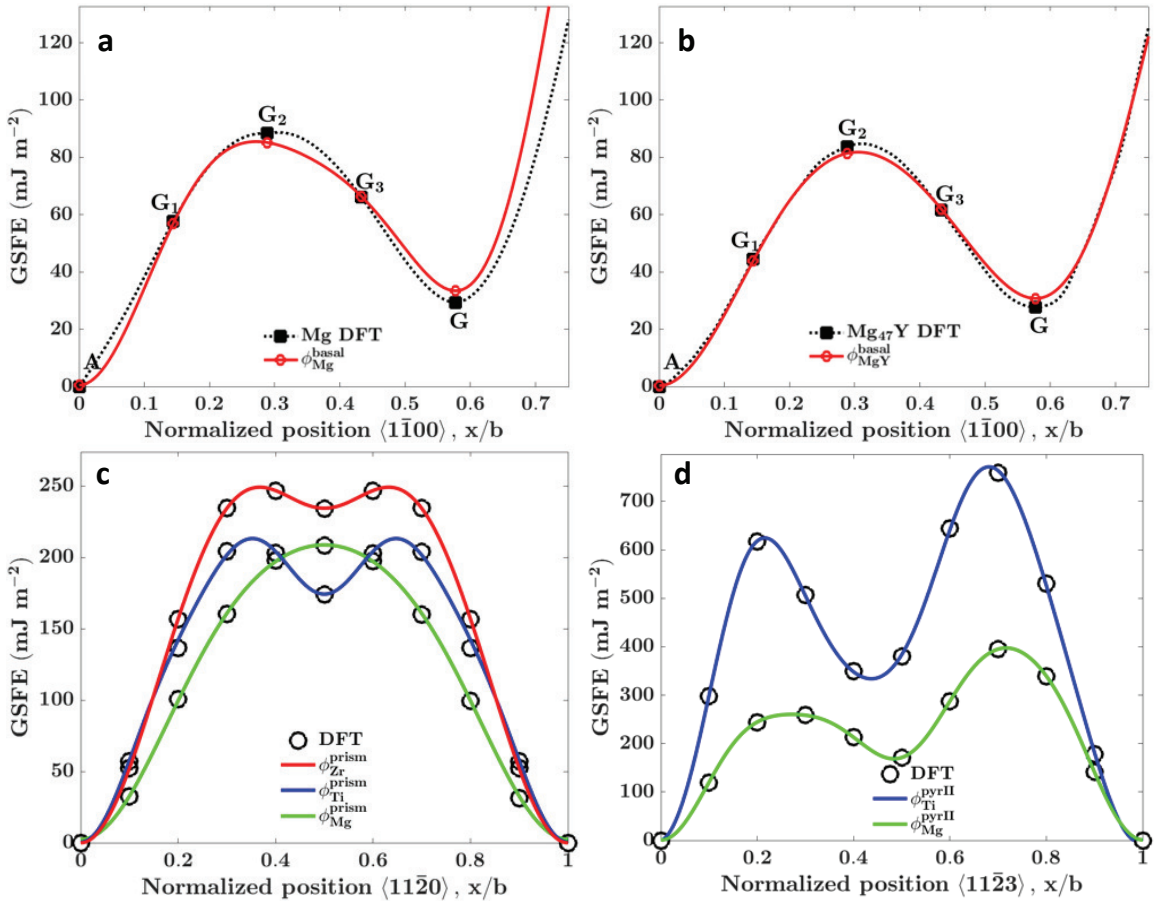

Figure 2.1.2: *Direct comparison of GSFE curves determined with DFT and the periodic potentials used in the calculation of the lattice energy in PFDD for (a) basal slip systems in pure Mg, (b) basal slip systems in $Mg_{47}Y$, (c) prismatic slip systems in pure Mg, Zr, and Ti, and (d) pyramidal-II slip systems in pure Mg, and Ti. Unlike the symmetric energetic paths for partials on the basal and prismatic planes, the pyramidal-II plane can have different positions and values for the local minima and maxima.*

2.1.5 Lattice energy for prismatic and pyramidal II slip modes

For prismatic slip, the relevant GSFE curve on the prismatic plane is associated with the prismatic slip system, $\{\bar{1}010\}\ \langle 1\bar{2}10\rangle$. For a prismatic dislocation in PFDD, E^{prism} can be expressed as a function of a single order parameter ζ_α corresponding to the slip direction $\langle 1\bar{2}10\rangle$ on the prismatic plane. The lattice energy is given by

$$E^{prism} = \sum_{\alpha=1}^{N_{pr}} \int \phi_\alpha^{prism}(\zeta_\alpha) d^2x \,, \tag{2.1.17}$$

ϕ_α^{prism} is the periodic potential for the excess energy expended in gliding along the slip vector. The ϕ_α^{prism} can be characterized by a GSFE curve along the slip direction $\langle 1\bar{2}10\rangle$. Here, these GSFE curves are calculated by DFT and are taken from published DFT results from [124] for Mg, [77] for the Zr data, and [123] for the Ti data. Figure 2.1.2(c) displays these curves. In a material like Zr, the GSFE curve along the prismatic plane has a local minimum, suggesting the possibility of a dislocation dissociation. Conversely in Mg, the GSFE curve has no local minimum, which would imply that the core is likely to remain compact.

The relevant GSFE curve for the pyramidal-II slip system is $\{\bar{2}112\}\ \langle 2\bar{1}\bar{1}3\rangle$. Similar to the prismatic case, we consider only one active order parameter ζ_α defined in a $\langle 2\bar{1}\bar{1}3\rangle$-type slip direction. In this case, the lattice energy is given by

$$E^{pyrII} = \sum_{\alpha=1}^{N_{py}} \int \phi_\alpha^{pyrII}(\zeta_\alpha) d^2x \,, \tag{2.1.18}$$

where ϕ^{pryII} is the periodic potential associated with excess energy in gliding along the slip vector. For ϕ^{pryII}, we adopt a generalized stacking fault energy

curve along $\langle 2\bar{1}\bar{1}3\rangle$ calculated using DFT. The pyramidal plane GSFE curve for Mg is taken from [15], but here, it was necessary to calculate the GSFE curve for Ti, as described in Section 2.1.3. GSFE curves for both Mg and Ti are different from those DFT curves previously reported, which did not employ full relaxation [16, 125].

In an effort to provide a continuous function for ϕ, we observe that the DFT GSFE curves for the prismatic and pyramidal-II systems for the particular metals we study here can be generally represented by the following function (where we drop the subscript α on ζ for brevity)

$$\begin{aligned}\phi^m(\zeta) = p_0 + p_1\cos(2\pi\zeta) + p_2\cos(4\pi\zeta) + p_3\cos(6\pi\zeta) + p_4\cos(8\pi\zeta) \\ + q_1\sin(2\pi\zeta) + q_2\sin(4\pi\zeta) + q_3\sin(6\pi\zeta) + q_4\sin(8\pi\zeta)\,, \qquad (2.1.19)\end{aligned}$$

where $m = prism$ and/or $pyrII$ depending on the active slip mode(s). We found this function convenient, but emphasize that not all GSFE curves would require all nine coefficients. If the potential is symmetric, such as for the prismatic plane GSFE curve for Ti, then the coefficients $q_1 - q_4$ can be set to zero. If it is symmetric and contains no local minima, like the prismatic plane GSFE curve for Mg, then p_4 can also be equal to zero.

The parameterized curves for ϕ_α^{prism} are compared against the DFT calculations in Figure 2.1.2(c). In these three metals, the continuous potential function provides excellent agreement to the data. Figure 2.1.2(d) shows the DFT calculated pyramidal-II GSFE curves in comparison with the function in Equation 2.1.19 for Mg and Ti. The pyramidal-II plane has an asymmetric GSFE curve along the slip direction, which requires calculation of all $p_0 - p_4, q_1 - q_4$ coefficients to fit the potential ϕ_α^{pyrII} to the DFT determined energy profile. For the two pyramidal-II curves, the function offers an excellent continuous function representation to the DFT data. All coefficients

Table 2.1.3: *Prismatic and pyramidal-II GSFE parameterization coefficients: Inter-planar spacing d normalized in terms of the Burgers vector b and the calculated coefficients for the lattice energy periodic potentials for the prismatic and pyramidal-II (Equation 2.1.19) slip mode. All coefficients are shown in units of mJ/m^2.*

Material	Plane	d	p_0	p_1	p_2	p_3	p_4	q_1	q_2	q_3	q_4
Mg	Prism	0.86603	119.18	-102.05	-13.60	-1.117	0.000	0.000	0.000	0.000	0.000
Ti	Prism	0.86603	138.65	-89.53	-43.96	2.591	-7.328	0.000	0.000	0.000	0.000
Zr	Prism	0.86603	129.90	-93.28	-33.45	3.198	-4.051	0.000	0.000	0.000	0.000
Mg	Pyr II	0.22318	217.98	-75.35	-116.48	-6.137	-9.728	-55.26	15.05	8.900	-1.228
Ti	Pyr II	0.22589	427.52	-165.06	-220.30	-22.96	-9.542	-52.33	118.72	-13.57	-16.63

for the prismatic and pyramidal-II cases were fit using the MATLAB curve fitting tool [130] and they are summarized in Table 2.1.3.

2.2 Equilibrium dislocation structure

In the following sections, we apply the HCP-PFDD method to simulate the dissociation of an initially perfect dislocation into a stable, equilibrium structure under zero applied stress. The structural characteristics that can be ascertained from the calculation are the partial dislocations resulting from the dissociation, the distance between the partials, the width of the individual partials and any asymmetry between their widths. For demonstration, the character of the starting perfect dislocation will be either pure edge or pure screw, although in principle, a dislocation of any initial character may be considered. In the examples, these dislocations lie on one of three planes: basal, prismatic, and pyramidal-II. When possible, we compare our results to those previously calculated by DFT and molecular statics or MD. Not all

cases treated here have been observed experimentally or pursued by other computational methods, such as DFT or MD.

2.2.1 Simulation configuration

All simulations were carried out in a 3D cuboidal simulation cell. Due to the use of a Fourier transform in the calculation of the elastic strain energy, all boundaries are periodic. We elect to orient the primary glide plane such that its normal direction lies parallel to the z-axis, as shown in Figure 2.2.1(a). Accordingly the crystallographic directions of the x, y, and z-directions depend on the slip system of interest. The corresponding directions for each simulation cube used for the basal, prismatic, and pyramidal-II planes are shown for an edge dislocation in Figures 2.2.1(b), (c), and (d), respectively. The $x-$, $y-$, and $z-axis$ in our simulation cell Figure 2.2.1(a) correspond to the $x-$, $y-$, and $z-axis$ respectively in our unit cells (see Figures 2.2.1(b-d)) when initializing for an edge dislocation and to $y-$, $x-$, and $z-axis$ respectively when initializing for a screw dislocation. Thus, the slip plane normal is always parallel to the $z-axis$ of the simulation cell, the dislocation line sense is always parallel to the $y-axis$ and the Burgers vector, which determines the orientation of the unit cell within the simulation cell and the character of the dislocation with respect to the line sense, is parallel to the $x-axis$ for an edge dislocation and the $y-axis$ for a screw dislocation. This additional orientation step is not a requirement but a choice made here since only one dislocation is being evaluated at a time in this study.

For convenience the grid spacing, λ_0, in all x, y, and z directions, is chosen to be the inter-planar distance of the slip plane, d, (normalized by the Burgers vector b of a dislocation on that plane for a material), given in Tables 2.1.2 and 2.1.3. For any HCP slip plane, given in $(hkil)$ or $(hk.l)$ Miller-

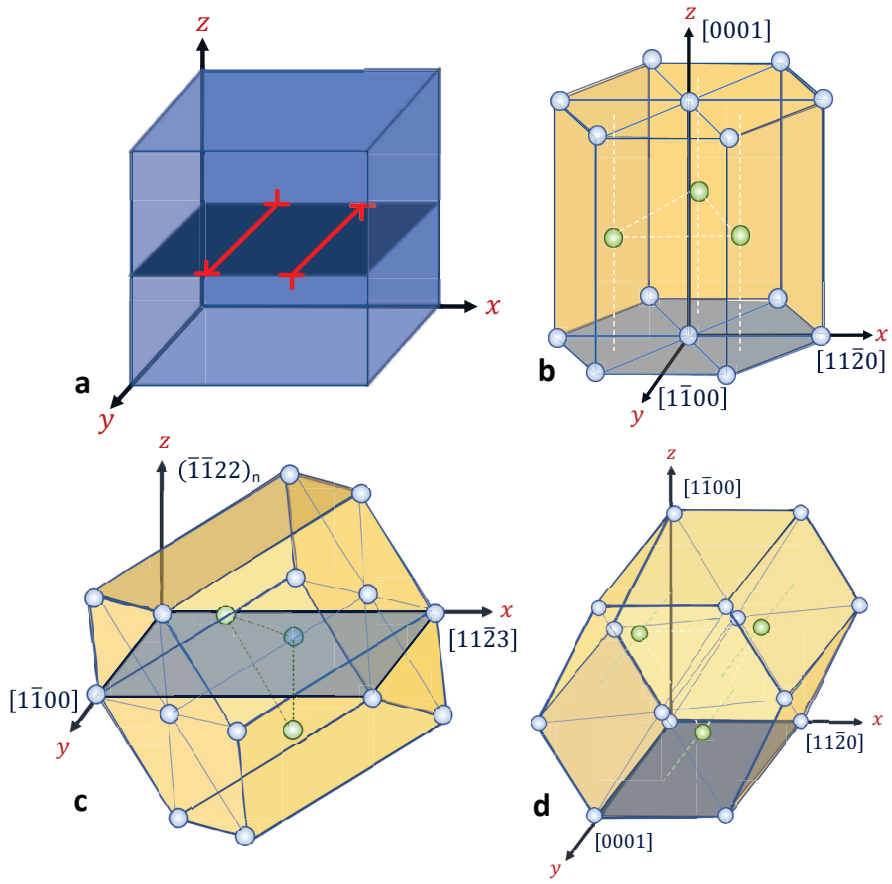

Figure 2.2.1: *Schematics showing (a) the initial simulation set-up for the PFDD computational cell, which was utilized with orientations for an edge dislocation on the (b) basal, (c) pyramidal-II, and (d) prismatic glide planes. The simulation set-up for a screw dislocation would have the same initialization shown in (a), while the unit cells in (b-d) would be rotated around their respective $z-axis$ by 90°. For clarity, the $x-$, $y-$, and $z-axis$ in our simulation cell correspond to the $x-$, $y-$, and $z-axis$ respectively in our unit cells when initializing for an edge dislocation and to $y-$, $x-$, and $z-axis$ respectively when initializing for a screw dislocation. Thus, the slip plane lies parallel to the simulation cell surface, the dislocation line sense lies parallel to the $y-axis$ and the Burgers vector (and unit cell) orientation is reflective of the desired dislocation character).*

Bravais notation the un-normalized inter-planar spacing d_* depends on the c/a ratio, and is given by $\frac{1}{{d_*}^2} = \frac{4}{3}\frac{h^2+hk+k^2}{a^2} + \frac{l^2}{c^2}$. In this way, the c-axis, and in particular, differences in the c-axis length (or the c/a ratio) for different HCP materials are taken into account. See Figure 2.A.1 in Appendix 2.A on page 69 for further explanation on why $\lambda_0 = d$ in this PFDD formulation. For the particular set up chosen here, the c-axis length is taken into account in the grid spacing normal to the slip plane (z-axis in Figure 2.2.1(a)). Accounting for the c-axis in this way is advantageous when using a cubic computational grid, as is done here. A computational cell length of $D = 256d$ was used for simulations on basal and prismatic planes, and $D = 640d$ was used for simulations modeling the pyramidal-II plane. By repeating the simulation for different cell sizes, the cell sizes used for the results that follow were determined to be sufficiently large that the dislocation structures were unaffected by the image dislocations in the periodic cells.

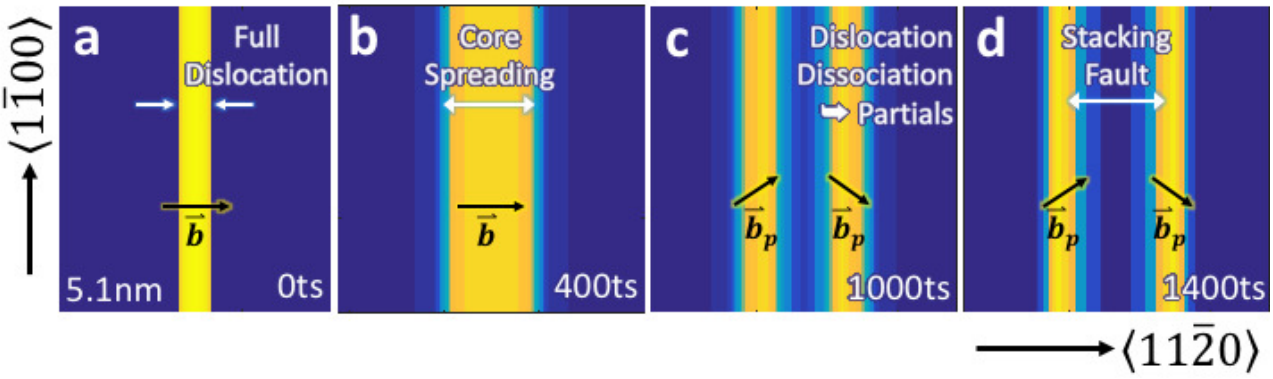

Figure 2.2.2: *Zoomed-in area of the slip plane showing the gradient of the disregistry $d\Delta/dx$ from PFDD for a basal edge dislocation in Mg as it evolves to a final equilibrium dissociated state over time: (a) 0, (b) 400, (c) 1000, and (d) 1400 time steps. The approximate side length of the area shown is 5.1 nm. The arrows labeled b and b_p are the Burgers vectors for the full and partial dislocations respectively.*

Inside the crystal, a dislocation dipole, consisting of a pair of perfect dislocations with equal and opposite sign, is initially placed on the glide plane (see Figure 2.2.1(a) and 2.2.2(a,c)). The dipole allows for a zero Burgers circuit around the simulation cell. The calculations are completed for both a perfect edge dipole and a perfect screw dipole. For the edge case, the line orientation is aligned along the y-axis and the Burgers vector along the x-axis. For the screw dipole, the line orientation is aligned along the y-axis and Burgers vector also along the y-axis. With the perfect dislocations in place on the glide plane, the simulation begins by evolving the system energy using Equation 2.1.7 to a minimum energy state. During this time, we observe that in some cases a perfect dislocation dissociates into smaller partial dislocations, which move apart in the glide plane, while in other cases, the dislocation simply spreads but does not dissociate. Since no external stress is applied in the examples here, the partial dislocations move to achieve an equilibrium structure.

To identify the displacement resulting from dislocation glide, particularly when multiple order parameters are active, we calculate the disregistry $\Delta(x)$ across the glide plane, which is defined as [3]

$$\Delta(x) = \sum_{i=1}^{3} \zeta_i(x) s_i \cdot s_p \,, \tag{2.2.1}$$

where s_p is the Burgers vector direction of the initial perfect dislocation, and s_i are the slip directions of each order parameter ζ_i on the glide plane. For instance, in the case of the basal plane, there are three order parameters, ζ_1, ζ_2, and ζ_3 (in directions $[11\bar{2}0], [1\bar{2}10], [\bar{2}110]$). Slip directions of Shockley partial dislocations ($[\bar{1}100], [0\bar{1}10], [10\bar{1}0]$) would correspond to a linear combination of ζ_1, ζ_2, and ζ_3, see Equation 2.1.15. A dislocation is located at the boundary where the disregistry $\Delta(x)$ transitions from 0 to 1 (see Figures

2.2.2(a,b)).

A dislocation results in a gradient in $\Delta(x)$. The peak in $d\Delta(x)/dx$ corresponds the central position of a dislocation and spread non-zero $d\Delta(x)/dx$ about the peak corresponds to its width (see Figures 2.2.2(c,d)). Splitting of the perfect dislocation into multiple partial dislocations of smaller Burgers vector values would correspond to multiple peaks in the final $d\Delta(x)/dx$ profile, the distance between which is quantified as the equilibrium stacking fault width SFW (which is also referred to as R_e interchangeably). In the case, where the perfect and partial dislocations are collinear (i.e., only one order parameter is active), the disregistry (Δ), calculated in Equation 2.2.1, is equivalent to the order parameter (ζ). To best visualize important structural features of the relaxed dislocations and any resulting partials and SFW we plot a zoomed in cross-section, centered around the position of the initial perfect dislocation, for both the disregistry $\Delta(x)$ and the gradient of the disregistry $d\Delta/dx$.

2.2.2 Dissociation on the Basal Plane

With the PFDD model, we simulate the dissociation of perfect edge and screw oriented dislocations along the basal plane in pure Mg. Figure 2.2.3 shows the disregistry $\Delta(x)$ profile of the final state of the edge and screw basal dislocation after the dissociation has completed. To reveal the dislocations, in the same figure, the gradient $d\Delta(x)/dx$ is also presented.

The calculation predicts that both edge and screw dislocations split into two Shockley partials, which correspond to the two peaks in the $d\Delta(x)/dx$ curve. The spread about these peaks indicates the widths of the partials, which are observed to be nearly equal. The equilibrium stacking fault width SFW (also referred to as R_e) is the distance between these peaks or the

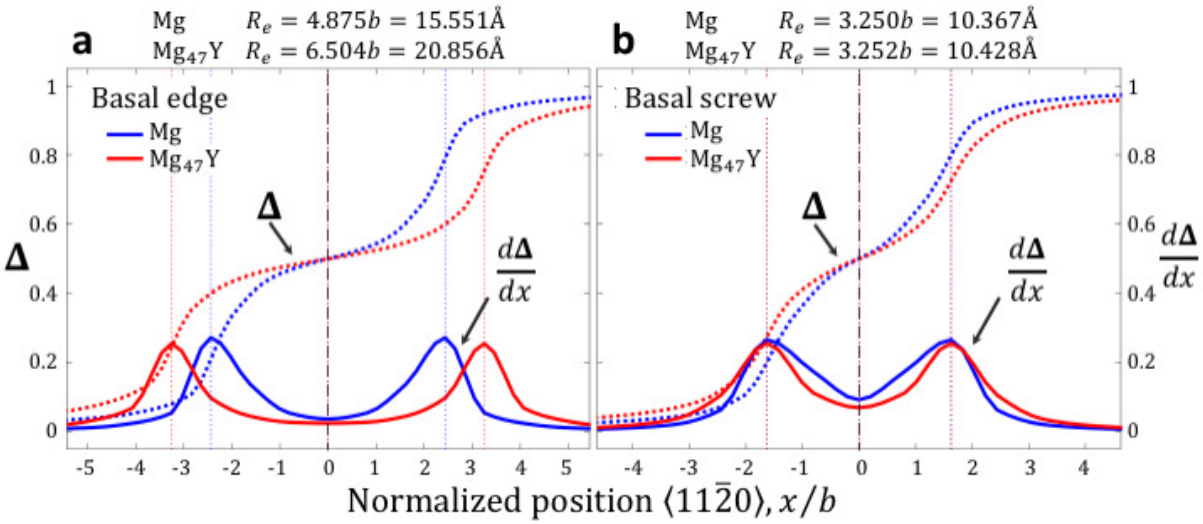

Figure 2.2.3: *Basal equilibrium stacking fault width calculations for initially (a) edge and (b) screw oriented perfect dislocations in the basal plane as determined by PFDD. Results for both pure Mg and $Mg_{47}Y$ are shown.*

center-to-center distance between the partials. Due to the grid spacing used in the PFDD calculations the error in the R_e is $\pm\, 0.5d$. As defined, a portion of the R_e includes the cores of the partials and is not comprised entirely of a perfect intrinsic stacking fault. For an edge dislocation in the basal plane of pure Mg, the $R_e = 15.551$Å $(= 4.875b)$, where $b = 3.190$Å is the Burgers vector magnitude of a dislocation on the basal plane for Mg. For the screw dislocation, $R_e = 10.367$Å $(= 3.250b)$. The dissociation of perfect edge and screw basal dislocations in $Mg_{47}Y$ are also simulated and the results included in Figure 2.2.3 for comparison. The edge dislocation dissociation results in $R_e = 20.856$Å $(= 6.504b)$, and the screw dislocation dissociation, a $R_e = 10.428$Å $(= 3.2522b)$, where $b = 3.2064$ on the basal plane for $Mg_{47}Y$. The differences in the SFWs between Mg and $Mg_{47}Y$ are negligible for the screw dislocation and $\sim$ 5 Å, just slightly less than $2b$, wider for an edge dislocation on $Mg_{47}Y$ compared to Mg. It can also be seen from $d\Delta/dx$ that

the cores of the two partials are narrower for $Mg_{47}Y$ compared to those for Mg and from $\Delta(x = 0)$ that the magnitude of the Burgers vectors for both the right and the left partials are equal.

The PFDD calculation follows the general expectation from continuum dislocation theory, which is that a perfect dislocation on the basal slip plane undergoes a planar dissociation following [12]:

$$\frac{1}{3}[1\bar{2}10] \rightarrow \frac{1}{3}[1\bar{1}00] + \frac{1}{3}[0\bar{1}10] \tag{2.2.2}$$

The above reaction indicates that a perfect dislocation will dissociate into two Shockley partial dislocations. Analogous to the dissociation of a perfect FCC dislocation on the {111} plane, the Burgers vectors of these Shockley partial dislocations on the basal plane are non-collinear and correspond to the two $\langle 1\bar{1}00\rangle$-type directions the basal γ-surface leading to the local minimum [125, 12, 18]. A force balance on this dissociated structure gives as the split distance or stacking fault width from the following analytical equation [18]

$$R_e = \frac{\mu}{2\pi\gamma_I}\left[(b_L \cdot \xi_L)(b_T \cdot \xi_T) + \frac{(b_L \times \xi_L) \cdot (b_T \times \xi_T)}{1-\nu}\right] \tag{2.2.3}$$

where γ_I is the intrinsic SFE, ν is Poisson's ratio, and b_L and b_T are the Burgers vectors of the leading and trailing partial dislocations, respectively. This expression presumes the reaction has already happened, reached the local minimum configuration, and does not consider the dissociation process that achieved it. Therefore, the only energy on the γ-surface needed is the γ_I, intrinsic stacking fault energy corresponding to the local minimum. This analytical model for Mg basal edge and screw dislocations predicts $R_e = 27.360\text{Å}$ $(= 8.577b)$ and $R_e = 13.316\text{Å}$ $(= 4.174b)$, respectively. Similarly, in the case of $Mg_{47}Y$, the analytical model produces $R_e = 27.018\text{Å}$ $(= 8.443b)$ for the split edge dislocation, and $R_e = 13.15\text{Å}$ $(= 4.109b)$ for the split screw dislocation. In both materials, the analytical model overestimates the

SFW compared to the PFDD model (see table:basalSFWs). The PFDD simulation takes into account the changes in interaction and lattice energies as the partials glide apart during the dissociation process towards its final equilibrium state, which is not known or specified *a priori*. The analytical model, in contrast, assumes an end state comprised of two distinct partial dislocations and does not account for changes in the interaction energy as the two partial dislocations move apart from each other.

Other computational approaches have been used to calculate the equilibrium structure of the basal dislocation. We compare these results with the PFDD calculations of the equilibrium SFWs for both edge and screw dislocations on the basal plane in pure Mg in Table 2.2.1. Atomic-scale simulation has been used to simulate the dissociation process, considering dynamical forces in the disassociation process, which are missing in the PFDD simulation. The data among the atomistic studies are wide spread, due to the use of different simulation cell sizes, boundary conditions, and interatomic potentials. Nevertheless, the PFDD results lie in well within this range. The SFWs reported here are notably close to DFT predictions from [19] and [17]. Our results agree well with those from the atomistic study by [20], who unlike the others in the table used the Mg EAM potential by [131]. Values for SFWs calculated by [16], using both DFT and simulations using the MEAM potential, are the lowest compared to all published DFT and EAM values. We also show estimates form GPN models, which utilize a time-dependent minimization scheme similar to the one used here. Differences between our results and GPN can be attributed to the functional form and origin of the fault energies used in the development of the $E_{lattice}$ term. Our results can be directly compared to the GPN model by [29], wherein they also used as input a full γ-surface.

Table 2.2.1: *Basal equilibrium stacking fault widths in units of Å from the dissociation of edge and screw oriented perfect dislocations along the basal plane in pure Mg reported previously in the literature and compared to values calculated with PFDD. The different methods are abbreviated as: phase field dislocation dynamics (PFDD), density functional theory (DFT), atomistic calculations that use an embedded atom method (EAM) or a modified embedded atom method (MEAM) interatomic potential, Generalized Peierls-Nabarro (GPN), and anisotropic linear elastic theory (ALET). In the PFDD calculations, the error bars correspond to 0.5d, which is error due to the grid spacing used in the calculations.*

Author	Edge (Å)	Screw (Å)	b (Å)	Method
This work	15.551 ± 1.296	10.367 ± 1.296	3.19	PFDD
	27.360	13.316		Analytical [18]
[19]	16.64	6.4	3.2	DFT
	14.4	6.4		EAM
	12.8	1.28		EAM
[17]	23.895	11.151	3.186	ALET
	22.323	12.756	3.189	DFT
[16]	7.011	4.016	3.187	DFT
	12.493	4.016	3.187	MEAM
[132]	27.2	14.016	3.2	P-N
[20]	18.816	6.912	3.2	EAM
[133]	25.6	16.416	3.2	EAM
[29]	21.312	–	3.2	GPN

2.2.3 Dissociation on the Prismatic Plane

We next apply the extended PFDD model to dislocations belonging to the prismatic slip mode. Figure 2.2.4 shows the disregistry $\Delta(x)$ and its gradient $d\Delta/dx$ profiles across the final equilibrium dislocation structure for Mg, Zr, and Ti. In the case of Mg, neither the edge nor screw dislocation dissociated, and no stacking fault region develops. The compact structure of the perfect dislocation is maintained. Stability of the compact core can be expected since the GSFE curve for Mg on the prismatic plane lacks a local minimum. This result agrees with DFT and atomistic calculations [16]. For Zr and Ti, the results from PFDD in Figure 2.2.4 indicate that the perfect dislocations dissociate into two distinct partial dislocations.

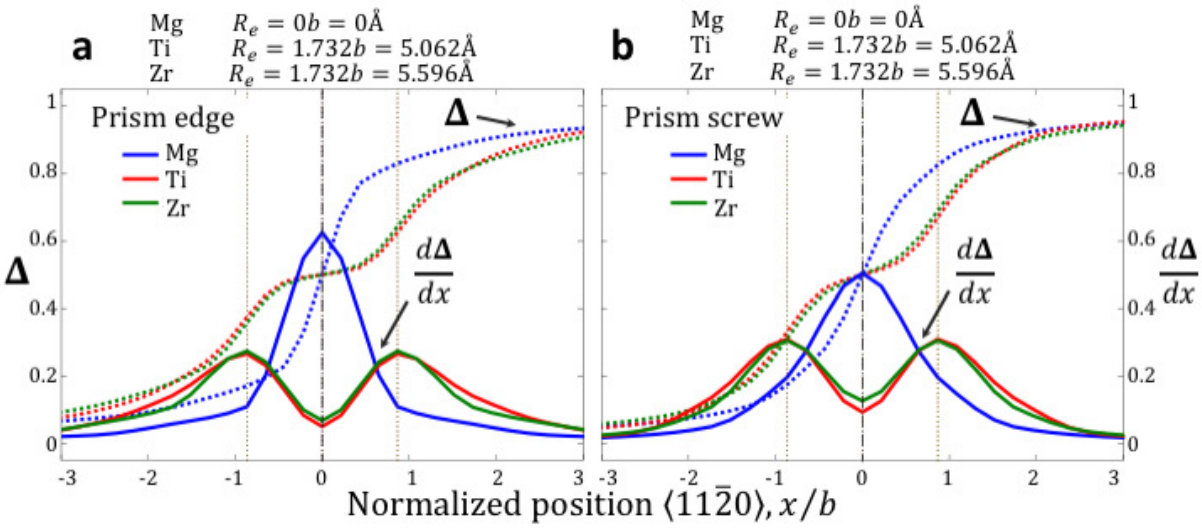

Figure 2.2.4: *Prismatic equilibrium stacking fault width calculations for initially (a) edge and (b) screw oriented perfect dislocations in the prismatic plane as determined by PFDD. Results for pure Mg, Zr, and Ti are shown.*

In the case of Zr and Ti, both perfect edge and screw dislocations dissociate into two partials, collinear of the $[1\bar{2}10]$ type and equal in Burgers

vector. The final equilibrium SFW is $R_e = 5.596$Å $(= 1.732b)$ for Zr and $R_e = 5.062$Å $(= 1.732b)$ for Ti. Neither metal exhibits a strong edge/screw character dependence. The differences between the screw and edge SFW are small and must lie within $\pm$ $0.5d$, hence significant differences are not apparent in the PFDD calculations. The structures of these dislocations are symmetric, with the cores of the partials being equal in width. In both metals, the SFW is not broad, an outcome of the shallow local energy minimum associated with formation of the stacking fault as seen in the prismatic GSFE curve 2.1.2(c). Further the core widths of the partial dislocations are relatively large compared to the SFW, suggesting that the SFW is not comprised of a homogeneous intrinsic stacking fault. For these dislocations the two partials are slightly more separated in Ti than Zr. The variations arise because the final split distances are influenced by both the repulsive elastic interactions between the partials and the local maxima and minimum in the GSFE curves. Ti has the lower peak barriers, which would lead to the wider partial cores, and it also has the higher modulus, which would lead to the stronger repulsive interaction.

From continuum dislocation theory, perfect dislocations on the prismatic slip plane are expected to dissociate following [12, 125]:

$$\frac{1}{3}[1\bar{2}10] \rightarrow \frac{1}{6}[1\bar{2}10] + \frac{1}{6}[1\bar{2}10] \tag{2.2.4}$$

As we have seen from the PFDD calculations, this dissociation is seen only to occur in Zr and Ti and not in Mg. Applying the analytical formula, Equation 2.2.3, to Zr and Ti only and using the energy minimum in the DFT GSFE curves for γ_I, the equilibrium SFWs for an edge and screw dislocation in Zr and Ti are found to be much larger than those calculated by PFDD. For Zr, the analytical model predicts $R_e = 9.730$Å $(= 3.011b)$ for edge and

$R_e = 6.071$Å $(= 1.879b)$ for screw. For Ti, the SFW values are $R_e = 10.282$Å $(= 3.518b)$ and $R_e = 6.370$Å $(= 2.179b)$ for edge and screw, respectively. The PFDD simulation takes into account the changes in interaction and lattice energies as the partials glide apart during the dissociation process towards its final equilibrium state. The analytical model, in contrast, neglects the dissociation process.

Table 2.2.2: *Prismatic equilibrium stacking fault widths in units of Å from the dissociation of screw oriented perfect dislocations along the prismatic plane in pure Zr reported previously in the literature and compared to values calculated with PFDD. The different methods are abbreviated as: phase field dislocation dynamics (PFDD), anisotropic linear elastic theory (ALET), and semidiscrete variational Peierls-Nabarro (SVPN). In the PFDD calculations, the error bars correspond to 0.5d, which is error due to the grid spacing used in the calculations.*

Author	Screw (Å)	b (Å)	Method
This work	5.596 ± 1.399 6.071	3.231	PFDD Analytical [18]
[22]	6.1	3.23	ALET
[24]	17.5	3.23	SVPN

Transmission electron microscopy (TEM) analyses of Ti and Zr suggest that screw dislocations encounter much higher Peierls barriers than non-screw dislocations, and therefore, control plastic deformation [134, 135, 136]. Published estimates for the equilibrium SFWs have focused on screw and not edge dislocations. Previous work has computed SFWs for screw dissociations on the prismatic plane in Zr using a P-N model [23, 24, 21]. When these models are informed with DFT values for the elastic constants and

γ_I, the calculations are consistent with those calculated here with PFDD (e.g., 5.9 Å and 4.6 Å reported by [21]). Other numerical approaches include anisotropic linear elastic theory (ALET) and semidiscrete variational Peierls-Nabarro (SVPN) and these are listed in Table 2.2.2. The ALET model [22] achieves reasonable agreement with PFDD, which can be expected since both approaches were informed with DFT. The SVPN result [24], however, is noticeably higher, since the system minimization is time independent, and like the analytical model, does not consider the dissociation process.

2.2.4 Dissociation on the Pyramidal-II Plane

We repeated the equilibrium SFW calculation with PFDD for dissociation of edge and screw dislocations on the pyramidal-II slip plane in Mg and Ti. The GSFE curves along the pyramidal-II slip plane have a local minimum, and we expect two collinear partial dislocations with Burgers vector in a $\langle 11\bar{2}3\rangle$ direction to form. Figure 2.2.5 shows the disregistry profiles resulting from the PFDD simulations for edge/screw dissociation in both Mg and Ti. The calculations indicate that two distinct partial dislocations form in both Mg and Ti during the PFDD simulations. For Mg, PFDD simulations calculated an equilibrium SFW of $R_e = 25.810$Å $(= 4.240b)$ and $R_e = 19.018$Å $(= 3.125b)$ for perfect edge and screw dislocation dissociation, respectively. In the case of Ti, PFDD calculates $R_e = 17.293$Å $(= 3.162b)$ and $R_e = 11.117$Å $(= 2.033b)$ for edge and screw dislocation dissociation, respectively.

A few experimental observations as well as MD simulations have reported the perfect dislocations on the pyramidal-II slip plane to dissociate into two partials equal in magnitude and collinear according to [12, 125, 15, 81, 137]:

$$\frac{1}{3}[2\bar{1}\bar{1}3] \rightarrow \frac{1}{6}[2\bar{1}\bar{1}3] + \frac{1}{6}[2\bar{1}\bar{1}3] \tag{2.2.5}$$

Edge and screw $\langle c+a \rangle$ dislocation dissociation distances have been modeled with DFT, using a cluster approach with fixed boundary conditions (edge) and flexible boundary conditions (screw) but only in Mg, with calculated stacking fault widths of $\sim$ 18Å and $\sim$ 16Å respectively [137]. Figure 2.2.5 shows the PFDD calculated dissociation distances for edge and screw dislocations on the pyramidal II plane in Mg and Ti. The results for Mg are larger than those previously mentioned from literature (43% greater for edge and 18.8% greater for screw).

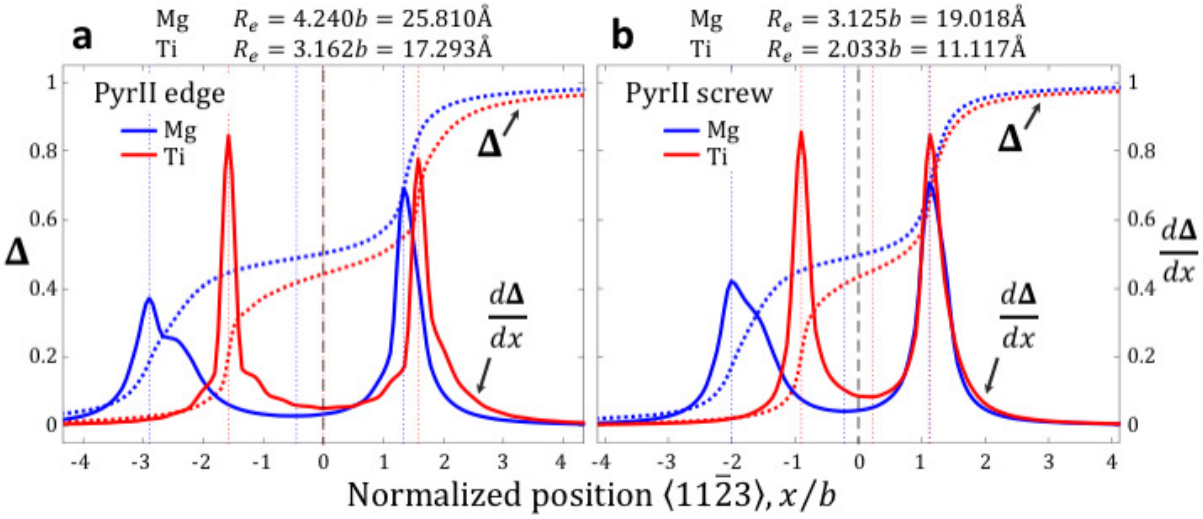

Figure 2.2.5: *Pyramidal-II equilibrium stacking fault width calculations for initially (a) edge and (b) screw oriented perfect dislocations in the pyramidal-II plane as determined by PFDD. Results for both pure Mg, and Ti are shown.*

In the case of Mg, DFT has previously calculated the equilibrium SFW for both edge and screw dislocations on the pyramidal-II slip plane, as shown in Table 2.2.3. The equilibrium SFW as calculated with PFDD for both the edge and screw dislocation dissociation reactions are slightly higher than DFT and analytical calculations, but compare well with those determined with DFT. We also note that there are further variations among the DFT

Table 2.2.3: *Pyramidal-II equilibrium stacking fault widths in units Å from the dissociation of edge and screw oriented perfect dislocations along the pyramidal-II plane in pure Mg reported previously in the literature and compared to values calculated with PFDD. The different methods are abbreviated as: phase field dislocation dynamics (PFDD), and density functional theory (DFT). In the PFDD calculations, the error bars correspond to 0.5d, which is error due to the grid spacing used in the calculations.*

Author	Edge (Å)	Screw (Å)	b (Å)	Method
This work	25.810 ± 0.679 22.155	19.018 ± 0.679 15.632	6.087	PFDD Analytical [18]
[137]	18.3	16.6	6.106	DFT
[69]	–	14	6.0827	DFT
[15]	22.6	–	6.089	DFT

results, possibly due to the use of different exchange correlation functionals and k-points, supercell sizes, initial dislocation configuration, and method of defining the SFW width. To the authors' knowledge, equilibrium SFW calculations have not been previously reported for edge or screw dislocation dissociations along the pyramidal-II plane in Ti.

Interestingly, the disregistry gradient $d\Delta/dx$ in Figure 2.2.5 shows that the dissociated dislocations in Mg have an apparent asymmetry between the core widths of the two partials. The left partial has a much wider ($\sim$ 2.5 times wider) core than the right partial. Differences in the widths of the individual partials (partial core spreading) in the split pyramidal-II dislocation in Mg have also been reported in atomistic molecular dynamics calculations using

the MEAM potential [16, 15]. The distances these two partials glide during the dissociation are also unequal as well, with the left partial moving further to the left than the right partial. In the case of Ti, the partial core widths are not as dissimilar as in Mg, and the differences between the distances the right and left partial glide during the dissociation is less than that in Mg and favors glide of the right partial more than the left.

We surmise that the asymmetries in the Mg and Ti dislocation cores arise from the asymmetry of the positions and critical energetic values in their GSFE curves. First we consider the Burgers vectors of the two partials. The reaction in Equation 2.2.5 suggests that the dissociation leads to two partials of equal Burgers vector. From the PFDD calculated core structure, we can determine the magnitude of the Burgers vector from the value of the disregistry Δ at $x = 0$. For Mg $\Delta(0)$ is ~ 0.5 and thus we can expect a dislocation split into partials with equal Burgers vectors, consistent with Equation 2.2.5. For Ti, however, $\Delta(0)$ is ~ 0.45, meaning the left and right partials have a Burgers vector magnitude of $0.45b$ and $0.55b$ respectively, where b is the magnitude of the Burgers vector for the initial perfect dislocation. This asymmetry in the partial Burgers vector value is governed by the displacement needed to achieve the local minimum or intrinsic stacking fault energy I in the GSFE curve in Figure 2.1.2(d) and 2.2.6. As shown in Figure 2.2.5, unlike Mg, the Burgers vectors of the two dissociated pyramidal dislocations in Ti are not equal in magnitude.

It is noticed that the partial with the wider core is associated with the lower unstable stacking fault peak U_1 (left) and the narrower one with the higher unstable stacking fault peak U_2 (right) in the GSFE curve (see Figure 2.1.2(d) and 2.2.6). During the dissociation process, the lower peak barrier would pose less resistance to partial dislocation glide, permitting core spread-

ing. For Ti, with the more symmetrical core structure the difference between the peak barriers in the Ti GSFE curve is comparatively smaller, apparently leading them to only a slight asymmetry between the core widths of the left and right partials.

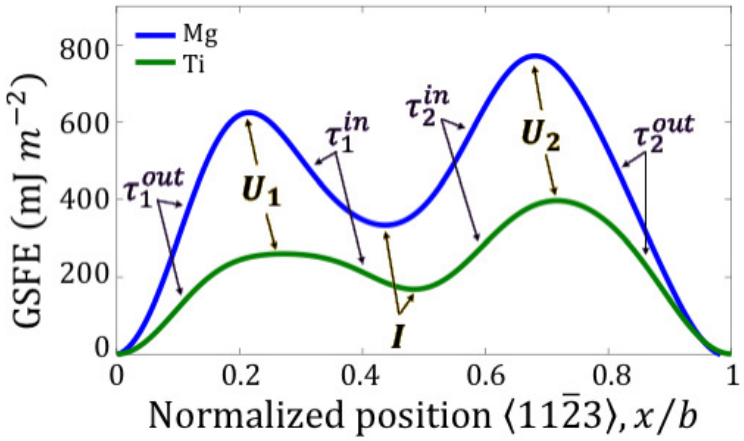

Figure 2.2.6: *Pyramidal-II GSFE curves for both Mg and Ti showing labels for critical energetic points and the peak shear stresses as the slopes leading to and from these points.*

Related to the peak energies U is the peak shear stress required to move the partial dislocations apart during the dissociation. These critical stresses are calculated directly from the derivative of the GSFE curves with respect to the displacement shift. The left partial would follow the energetic path starting from the reference point (global minimum at 0 shift) to U_1, whereas the right partial would follow a path associated with the right most reference point (global minimum at 1 to the peak U_2). The ideal shear stress associated with the resistance for the left partial to move is τ_1^{out} is the maximum slope from a global minimum to U_1, and that for the right partial is τ_2^{out}, the maximum slope from the global minimum to U_2. The local minimum in the GSFE corresponds to the stacking fault formed by the glide of the partials.

The peak slopes on either side of the local minimum, $\tau_1^{in} and \tau_2^{in}$, are related to the resistance for the core of the partials to spread in plane. With interest in the effect of asymmetries in the GSFE with asymmetries in core structures, we analyze the ratios of these ideal shear stresses. Table 2.2.4 shows the four peak slopes and the ratios of $\tau_2^{out}/\tau_1^{out}$ and τ_2^{in}/τ_1^{in} as well as τ_1^{out}/τ_1^{in} and τ_2^{out}/τ_2^{in} for Mg and Ti.

Table 2.2.4: *The relationships between the absolute values for the maximum slopes between the global and local maxima and minima of the GSFE curves for the pyramidal-II planes of Mg and Ti as shown in Figure 2.1.2(d).*

Material	τ_1^{out}	τ_1^{in}	τ_2^{in}	τ_2^{out}	τ_1^{out}/τ_1^{in}	τ_2^{out}/τ_2^{in}	τ_2^{in}/τ_1^{in}	$\tau_2^{out}/\tau_1^{out}$
Mg	16.85	6.29	15.50	24.03	2.68	1.55	2.47	1.43
Ti	50.24	21.38	30.28	36.36	2.35	1.20	1.42	0.72

According to Table 2.2.4, $\tau_2^{out}/\tau_1^{out}$ for Ti is less than unity, suggesting that it will be easier for the right partial to glide right than the left partial to glide left. As seen in the PFDD calculated core structure of the dissociated screw dislocation in Figure 2.2.5(b), the left partial moves $\sim 0.9b$ left and the right partial moves $\sim 1.1b$ right. Conversely, for Mg $\tau_2^{out}/\tau_1^{out}$ is greater than unity, suggesting that it will be far easier for the left partial to glide left than the right partial to glide right. Accordingly, the core of the Mg pyramidal dislocations as calculated via PFDD finds that the left and right partials move $\sim 2.9b$ and $\sim 1.3b$, respectively for the dissociated edge dislocation and $\sim 2.0b$ and $\sim 1.1b$, respectively for the dissociated screw dislocation.

Once the SF has formed, whether or not the spreading of a partial dislocation core occurs is governed by τ_2^{in}/τ_1^{in}. Referring to Table 2.2.4, while τ_2^{in}/τ_1^{in} exceeds unity for both Ti and Mg, it is much higher in Mg than that for Ti, indicating that core spreading is more likely in one partial dis-

location in Mg than Ti. Further, the ratios τ_1^{out}/τ_1^{in} and τ_2^{out}/τ_2^{in} indicate which partial dislocation is likely to experience this spreading. According to these values for Mg, we would anticipate spreading of the left partial core. In agreement, in simulation, the left partial in the pyramidal core of Mg is found to broadened widely, more so than the right one.

These GSFE sensitive dislocation core structures on the pyramidal II plane is explored more in depth in the next chapter, where the next stage of PFDD model development to include elastic anisotropy is used to simulate dislocation behavior in 10 different HCP materials (See Chapter 3 on page 71)

2.3 Summary

This work presents model extensions to advance a phase field approach for studying dislocation motion, called phase field dislocation dynamics (PFDD), to include crystals with a hexagonal close packed (HCP) crystal structure. The functional form of the lattice energy was modified to include periodic potentials that depend on slip mode. In this way, the significant differences seen in the γ-surfaces and GSFE curves on different HCP slip planes, as determined with atomistic approaches, can be represented. The new periodic potentials are directly informed by generalized stacking fault energy (GSFE) curves calculated with density functional theory (DFT), either calculated here or adopted from previously published DFT data. For instance, the γ-surface for the basal slip plane in Mg and the GSFE curve for the pyramidal-II slip plane in Ti are presented here.

With the model, we calculate the equilibrium SFWs for both edge and screw dislocations in various HCP metals, including pure Mg, $Mg_{47}Y$, Ti,

and Zr, and on the basal, prismatic, and pyramidal-II slip planes. These examples illustrate the flexibility of the model formulation, as well as permit direct comparison with calculations of equilibrium SFW by other computational approaches, such as atomistic and other continuum approaches previously reported in the literature. For example, the method is able to capture both the compact dislocation core on the prismatic plane in Mg, and also the dissociated dislocation core on the prismatic plane in Zr and Ti. In all cases, the PFDD results show reasonable comparison to results previous reported using MD or DFT. Since PFDD was informed with DFT GSFE information, best comparisons are generally found with DFT calculated values, or GPN models also informed with DFT information. In addition, results were compared to analytical calculations of the equilibrium SFW [18]. In all cases, the analytical values were larger than those determined by PFDD. The analytical equation does not fully account for the dissociation process, including energy barriers partials must overcome as they spread apart through the crystal lattice. In addition, it is worth noting that in some cases, such as screw and edge dislocations in Zr and Ti on the pyramidal-II plane, data for the equilibrium core structures were not available in the current literature for comparison.

In simulating the dissociation process from an initially unstable perfect dislocation to its final equilibrium structure, the PFDD model revealed additional effects of the displacements and values of energetic local maxima and minima of the GSFE curve. The most pronounced example arose when considering the structure of dislocations on the pyramidal-II plane, which has an asymmetrical GSFE curve. In the case of Mg, the PFDD results show that the width of the left partial is nearly three times wider than the right partial, for a dissociated edge dislocation. It is also shown that while

the Burgers vectors for the partial dislocations are equal in magnitude, the left partial glides farther than the right partial. Consequently, the left partial contributes more to the total SFW than the right partial. These results are in agreement with previous work using atomistic calculations with the MEAM potential, which also found an asymmetry in the width of individual partials along the pyramidal-II plane in Mg [16, 15]. With the aid of PFDD calculations with designed GSFE curves, we identify the relationships between the asymmetries in the GSFE curve and the asymmetries in the equilibrium core structure of the dislocation, namely distances traveled by the two partials as they glide apart during the dissociation and in the core widths and values of the Burgers vectors of the two partial dislocations, explaining why the extended dislocation structures exhibit significant differences in asymmetry between Mg and Ti. On the other hand, while Ti also has a GSFE curve that possesses some asymmetries, its pyramidal dislocation core structure bears less asymmetric characteristics than the Mg pyramidal dislocation core. Our analysis reveals that the partials in Ti have Burgers vectors with different magnitudes that correspond to the position of the intrinsic stacking fault energy, such that the left partial has a smaller Burgers vector than the right partial.

We mention that other dislocations have been reported in HCP materials. In both Zr and Ti, another important pyramidal slip system is pyramidal type I, which has twelve slip systems. For Mg, whether this system is as active or more active than the pyramidal type II mode studied here has been a point of debate. This is a potential area for future work with the newly extended HCP-PFDD model.

HCP metals, particularly in pure form, as studied here, tend to twin easily when the c-axis of the crystals are stretched or compressed. The role

of dislocations in the formation of deformation twin nuclei has been studied predominantly using dislocation theory and atomistic simulation [138, 139, 140, 141]. It has been suggested that twin embryo formation begins with the stress-induced dissociation of linear defects with relatively large Burgers vectors, such a pyramidal dislocation or pile up of basal dislocations [73, 142, 143]. While in this study we do not simulate twin formation, we simulate the dissociation process of individual dislocations. These calculations would be fundamental to further calculations of dislocation reactions among many dislocations with the PFDD model presented here.

2.4 Copyright

Appendix

2.A Grid spacing in HCP

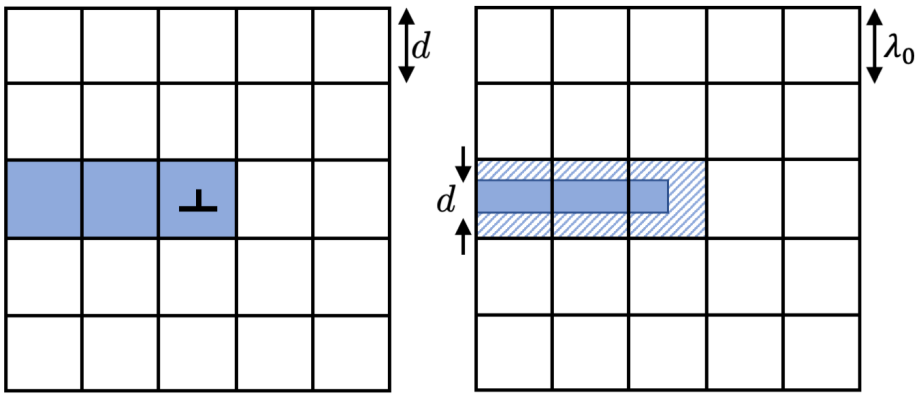

Figure 2.A.1: *The c-axis must be accounted for since we are no longer dealing with a cubic lattice structure. The grid spacing, λ_0, is chosen to be the interplanar distance of the slip plane, d. Where d for any hcp slip plane given in (hkil) or (hk.l) Miller-Bravais notation follows*

$$\frac{1}{d^2} = \frac{4}{3}\frac{h^2 + hk + k^2}{a^2} + \frac{l^2}{c^2}.$$

This figure is adapted from [3].

In Figure 2.A.1 we see a distribution of ζ values on the cross-section plane of a perfect/compact edge dislocation in a finite difference mesh used in the phase field model, where the filled area ($\zeta = 1$) represents the slipped region

and the white areas ($\zeta = 0$) is the unslipped region. By definition, a cell filled with $\zeta = 1$ indicates a stress-free shear strain, $\epsilon = b/d$. When $\lambda_0 = d$, the relative displacement of the top to the bottom of the cell is $\lambda_0 b/d = b$ and therefore the boundary cell, where $\zeta = 1$, bordering the slipped and unslipped regions contains a single dislocation with Burgers vector b. If a larger scale meshing is used, as depicted in the right figure, where $\lambda_0 > d$, the hatched region is the 'resolvable ζ distribution, however the actual distribution is the solid region and the displacement becomes $\lambda_0 b/d \neq b$, or equivalently the boundary cell contains λ_0/d dislocations with Burgers vector b, which is inconsistent with the definition of ζ.

Chapter 3

Asymmetric equilibrium core structures of pyramidal-II dislocations in ten HCP materials

In this stage of the PFDD development, published in Reference [2], we employ an elastically anisotropic version of the PFDD approach, developed by a Beyerlein group member (PostDoc Shuozhi Xu) and published in Ref. [95], to compute the equilibrium structures of pyramidal-II $\{\bar{1}\bar{1}22\}\langle 11\bar{2}3\rangle$ dislocations in ten HCP metals: Be, Co, Mg, Re, Ti, Zn, Cd, Hf, Y, and Zr. All input parameters including the lattice parameters, elastic constants, and GSFE curves are computed from first principles to avoid any dependence on interatomic potentials. These ten metals exhibit anisotropic elasticity to varying degrees [7]. For the DFT GSFE calculations, we apply the same method with full relaxation to all ten and show that their energetic landscapes exhibit with a single local minimum and two unequal maxima, featuring a wide

range of intrinsic SFEs. We show that achieving a single local minimum in the GSFE for Co requires accounting for its ferromagnetic properties.

In all these metals, the $\langle c+a \rangle$ pyramidal dislocations dissociate into two partials that separate in plane, creating extended structures, with nm-sized splitting distances. For the screw dislocation, Zn has the widest splitting distance and Ti the narrowest, and for the edge dislocation, Hf has the widest and Be the narrowest. Considering all ten metals, the separation distances scale inversely with the normalized intrinsic SFE, $I/(Kb)$, where K is an anisotropic energy factor dependent on elastic constants and dislocation character. In most cases, the dislocation partial core widths and Burgers vectors are not ideally equal. These asymmetries in the dislocation structures can be explained by deviations in the $\{\bar{1}\bar{1}22\}$ GSFE landscape from that expected of a metal with an ideal c/a ratio and symmetric landscape. Metals with higher levels of elastic anisotropy have wider separation distances for both screw and edge character dislocations than expected with effective isotropic constants, being 20–35% broader for Zn, which is highly anisotropic but having no effect on Re, Y, and Mg, which are all nearly isotropic. These findings on the equilibrium structure of $\langle c+a \rangle$ pyramidal-II dislocations across a broad range of HCP metals are important for understanding their motion and interactions with other dislocations or interfaces.

3.1 Computational Methods

3.1.1 DFT Methodology and Calculations

For all DFT calculations here, we use the Vienna *Ab-initio* Simulation Package (VASP) [126, 127] and utilize the generalized gradient approximation for the exchange correlation functional with the Perdew-Burke-Ernzerhof param-

eterization [128]. The interaction between valence electrons and ionic cores is treated using projector augmented wave potentials. The number of valence electrons for each material can be found in Table 3.1.1. A plane wave energy cutoff of 400 eV is employed and the structure is optimized until the force on each atom became smaller than 0.01 eV/Å. We use a $19 \times 19 \times 19$ Gamma-centered Monkhorst Pack k-point mesh to integrate the Brillouin Zone of the primitive HCP unit cells to calculate the lattice parameters and elastic constants. For the GSFE curves, we adopted a $17 \times 13 \times 1$ k-point mesh. The k-point mesh was sufficiently dense that the convergence of total energy was less than 1 meV per atom with respect to a change in mesh size [144, 145]. We confirmed that higher values of energy cut off (up to 500 eV) and finer k-point grids do not lead to significant differences in the constants or GSFEs. All supercells contain a thick vacuum layer of 15 Å along the z-direction. Among these ten metals, Co is a well known ferromagnetic material [146]. So we also identify the effect of ferromagnetic (FM) ordering in Co on the lattice parameters, elastic constants, and GSFE through comparisons with those calculated without magnetism (NM).

The lattice parameters and elastic constants calculated via DFT are presented in Table 3.1.2. Overall, these quantities are in good agreement with previous DFT calculations and experimental measurements (see Table 3.B.1 in Appendix B) [77, 15]. For all HCP metals, we confirmed that the calculated elastic constants satisfy $2C_{66} = C_{11} - C_{12}$, indicating transversely isotropic elasticity with five independent constants.

In addition to the lattice parameters and elastic constants, PFDD also utilizes $\{\bar{1}\bar{1}22\}$ GSFE curves in order to calculate the equilibrium dislocation core structures. For this work, the GSFE is the excess potential energy incurred when one crystal half is sheared relative to the other half across the

Table 3.1.1: *Number of valence electrons in pseudopotential used in DFT calculations and dimensions of supercell for pyramidal-II GSFE calculations in Å. Number of atoms is 60. Number of planes along the z-direction is 30, which is sufficiently large according to prior work in FCC [5] and BCC metals [6].*

Material	No. of valence electrons	Supercell dimensions (x, y, z)
Be	2	(3.923, 4.226, 38.544)
Mg	2	(5.525, 6.089, 51.488)
Y	11	(6.316, 6.777, 58.547)
Ti	4	(5.063, 5.467, 51.960)
Zr	4	(5.596, 6.100, 51.392)
Hf	4	(5.529, 5.965, 52.832)
Re	7	(4.800, 5.264, 47.134)
Co (NM)	9	(4.259, 4.658, 42.835)
Co (FM)	9	(4.316, 4.746, 43.524)
Zn	12	(4.614, 5.594, 46.894)
Cd	12	(5.255, 6.410, 52.345)

pyramidal-II $\{\bar{1}\bar{1}22\}$ plane. The relevant direction of shearing on this plane is the $\langle 11\bar{2}3\rangle$ direction, the slip direction along which the local maxima and minimum usually lie. Many details of these lattice energy curves can affect the core structure, and for this reason, we employ DFT for its calculation, as opposed to MS or a hypothetical function. To do so, we use the relaxed method [15], wherein for each displacement step, minimization of the energy of the system is ensured by fixing all atomic positions along the glide direction

Table 3.1.2: *Lattice parameters (in Å) and elastic constants (in GPa) for the ten HCP metals obtained from DFT and isotropic shear modulus μ (in GPa), and Lamé parameter, λ (in GPa).*

Material	a	c/a	C_{11}	C_{12}	C_{13}	C_{33}	C_{44}	C_{66}	μ	λ
Be	2.265	1.5760	303	36.7	12.5	380.1	165.2	133.2	154.35	20.38
Mg	3.190	1.6250	63.3	25.9	20.8	65.7	18	18.7	19.26	23.53
Y	3.648	1.5660	74	24.4	21.3	78.1	25.2	24.8	25.65	22.91
Ti	2.923	1.5810	159.4	108.9	83.9	191.7	37.6	25.2	35.67	94.43
Zr	3.231	1.6010	135.1	80.3	70.7	166.1	26.1	27.4	30.23	77.59
Hf	3.192	1.5790	183.4	83.1	72.5	206.1	52.6	50.1	54.05	78.31
Re	2.773	1.6130	617.9	281	233.4	678.6	165.4	168.4	177.61	260.48
Co (NM)	2.459	1.6090	424.2	161.1	151.6	457.6	84.8	131.6	116.35	170.72
Co (FM)	2.492	1.6208	359.2	164.8	109.3	406.4	93.1	97.2	106.11	139.44
Zn	2.664	1.8470	154.3	38.4	48.4	63.9	30.4	58	39.58	45.05
Cd	3.034	1.8610	76.8	42.1	34.1	45.6	7.8	17.3	12.51	38.31

and allowing those along the plane normal and the in-plane direction lying normal to the glide direction to relax. Fine displacement intervals were used to precisely locate the local minimum. Note that with the same DFT model design, the GSFE curves or surfaces for the basal, prismatic, and two types of pyramidal planes in Mg, Zr, and Ti have been previously calculated [1, 124, 15]. Here, we extend the pyramidal-II GSFE calculations for all ten HCP metals

Figure 3.1.1(a) presents the calculated GSFE curves for all ten HCP metals. We observe that all curves have two pronounced local maxima, denoted

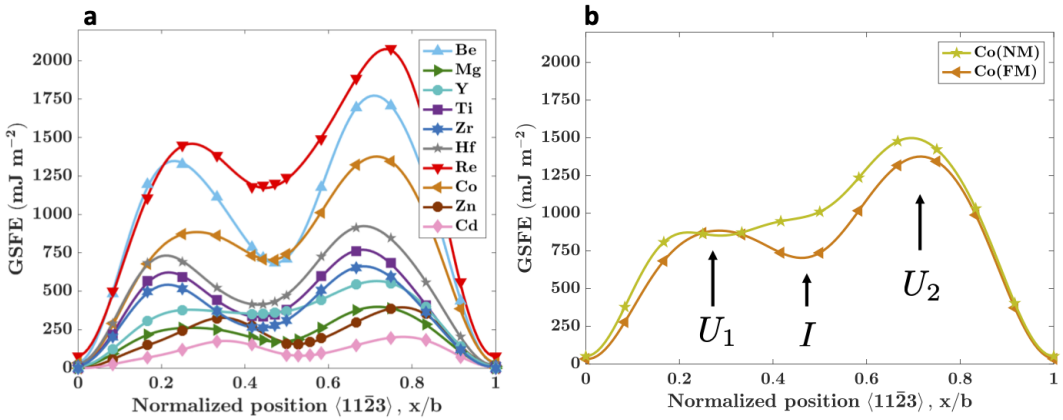

Figure 3.1.1: *Comparison of GSFE profiles for (a) the pyramidal-II plane in ten HCP metals as determined by DFT, and (b) for Co with and without magnetism considered in the DFT simulations. In Figure (a), the GSFE curve for Co is shown with the effect of ferromagentism considered. The unstable SFEs, $U_{1,2}$, and intrinsic SFE, I, are labeled in (b).*

as the unstable SFEs, U_1 and U_2, and a local minimum, well known as the intrinsic SFE I. To ensure the local minimum indeed lies along the GSFE curve, the full pyramidal-II GSFE surface of Mg was calculated with DFT (see Figure 3.A.1 of Appendix A). Compared to prior pyramidal-II GSFE curves, the results in Fig. 3.1.1 are similar with the exception of Cd [17]. Differences could be attributed to more atoms in the present supercell ($\approx$ 60) but coarser k-point grid.

The relative shear displacement x_I/b across the plane corresponding to I leads to a meta-stable stacking fault. Table 3.1.3 summarizes the values for I, U_1, U_2, and x_I/b. In all metals, the two peak energies, U_1 and U_2, belonging to the same landscape, are unequal with $U_2 > U_1$. The local minimum x_I/b displacement is shifted from the ideal $x_I/b = 0.5$, a reflection of the anisotropy in bond length. In low symmetry HCP metals, the bond lengths are generally unequal for all planes. When $c/a = \sqrt{8}/3 = 1.633$,

all twelve nearest neighbors of an atom in the double lattice structure are equidistant. Only one of the ten HCP metals, Mg, possesses a nearly ideal c/a ratio, and accordingly, its $x_I/b = 0.49$. Two metals, Zn and Cd, have c/a ratios greater than ideal, leading to $x_I/b > 0.5$. All remaining metals have below ideal c/a ratios and $x_I/b < 0.5$.

Table 3.1.3: *The unstable SFEs, U_1 and U_2 and the intrinsic SFE, I for ten HCP metals. Their normalized locations are also shown. All energies are expressed in units of $mJ{\cdot}m^{-2}$, and positions are normalized with the Burgers vector magnitude in the $[11\bar{2}3]$ direction, b.*

Material	U_1		I		U_2	
	$mJ{\cdot}m^{-2}$	x_{U_1}/b	$mJ{\cdot}m^{-2}$	x_I/b	$mJ{\cdot}m^{-2}$	x_{U_2}/b
Be	1335.7	0.23	678.2	0.47	1768.6	0.71
Mg	262.9	0.27	168.1	0.49	397.4	0.72
Y	380.1	0.27	352.3	0.42	565.6	0.71
Ti	617.8	0.21	332.1	0.44	764.2	0.68
Zr	538.5	0.21	260.2	0.44	658.2	0.69
Hf	730.2	0.20	411.9	0.43	919.6	0.69
Re	1468.1	0.27	1168.0	0.44	2088.8	0.74
Co (NM)	870.0	0.21	857.3	0.30	1502.5	0.69
Co (FM)	889.6	0.29	702.2	0.45	1381.2	0.71
Zn	324.3	0.35	150.3	0.52	393.4	0.78
Cd	174.4	0.36	78.2	0.53	202.3	0.79

Figure 3.1.1(b) examines more closely the GSFE curves for Co calculated with and without ferromagnetic ordering. The effect of magnetism on the

GSFE is found to be significant. Without magnetism, the GSFE possesses no pronounced local minimum, but with magnetism, it has a single local minimum at $x_I/b = 0.45$, like the other nine HCP metals. The peak energy U_2 also reduces with magnetism by 8%. Table 3.1.2 shows that magnetism increased the lattice parameter a and the c/a ratio and decreased the elastic constants C_{11}, C_{13} and C_{33}. A similar effect of magnetism on a was reported in prior studies of cubic metals, namely Cr [96], Fe [147], and Ni [5]. More importantly, the values for the elastic moduli determined with ferromagnetism achieve better agreement with the experimentally measured values, which are presented in Table 3.B.1 in Appendix B. Hereinafter, PFDD calculations in this paper will use the GSFE curve, lattice parameters, and elastic moduli calculated for Co from DFT with ferromagnetism considered.

3.1.2 PFDD formulation

As is fundamental in phase field approaches, this method relies on the evolution of one or more order parameters through the minimization of the total system energy. For phase field approaches formulated to study the motion and interaction of dislocations, the order parameters, ζ, represent the location of and area traveled by dislocations within the system [90, 111, 89]. The order parameters are defined by slip systems within a material, and hence the number of order parameters varies with the crystallography of the material under study. Defined in this way, the set of ζ is used to describe the plastic strain as

$$\epsilon_{ij}^{p} = \frac{1}{2}\sum_{\alpha=1}^{N_{\text{op}}} \frac{b_\alpha}{d_\alpha}\zeta_\alpha(\mathbf{x},t)\delta_\alpha(s_i^\alpha m_j^\alpha + s_j^\alpha m_i^\alpha). \tag{3.1.1}$$

where the sum is taken over all slip systems α from 1 to N_{op} included in the material, b_α is the magnitude of the Burgers vector on the slip plane

of interest, d_α is the interplanar distance for the active slip plane, δ_α is the Dirac distribution supported on the slip plane, $\mathbf{m}$ is the slip plane normal, and $\mathbf{s}$ is the normalized slip vector. In many crystals, multiple systems share the same plane; therefore, while d_α is defined with each slip system α, slip systems on the same slip plane will share the same d_α.

In the PFDD method, the order parameters evolve through the minimization of the total system energy density, E, dictated at each time step via the time-dependent Ginzburg-Landau (TDGL) equation

$$\frac{\partial \zeta_\alpha(\mathbf{x}, t)}{\partial t} = -L \frac{\delta E(\zeta)}{\delta \zeta_\alpha(\mathbf{x}, t)} \tag{3.1.2}$$

where L, which is related to the convergence speed of the system, is a non-negative coefficient that is constant and set to unity here for all order parameters. For calculations involving multiple order parameters, Equation 3.1.2 becomes a set of N coupled integro-differential equations that must be solved numerically to evolve the system. In the dislocation problems of interest for this work, the total free energy density of the system consists of two contributions [90, 31]:

$$E = E^{\text{strain}} + E^{\text{lattice}} \tag{3.1.3}$$

where E^{strain} is the elastic strain energy density generated by the presence of dislocations in the system and interactions between these dislocations. The lattice energy density, E^{lattice}, describes the energy expended as a dislocation glides through the crystal lattice breaking and re-forming atomic bonds. Under an external stress, a third term for the work done to the system through an applied stress would be included. However, for the problems in this work, no external stress is applied. In addition, past PFDD formulations have included a gradient energy term, representing the energy density stored in the partial dislocation cores in FCC metals [94]. It tends to increase the

partial dislocation core size in better agreement with MS [94, 148]. With its basic effect qualitatively understood, we refrain from adding the gradient energy term in the present application since it requires an additional material-dependent coefficient. We note that in this case, without the gradient energy term, the PFDD formulation employed is equivalent to a GPN model [92]. We emphasize that the GPN model has not yet been applied to the problem of pyramidal-II dislocation cores, to our best knowledge.

The elastic strain energy density, E^{strain}, which is commonly expressed in terms of the elastic strain, can also be expressed in terms of the plastic strain [90]:

$$E^{\text{strain}} = \frac{1}{(2\pi)^3}\frac{1}{2}\hat{A}_{mnuv}(\mathbf{k})\hat{\epsilon}^{p}_{mn}(\mathbf{k})\hat{\epsilon}^{p*}_{uv}(\mathbf{k})d^3k \tag{3.1.4}$$

where a superposed ($\hat{}$) denotes the Fourier transform, $\hat{A}_{mnuv}(\mathbf{k}) = C_{mnuv} - C_{kluv}C_{ijmn}\hat{G}_{ki}(\mathbf{k})k_jk_l$, $\mathbf{k}$ is the wavenumber vector, $\hat{G}_{ki}(\mathbf{k})$ is the Fourier transform of the Green's tensor of linear elasticity, $\int$ denotes the principal value of the integral, C_{ijkl} is the elastic moduli tensor and the superscript $(*)$ denotes the complex conjugation.

In order to examine the effect of HCP anisotropy, we will use the elastic moduli tensor and the Green's tensor for either a transversely isotropic or ideally isotropic material in the calculations. The elastic stiffness tensor for both a transversely isotropic hexagonal system, $\boldsymbol{C}^{\text{a}}$, and an isotropic system, $\boldsymbol{C}^{\text{i}}$, can be given in compact matrix notation by:

$$\boldsymbol{C}^{\mathrm{a}} = \begin{bmatrix} C_{11} & & & & & & \\ C_{12} & C_{11} & & & & & \\ C_{13} & C_{13} & C_{33} & & \text{Symm} & & \\ & & & C_{44} & & & \\ & & & & C_{44} & & \\ & & & & & C_{66} & \end{bmatrix}$$

$$\boldsymbol{C}^{\mathrm{i}} = \begin{bmatrix} \lambda+2\mu & & & & & & \\ \lambda & \lambda+2\mu & & & & & \\ \lambda & \lambda & \lambda+2\mu & & \text{Symm} & & \\ & & & \mu & & & \\ & & & & \mu & & \\ & & & & & \mu & \end{bmatrix} \tag{3.1.5}$$

where $2C_{66} = C_{11} - C_{12}$, μ is the shear modulus, and λ is Lamé's first constant. We utilize a Voigt average to determine the two isotropic constants from the five transversely isotropic constants (Table 3.1.2), using [63]

$$\mu = \frac{1}{30}[7C_{11} - 5C_{12} + 2C_{33} + 12C_{44} - 4C_{13}] \tag{3.1.6}$$

$$\lambda = \frac{1}{15}[C_{11} + C_{33} + 5C_{12} + 8C_{13} - 4C_{44}] \tag{3.1.7}$$

whose values are also included in Table 3.1.2.

The lattice energy E^{lattice} depends on the material and, in some cases, such as HCP and BCC metals, the lattice energies of more than one type of crystallographic plane are of interest [1, 96]. In general, E^{lattice} can be written as [90, 1]:

$$E^{\text{lattice}} = \sum_{\beta=1}^{N_{\text{p}}} \int \frac{1}{d_\beta} \phi_\beta(\zeta_1(\mathbf{x}), \zeta_2(\mathbf{x}), ..., \zeta_N(\mathbf{x})) d^3x \tag{3.1.8}$$

where $\phi_\beta(\zeta_1(x), \zeta_2(x), ...)$ is a periodic potential for slip plane β on up to N_p planes.

3.1.3 PFDD model for $\langle c+a \rangle$ pyramidal dislocations

Here we consider a straight dislocation belonging to a pyramidal-II $\langle c+a \rangle$ slip system. Hence, $N_\mathrm{op} = 1$, $N_\mathrm{p} = 1$, and $\alpha = \beta = 1$. In what follows, we drop the subscripts α and β. For the periodic potential of the pyramidal-II plane, the following continuous function, proposed in Ref. [1], is adopted:

$$\begin{aligned}\phi(\zeta) = p_0 &+ p_1\cos(2\pi\zeta) + p_2\cos(4\pi\zeta) + p_3\cos(6\pi\zeta) + p_4\cos(8\pi\zeta) \\ &+ q_1\sin(2\pi\zeta) + q_2\sin(4\pi\zeta) + q_3\sin(6\pi\zeta) + q_4\sin(8\pi\zeta)\,. \end{aligned} \tag{3.1.9}$$

where the coefficients $p_0, ...p_4, q_1, ...q_4$ are calculated from the GSFE curves using the MATLAB curve fitting tool [130]. The continuous GSFE curves are shown in Figure 3.1.1(a) and the corresponding coefficients are presented in Table 3.1.4.

The explicit Euler method is employed for the time integration in the TDGL equation. The order parameter at time $t_i + \Delta t$ is formulated explicitly based on its value at time t_i according to Equation 3.1.2. A recent PFDD work [148] found that the explicit Euler method requires the timestep size Δt to be small enough for numerical stability, so $\Delta t = 0.01$ is used in our work.

Figure 3.1.2(a) shows the 3D cuboidal periodic simulation cell. As part of the Fast Fourier transform method for calculating the strain energy density, periodic boundary conditions are employed. All order parameters $\zeta = 0$ (perfect direct lattice) at each grid point, except those that lie on the plane $z = N/2$ and between $x = N/4$ and $x = 3N/4$ (in the darker shaded area) where $\zeta = 1$ (perfect direct lattice translated by 1 Burgers vector) for all

Table 3.1.4: *Interplanar spacing, d, normalized in terms of the Burgers vector magnitude b and the calculated coefficients for the lattice energy periodic potential for the pyramidal-II (Equation 3.1.9) slip mode. All coefficients are shown in units of $mJ{\cdot}m^{-2}$.*

Material	d/b	p_0	p_1	p_2	p_3	p_4	q_1	q_2	q_3	q_4
Be	0.22619	989.73	−295.15	−572.54	−45.07	−41.44	−178.95	143.29	6.682	−15.83
Mg	0.22318	217.98	−75.35	−116.48	−6.137	−9.728	−55.26	15.05	8.900	−1.228
Y	0.22680	332.03	−154.61	−137.14	−24.28	−4.422	−76.47	22.48	10.91	−1.145
Ti	0.22589	427.52	−165.06	−220.30	−22.96	−9.542	−52.33	118.72	−13.57	−16.63
Zr	0.22466	366.91	−127.64	−196.37	−21.80	−8.282	−48.31	105.95	−12.50	−12.27
Hf	0.22601	528.33	−184.61	−258.63	−41.86	−18.95	−82.81	131.01	−11.56	−15.33
Re	0.22392	1205.08	−482.64	−551.80	−92.09	−1.064	−269.59	46.20	42.31	24.93
Co(NM)	0.22416	875.19	−404.22	−306.22	−74.51	−38.14	−239.18	93.18	40.97	−17.05
Co(FM)	0.22344	770.05	−318.55	−360.51	−33.14	−23.72	−220.16	48.84	16.88	4.346
Zn	0.20934	214.57	−74.43	−115.09	−5.264	−15.33	−49.90	−56.68	23.13	8.863
Cd	0.20848	109.91	−41.06	−57.01	−2.154	−8.134	−25.06	−35.13	13.93	4.391

grid points in this region. Since dislocations are not explicitly defined in the PFDD model, but rather are inferred as a structurally necessary defect along boundaries between regions with different order parameter integer values, two perfect dislocations are initialized in our simulation cell, one at $x = N/4$ and the other at $x = 3N/4$, forming a dipole. We chose this set up as opposed to initializing the order parameter step from $0 \rightarrow 1$ at $x = N/2$ to avoid placing an unintentional dislocation along the periodic boundary. Along each direction of the simulation cell there are $N = 640$ grid points. Several simulation cell sizes were tested, and this size was determined to be sufficiently large such that the final equilibrium state was unaffected by the image dislocations in the periodic cells.

The grid spacing in all x, y, and z directions, is set as the interpla-

nar distance d for the pyramidal-II plane normalized by the Burgers vector magnitude b. Note that b is for the $\langle 11\bar{2}3\rangle$ direction and d is for the $\{\bar{1}\bar{1}22\}$ plane. In the (hkl) Miller-Bravais notation, the interplanar spacing is $\frac{1}{d^2} = \frac{4}{3}\frac{h^2+hk+k^2}{a^2} + \frac{l^2}{c^2}$. Thus, the interplanar spacing accounts for the lattice spacing in both the $\langle a\rangle$ and $\langle c\rangle$ directions and changes with the material c/a ratio. By using the interplanar spacing as the grid spacing, the calculations account for the differences in the c-axis length among the HCP materials. Table 3.1.4 summarizes the normalized interplanar spacing d/b for each material. In addition, the DFT calculated elastic constants and lattice parameters, shown previously in Table 3.1.2, are used to inform the materials parameters for each simulation.

Each simulation begins with a perfect edge or screw dislocation dipole placed on the glide plane, as shown in Figure 3.1.2(a). The dipole consists of a pair of dislocations with equal and opposite sign, which produces a net zero Burgers circuit around the simulation cell. The lines of the pair lie at $N/4$ and $3N/4$ along the x-axis and the line sense is oriented parallel to the y-axis, which is the $[1\bar{1}00]$ direction, as shown in Figure 3.1.2(b). For the edge dislocation, the Burgers vector is oriented parallel to the x-axis ($[11\bar{2}3]$ direction) and for the screw dislocation, it lies parallel to the y-axis. It can be demonstrated that as the system relaxes to its equilibrium state, the two dislocations in the dipole behave independently and identically. Accordingly, we focus the analysis hereinafter on the positive dislocation, which is on the left in Figure 3.1.2(a).

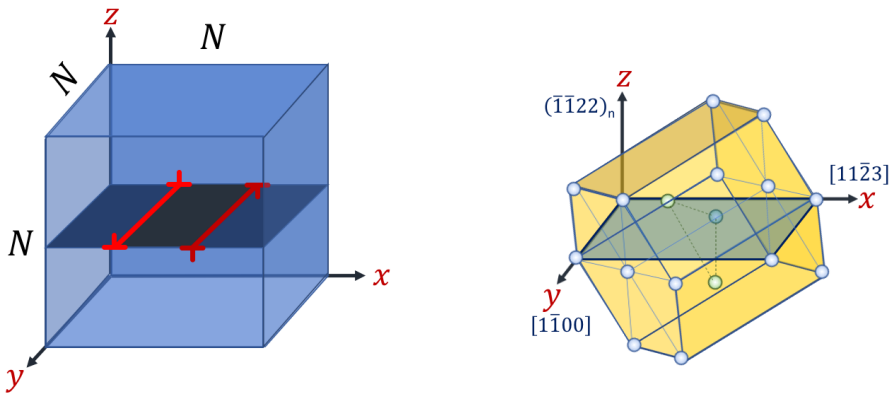

(a) **(b)**

Figure 3.1.2: *Schematics showing (a) the initial simulation set-up for the PFDD computational cell with two infinitely long parallel dislocations forming a dipole. In (b), the HCP unit cell is oriented (shown for an initial edge dislocation) such that the pyramidal-II glide plane lies parallel to the xy-plane in the simulation cell in (a). The simulation set-up for a screw dislocation would have the same initialization shown in (a), while the HCP unit cell in (b) would be rotated around the z-axis by* $90°$*. For clarity, the x-, y-, and z-axis in our simulation cell correspond to the x-, y-, and z-axis respectively in our HCP unit cell when initializing for an edge dislocation and to y-, x-, and z-axis respectively when initializing for a screw dislocation. Thus, the slip plane lies parallel to the simulation cell surface, the dislocation line sense lies parallel to the y-axis and the Burgers vector (and unit cell) orientation is reflective of the desired dislocation character.*

3.2 Results

3.2.1 Disregistry across the core structure

To determine the structure of the dislocation at all times during the relaxation process, we extract in-plane values of the order parameter, ζ, and compute the disregistry $b\zeta$ across the plane where the dislocation lies. Given that b is a constant for each metal, the latter quantity can be simplified as the order parameter density $\mathrm{d}\zeta/\mathrm{d}x$. Initially the full dislocation is compact and its $\mathrm{d}\zeta/\mathrm{d}x$ profile corresponds to a narrow peak at the initial position $x = 0$. If the dislocation dissociates during relaxation into smaller, distinct partial dislocations, the order parameter density profile would transform in time to one comprised of relatively shorter peaks where these partials are located, as illustrated in Figure 3.2.1. The viewing plane of this illustration lies transverse to the dislocation line. The two peaks correspond to the two partial dislocations on the glide plane and the locations of these peaks correspond to the positions of the center of the cores. To conserve the Burgers vector, the partials will have the same sign and thus repel one another, causing the left partial to displace to the left and the right one to the right from the dissociation site. If the cores of these partials were compact then they would appear as two narrow peaks. Yet, in actuality, the cores of the partials assume a finite width w in response to the energetic expense associated with creating a fault. Adopting the approach used commonly in analyses of diffraction data, we establish the widths of the partial cores, w_{l} and w_{r}, as the full width at half maximum (FWHM) of each peak in $\mathrm{d}\zeta/\mathrm{d}x$ profile. Over the years, the size of the extended dislocation cores have been most prominently characterized by the equilibrium distance between the two partials, which has also been variously called the equilibrium stacking fault width (SFW) or splitting

distance. Here, we define the equilibrium splitting distance as the distance between the centers of the two partial, denoted as R_{e}, as illustrated in Figure 3.2.1.

The Burgers vector decomposition between the two partials can also be determined from ζ and its density $\mathrm{d}\zeta/\mathrm{d}x$. The magnitude of the Burgers vectors for the partial dislocations can be expressed as a fraction of the magnitude of the full pyramidal-II Burgers vector. The magnitude of the Burgers vector of the left partial is related to the value of the order parameter $\zeta_0 = \zeta(x_0)$ where the position x_0 is the minimum value of the gradient within the stacking fault (i.e., between the two peaks). The magnitude of the Burgers vector for the right partial dislocation is the remainder $1 - \zeta_0$. Having identified ζ_0, we can calculate the Burgers vector of the two partials b_{l} and b_{r} via,

$$b = \zeta_0 b + (1 - \zeta_0) b = b_{\mathrm{l}} + b_{\mathrm{r}} \tag{3.2.1}$$

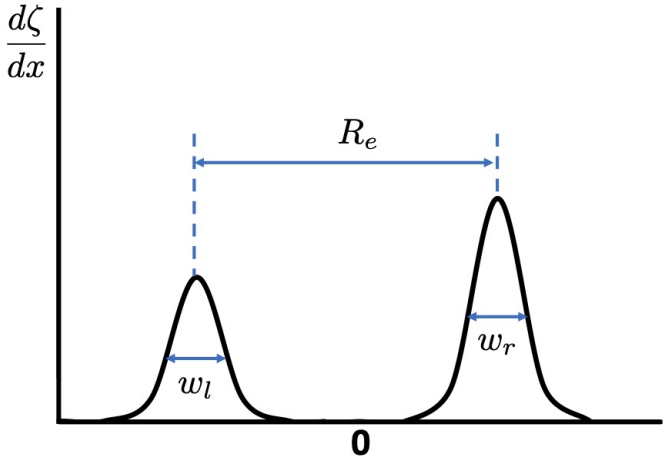

Figure 3.2.1: *A schematic of the gradient of the order parameter,* $\mathrm{d}\zeta/\mathrm{d}x$. *The labels indicate the equilibrium SFW,* R_{e}, *and their core widths,* w_{l} *and* w_{r}, *respectively.*

Table 3.2.1: *The equilibrium SFW, R_e, the left and right partial dislocation core widths, w_l and w_r, and left and right Burgers vector magnitude, b_l and b_r, respectively, for perfect edge and screw dislocation dissociation in ten HCP materials. Due to the grid spacing, the partial dislocation core widths have error bars of $\pm 0.1b$. Values of R_e, w_l, w_r, b_l, and b_r are normalized by b.*

Material	Dislocation	b (Å)	R_e	w_l	b_l	w_r	b_r
Be	Edge	4.228	4.298	0.45	0.48	0.45	0.52
	Screw	4.228	4.298	0.68	0.48	0.68	0.52
Mg	Edge	6.087	4.240	0.89	0.49	0.45	0.51
	Screw	6.087	2.901	0.89	0.46	0.47	0.51
Y	Edge	6.778	3.175	0.68	0.48	0.45	0.52
	Screw	6.778	2.495	0.91	0.46	0.45	0.54
Ti	Edge	5.468	4.065	0.45	0.44	0.45	0.56
	Screw	5.468	2.259	0.45	0.44	0.45	0.56
Zr	Edge	6.099	4.717	0.45	0.44	0.45	0.56
	Screw	6.099	2.696	0.45	0.44	0.45	0.56
Hf	Edge	5.966	4.971	0.45	0.44	0.68	0.56
	Screw	5.966	3.389	0.45	0.44	0.68	0.56
Re	Edge	5.262	5.599	1.79	0.46	0.67	0.54
	Screw	5.262	3.807	1.34	0.46	0.67	0.54
Co (FM)	Edge	4.746	4.916	1.79	0.47	0.89	0.53
	Screw	4.746	3.576	1.34	0.47	0.67	0.53
Zn	Edge	5.595	4.815	0.42	0.52	0.42	0.48
	Screw	5.595	4.397	0.42	0.52	0.42	0.48
Cd	Edge	6.410	4.168	0.42	0.53	0.42	0.47
	Screw	6.410	2.710	0.42	0.53	0.42	0.47

3.2.2 Be, Mg, Y

We begin with the group II and III HCP metals, Be, Y, and Mg. The GSFE curve of Be stands out from the others in Figure 3.1.1(a) with the largest unstable SFEs $U_{1,2}$, as well as a distinct local minimum at the stable energy I. In the GSFE curves for Y and Mg, however, the differences among $U_{1,2}$ and I are relatively small and hence, their local minima lie in a relatively shallow energy well.

Figure 3.2.2 shows the order parameter ζ and its density $\mathrm{d}\zeta/\mathrm{d}x$ after the equilibrium structure is achieved for dislocations in these metals. These profiles focus on a smaller region of the model crystal and ζ is represented by the dotted lines and $\mathrm{d}\zeta/\mathrm{d}x$ by the solid lines. The initial position of the dislocation before the dissociation process is zero (as indicated with vertical dashed line). In all three metals, the dislocation was observed to dissociate into two partials with a stacking fault in between. The partial dislocations appear as the two broad peaks in the order parameter density and the stacking fault is the intervening, nearly flat region between them.

Table 3.2.1 summarizes the Burgers vectors of their partials as well as their splitting distances R_{e}. The Burgers vectors in each partial dislocation are nearly, but not exactly, equal in value, with the left one being slightly smaller than the right one. For Be, Mg, and Y, their final splitting distances are, respectively, 18.17 Å, 25.81 Å, and 21.52 Å for the edge dislocations and 18.17 Å, 17.66 Å, and 16.91 Å for the screw dislocations. The edge dislocations have larger R_{e} than the screw dislocations. This trend only confirms the stronger edge repulsion force generated between two like edge dislocations than two like screw dislocations.

For validation, we turn to available DFT calculations, which only exist for Mg. DFT calculations reported 16.6 Å and 18.3 Å respectively for screw

and edge dislocations [137] and 14 Å for the screw dislocation [69]. MS simulations calculated 15 Å and 20.72 Å respectively for screw and edge dislocations [149] and 22.6 Å for the edge dislocation [15]. Differences are small considering likely variations in the definition of R_e, elastic constants, and fault energies among these studies. Further, as noted earlier, without the gradient term, partial core widths tend to be narrower than those from DFT or MS [94].

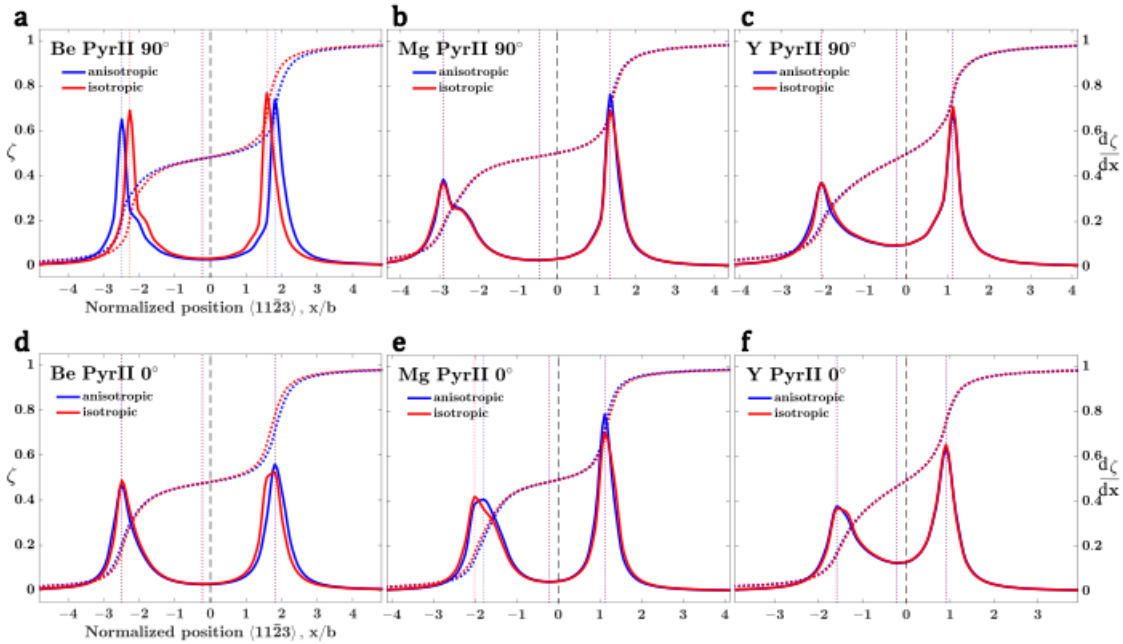

Figure 3.2.2: *The order parameter, ζ (dotted lines), and its density, $\mathrm{d}\zeta/\mathrm{d}x$ (solid lines), along the $[11\bar{2}3]$ slip direction for an initialized edge (a,b,c) and screw (d,e,f) dislocations in Be, Mg, and Y. Both isotropic (red) and anisotropic (blue) elastic considerations are compared. The vertical lines represent the location of the two partials before the dissociation, when they are one unstable perfect dislocation at zero position, and at the end of the simulation, when equilibrium is achieved.*

The estimates for the widths of the partial cores w for Be, Y, and Mg are

listed in Table 3.2.1. The energetic formulation in the model expects that the larger $U_{1,2}$ would lead to the narrower w. As expected, we observe that the cores of the partials are generally wider in dislocations of Mg and Y, with the smaller peak energies than those of Be, which has the highest U_1 and U_2 of this group.

We see that, in Mg and Y, the dislocation structures are asymmetric with the width w_l of the left partial generally larger than w_r for the right one. The asymmetry can be quantified by the ratio of $w_\mathrm{l}/w_\mathrm{r}$, which is also given in Table 3.3.1. In the case of the edge dislocation, in Mg, the asymmetry is noticeable with $w_\mathrm{l}/w_\mathrm{r}$ slightly less than 2.0, and less so in Y with $w_\mathrm{l}/w_\mathrm{r} = 1.5$. These differences result primarily from the different energetic pathways on the GSFE curve corresponding to their displacement. The energetic path for the left partial as it displaces in the negative $\langle 11\bar{2}3\rangle$ direction follows the right-hand portion of the GSFE and is affected by the second peak U_2. This path is different from that taken by the right partial, which displaces in the positive $\langle 11\bar{2}3\rangle$ direction and is, hence, dictated by U_1.

We performed a second set of calculations considering isotropic elasticity in place of the more realistic anisotropic elasticity. The split distances R_e and asymmetries between the two partials are not noticeably affected by elastic anisotropy. Exceptions are a slight decrease in R_e for the edge dislocation in Be from 18.17 Å to 16.26 Å and a slight increase for the screw dislocation in Mg from 17.66 Å to 19.02 Å when isotropy is assumed.

3.2.3 Ti, Zr, Hf

In this section, the equilibrium structures of dislocations for group IV HCP metals (Ti, Zr, and Hf), are examined. The GSFE curves for this group have similar shapes with a distinct local minimum located at $x_I/b = 0.43$–0.44,

which deviates significantly from the ideal 0.5. In each case, the two local maxima, U_1 and U_2, are not significantly different in value.

Figure 3.2.3 presents ζ and $\mathrm{d}\zeta/\mathrm{d}x$ for screw and edge dislocations in these metals after equilibrium is achieved. Like the previous metals, the dislocations in this group do not maintain a compact core. They dissociate into two distinct partials, which for all three metals, are unequal in value, with the left one being noticeably smaller, by 18%, than the right one. This uneven split is an outcome of the relatively short critical shear displacement of $0.43b$–$0.44b$ needed to achieve the local minimum fault in all their GSFE curves. The separation distances R_e of these partials belonging to the edge dislocations are 28.77 Å, 22.23 Å, and 29.66 Å for Zr, Ti, and Hf, respectively. Compared to the edge dislocations, in all metals in this group, R_e for screw dislocations are smaller, 16.44 Å, 12.35 Å, and 20.22 Å, for Zr, Ti, and Hf, respectively.

Table 3.2.1 lists the partial widths, w, as defined by the FWHM method in the two peaks in ζ. Two of the metals, Zr and Ti, feature a symmetric core structure with $w_\mathrm{l}/w_\mathrm{r} = 1.0$. Hf, on the other hand, exhibits an asymmetric core, unlike Zr and Ti, with $w_\mathrm{l}/w_\mathrm{r} = 0.66$.

The same calculations under the assumption of elastic isotropy are also shown in the same plots for comparison. Elastic anisotropy of Ti and Zr leads to wider R_e than when the anisotropy is removed. The edge dislocation in Ti exhibits the greatest increase in R_e from 17.29 Å (isotropic) to 22.23 Å (anisotropic). For Hf, on the other hand, elastic anisotropy does not lead to significant changes in R_e or its asymmetric structure.

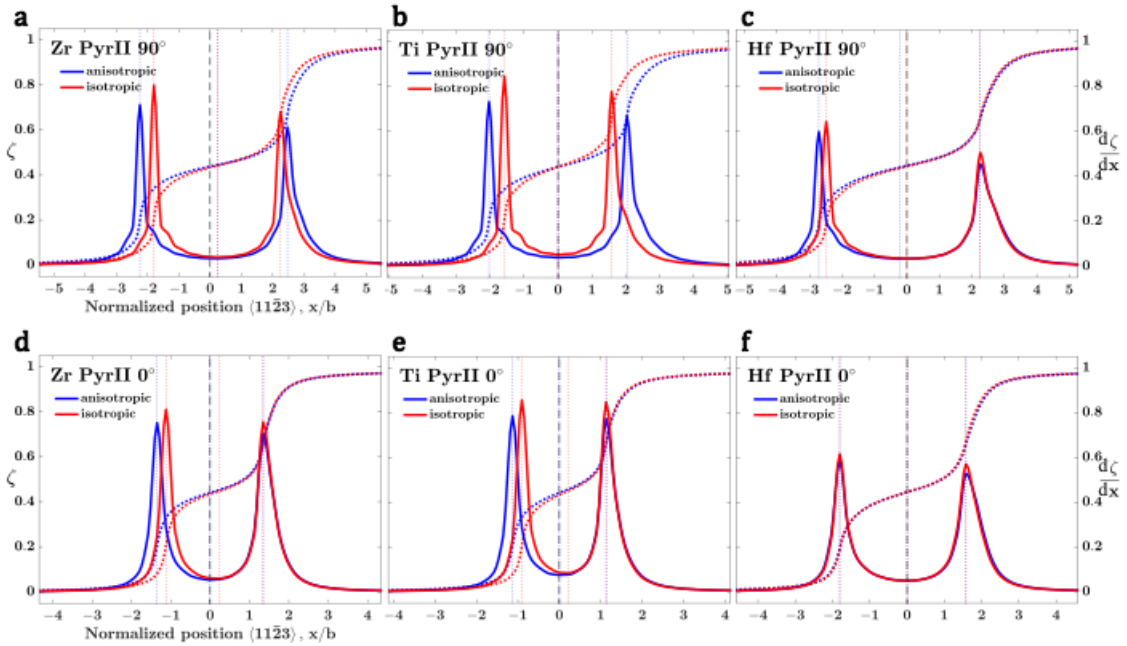

Figure 3.2.3: *The order parameter, ζ (dotted lines), and its density, $/dx$ (solid lines), along the* $[11\bar{2}3]$ *slip direction for an initialized edge and screw dislocation in Ti, Zr, and Hf. The coloring follows Figure 3.2.2.*

3.2.4 Re and Co

Next, we study the equilibrium core structures of dislocations in the group VII and IX HCP metals: Re and Co. Their GSFE curves are compared to others previously in Figure 3.1.1(a). An important distinguishing feature of their energetic landscapes from the other eight metals is their significant differences between their two peak energies U_1 and U_2. U_2 is 30% higher than U_1 in Re and 36% higher than U_1 in Co.

Figure 3.2.4 presents their equilibrium dislocation structures. These two metals share many common features with the most prominent one being their asymmetric structure, compared to the dislocation structures of other metals. They both dissociate into two partials that are unequal in Burgers vector value and core width. The Burgers vector left partial is approximately

15% smaller in length than that of the right one and its width is twice as large. The widths of the partial cores are some of the largest compared to the other metals, even though their lattice parameters are not. Re has the larger R_e of 29.46 Å and 20.03 Å for the edge and screw dislocations, respectively. Co has smaller R_e of 23.33 Å and 16.97 Å for the two dislocations, respectively.

For comparison, the calculated structures using their isotropic equivalent elastic properties are also included in these profiles. Elastic anisotropy has a negligible effect on the splitting distance of both the edge and screw dislocations. Only a very slight increase is seen in the R_e for the screw dislocation in Co due to elastic anisotropy; $R_e = 15.91$ Å for isotropy compared to 16.97 Å for anisotropy.

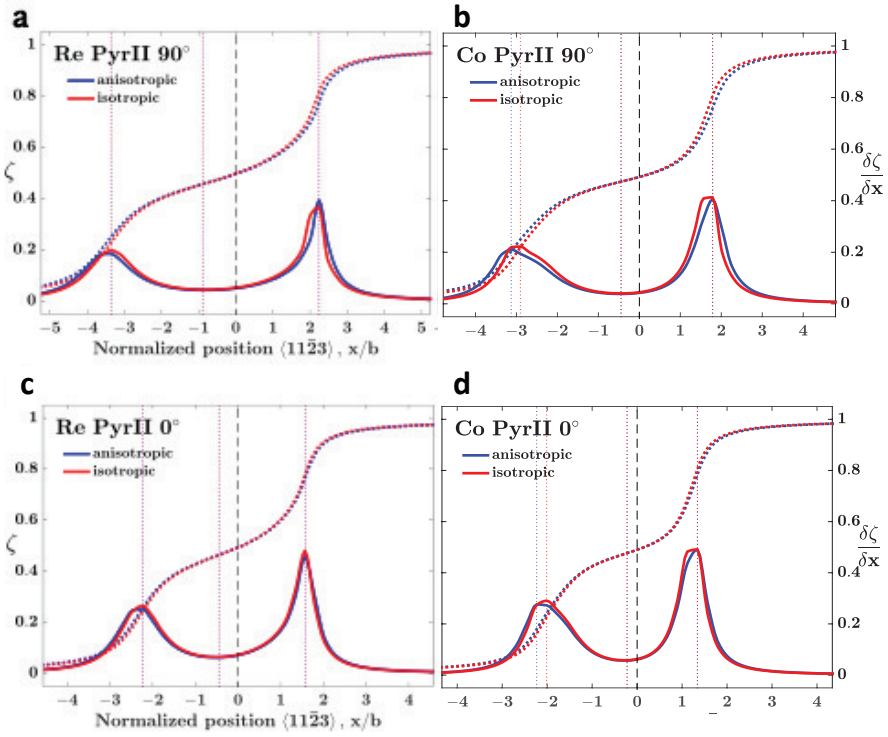

Figure 3.2.4: *The order parameter, ζ (dotted lines), and its density, $\mathrm{d}\zeta/\mathrm{d}x$ (solid lines), along the $[11\bar{2}3]$ slip direction for an initialized edge and screw dislocation in Re and Co (FM). The coloring follows Figure 3.2.2.*

3.2.5 Zn and Cd

The last two metals studied are Zn and Cd, which are group XII metals. The GSFE curves for these materials are presented previously in Figure 3.1.1(a). Compared to the other metals, they have the lowest unstable SFEs U_1 and U_2. Also, unique to this group, their c/a ratios are larger than the ideal value and the displacement x_I/b at which the local minimum is achieved is greater than 0.5 (located at 0.52–0.53). The displacements corresponding to the unstable SFEs are also larger than those of the other metals.

Figures 3.2.5 shows the calculated ζ and $\mathrm{d}\zeta/\mathrm{d}x$ profiles for the equilibrium cores for the edge and screw dislocations in Zn and Cd. Their splitting distances, R_e, are 26.94 Å and 24.60 Å for the edge and screw dislocations for Zn and 26.73 Å and 17.37 Å for Cd.

The dislocation structures of these two metals is nearly symmetric. The widths of their two partials are nearly equal. Although, like the other metals, the Burgers vectors of the two partials are not precisely equal in length; however, the difference is not significant (within ±0.02 Å). Due to the larger displacement offset of the local minimum in their GSFE curves, the value of the Burgers vector of the left partial is slightly larger than the right one.

Figures 3.2.5 (a)–(d) shows that anisotropy has a significant effect on the equilibrium splitting distances for both Zn and Cd. These group XII elements are the only materials here to exhibit a much narrower $\mathrm{d}\zeta/\mathrm{d}x$ peak separation distance when anisotropy is taken into consideration. In Zn, for the edge dislocation, R_e reduces to 26.94 Å under elastically anisotropic conditions from an isotropic one of 42.17 Å; for the screw dislocation, R_e reduces to 24.60 Å under elastically anisotropic properties from R_e of 30.45 Å under isotropic ones. Cd shows a similar trend, with R_e value of 26.73 Å and 37.42 Å for the edge dislocation with elastic anisotropy and isotropic

isotropy, respectively. Finally, in the screw case in Cd, we see R_e equals 17.37 Å and 22.72 Å for the elastic anisotropic and isotropic cases, respectively.

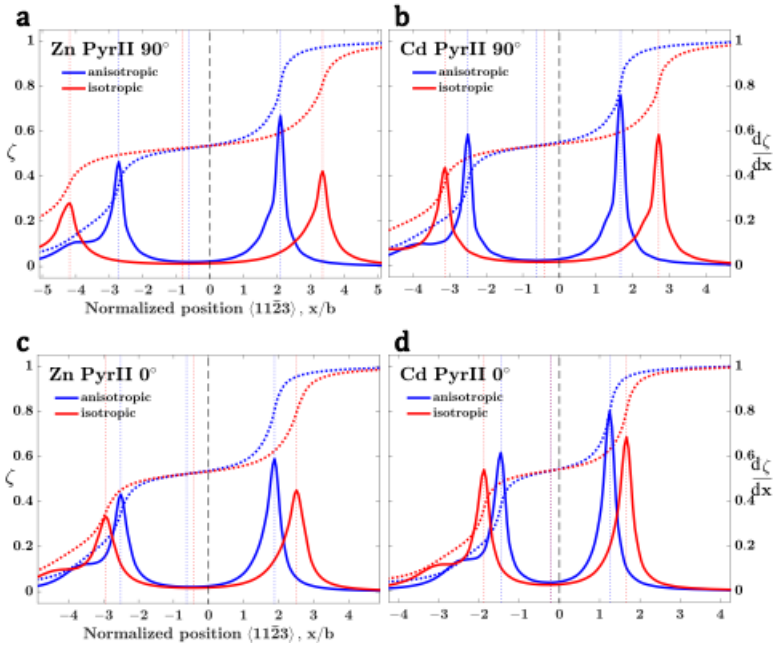

Figure 3.2.5: *The order parameter, ζ (dotted lines), and its density, $\mathrm{d}\zeta/\mathrm{d}x$ (solid lines), along the* $[11\bar{2}3]$ *slip direction for initial edge and screw dislocations in Zn and Cd. The coloring follows Figure 3.2.2.*

3.3 Discussion

From the DFT calculations, we find that these metals bear different levels of elastic anisotropy and different maxima and minima in their GSFE curves. In PFDD calculations, these properties are directly taken into account, and as the results have shown, the dissociation process leads to dislocation cores that deviate from the ideal picture, particularly showing partial dislocations with non-compact cores and that are unequal in their widths and Burgers vectors. With all ten HCP metals in hand, we identify in the next few sections

the material properties that govern their core structure.

3.3.1 Scaling of core size with the intrinsic stacking fault energy

The analytical model in Eq. 1.4.2 expects that the intrinsic SFE, I, has the most pronounced effect on the R_e/b. Figure 3.3.1 presents the variation in the PFDD calculated distances when considering anisotropy, R_e/b, with $I/(Kb)$, as expected from the analytical model in Eq. 1.4.2. R_e/b shows a strong inverse scaling with $I/(Kb)$. Metals Ti and Y have the largest $I/(Kb)$ and also the narrowest $R_e/b \approx 2$–3, while Zn and Be with the smallest $I/(Kb)$ have the widest $R_e/b \approx 5$–6. The inverse scaling reflects the same basic principle used in the analytical model, that an SFW a low I comprises a large fraction of the entire core structure and I has a dominant effect on the equilibrium split distance.

Figure 3.3.1(b) examines the relationship between R_e and the higher maxima U_2 in the GSFE curve. A remarkably strong inverse scaling in $U_2/(Kb)$ emerges. A similar analysis with $U_1/(Kb)$ does not show a strong trend, and can be found in Figure 3.C.1 in Appendix C. In the dissociation process, the partial dislocations move apart and evidently it is the higher maximum U_2 that affects the resistance.

To date, the analytical model in Eq. 1.4.2 was the only application used to predict R_e/b for the pyramidal-II dislocations for just some of the HCP metals studied here. For the remaining materials, this work is the first to quantify the equilibrium stacking fault width on the pyramidal-II plane. Results indicate that as expected from theory, R_e/b scales inversely with $I/(Kb)$ and is minimally impacted by $U_1/(Kb)$ and $U_2/(Kb)$. The key difference is

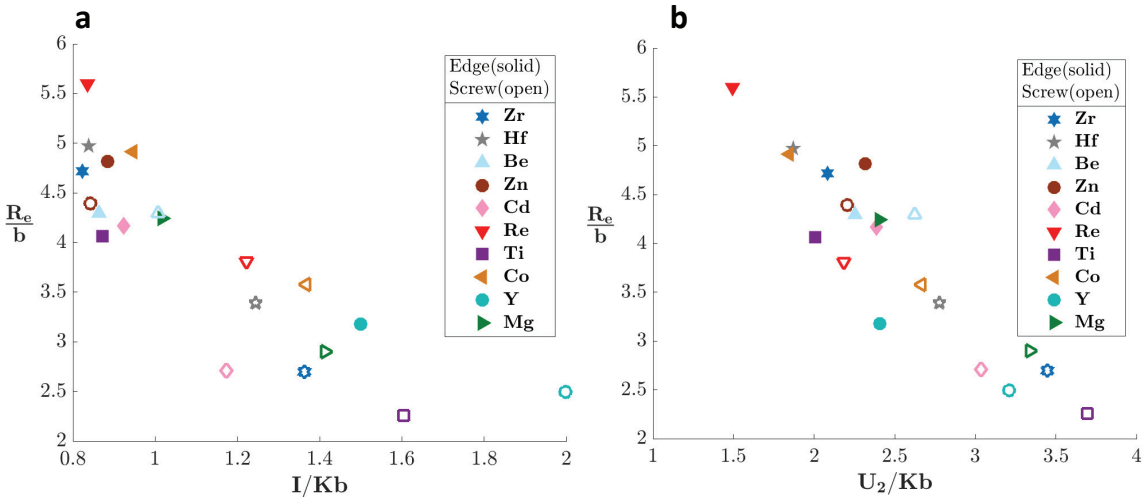

Figure 3.3.1: *The equilibrium partial separation distance R_e, calculated using PFDD plotted against (a) the intrinsic SFE I normalized by Kb, and (b) the unstable SFE U_2, also normalized by Kb. Expressions for K are given in Ref. [4].*

that the scaling is not as strong as the analytical model predicts and is not profoundly affected by the anisotropy in its elasticity properties inherent to HCP metals.

3.3.2 Origin of the asymmetric cores

The analysis so far has indicated that the asymmetry in the dislocation structures is not a consequence of elastic anisotropy. The dislocation cores from the anisotropic and isotropic equivalent calculations exhibit very similar, if not the same, asymmetries. The properties of the GSFE curves of the individual metals, on the other hand, are highly influential. In particular, the core widths of the partials are affected by the depth of the local minimum in the GSFE. Shallow energy wells, for instance, would suggest that a broad partial core, in which the partial Burgers vector is distributed in plane, are

more energetically favorable over the formation of the compact partial core bordering a minimum energy intrinsic stacking fault.

Here we observe that the GSFE curves of all ten HCP metals exhibit some degree of asymmetry about the local minimum state. The two local maxima, U_1 and U_2, are unequal, and hence, the local minimum lies at different depths with respect to U_1 and U_2. The left partial, as it displaces left in the negative slip direction, is affected by D_2, and the right one, as it displaces in the positive slip direction, by D_1. With depth quantified by $D = (U - I)/U$, their differences can be measured by comparing $D_1 = (U_1 - I)/U_1$ and $D_2 = (U_2 - I)/U_2$ in each GSFE curve. Table 3.3.1 summarizes the ratios U_2/U_1 and D_2/D_1 for each metal. A correlation can be identified by comparing D_2/D_1 with $w_\mathrm{l}/w_\mathrm{r}$. The more symmetric core widths have nearly equal depths within 20%. Those metals with GSFE curves with greater differences, where D_2/D_1 is large, such as Mg, Y, and Re, have highly asymmetric cores.

3.3.3 Effect of elastic anisotropy

The equilibrium core structures calculated assuming effective isotropic or actual anisotropic elastic properties are similar in many features. For instance, many of the asymmetric properties of the core are retained even when the anisotropy is removed by using the effective isotropic constants. The primary effect of anisotropy is to, in some cases, either narrow or widen the equilibrium split distance, R_e (see Figure 3.3.2). Qualitatively, these effects only confirm that the dominant contribution of elasticity is to control the elastic repulsive interactions between the two partials.

In theory, the ratio of the anisotropic to isotropic $R_\mathrm{e}^\mathrm{ani}/R_\mathrm{e}^\mathrm{iso}$ should scale with the ratio of the pre-energy factors, K/μ from Equation 1.4.2, the analytical calculation for the stacking fault widths. Figure 3.3.3(a) shows the

Table 3.3.1: *The ratio between the left and right partial dislocation cores, $w_\mathrm{l}/w_\mathrm{r}$, for both edge and screw dislocations, and the ratio between the unstable SFEs, U_2/U_1, and the ratio, D_2/D_1. Values of w_l and w_r are from Table 3.2.1.*

Material	$w_\mathrm{l}/w_\mathrm{r}$ (edge)	$w_\mathrm{l}/w_\mathrm{r}$ (screw)	U_2/U_1	D_2/D_1
Be	1.0	1.0	1.324	1.252
Mg	1.98	1.89	1.512	1.600
Y	1.5	2.02	1.488	5.156
Ti	1.0	1.0	1.237	1.223
Zr	1.0	1.0	1.222	1.170
Hf	0.66	0.66	1.259	1.267
Re	2.67	2.0	1.423	2.157
Co (FM)	2.0	2.0	1.553	2.390
Zn	1.0	1.0	1.213	1.151
Cd	1.0	1.0	1.160	1.112

variation in the ratio of $R^{\mathrm{ani}}/R^{\mathrm{iso}}$, determined using PFDD, with the calculated pre-energy factor K/μ for both edge and screw dislocations. The calculations follow the expected scaling although we see that cases in which the anisotropic and isotropic separations were nearly equivalent corresponding to a range of $K/\mu = 1.05$–1.2. Yet still, we find that in most cases that the anisotropic R_e is wider than the isotropic one when K/μ is much greater than unity and vice versa when it is much less than unity.

Over the years, many factors have been proposed to quantify the level of elastic anisotropy in HCP metals, some of which we have included in Ap-

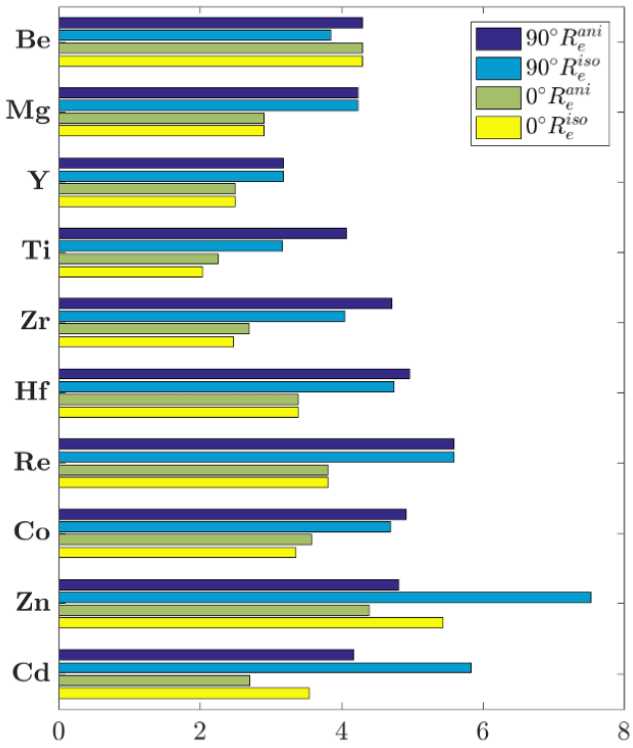

Figure 3.3.2: *PFDD calculated SFWs (R_e) for edge (90 °) and screw (0 °) dissociated dislocations in the 10 HCP materials with assumed elastic isotropy (iso) and anisotropy (ani). Mg, Y, and Re are relatively isotropic. Metals with higher levels of anisotropy have wider R_e except for Zn and Cd, which are narrower. Anisotropy does not change morphology of the dislocation core.*

pendix D for completeness. Knowing which anisotropic indexes best capture certain material behavior could be important to larger length scale models, which cannot model discrete deformation behaviors. There have been many different anisotropic indexes (see Table 3.D.1 for the calculations of α, β, and γ, as well as, Figure 3.D.1 depicting their relationship, if any, to the ratio $R^{\text{ani}}/R^{\text{iso}}$ for edge and screw dislocations) that do not consistently describe the impact elastic anisotropy can have on the equilibrium stacking fault width.

Recently, however, a measure of the distance between the upper and lower bounds of the fourth-ranked elasticity tensor was used to develop an index A^L, applicable to all classes of elastic anisotropy [150]. Here we apply A^L to quantify the level of anisotropy among the ten HCP materials. A^L is defined as:

$$A^L = \sqrt{\left[\ln\left(\frac{\kappa^{\mathrm{V}}}{\kappa^{\mathrm{R}}}\right)\right]^2 + 5\left[\ln\left(\frac{\mu^{\mathrm{V}}}{\mu^{\mathrm{R}}}\right)\right]^2} \tag{3.3.1}$$

where the bulk (κ^{V}, κ^{R}) and shear moduli (μ^{V}, μ^{R}) are calculated following the Voigt and Reuss averages, respectively. By definition, for an ideally isotropic material, $A^L = 0$.

Table 3.3.2 shows the A^L factors, as well as the other indicators, for all metals here. According to A^L, Y is the most isotopic HCP metal and Zn the most anisotropic. Figure 3.3.3 plots the ratio of the anisotropic to isotropic R_{e} against A^L. The effect of anisotropy on the deviations is greater in the edge case than screw case. It can be anticipated that the edge dislocations would be more sensitive to the level of anisotropy due to the more complex elastic stress state generated by edge dislocations than screw dislocations.

Significantly, Figure 3.3.3(b) shows that the closer $R_{\mathrm{e}}^{\mathrm{ani}}/R_{\mathrm{e}}^{\mathrm{iso}}$ is to unity, the smaller the value of A^L, and vice versa. For instance, metals like Y, Re, and Mg, with the relatively lower values of A^L, have R_{e} values that are unchanged when isotropy is assumed in place of their actual anisotropy. It captures the fact that, while Mg may be nearly isotropic, it is not exactly isotropic, explaining the slight deviation of $R_{\mathrm{e}}^{\mathrm{ani}}/R_{\mathrm{e}}^{\mathrm{iso}}$ of the screw dislocation from unity. As A^L for the metal increases up to 0.2 $R_{\mathrm{e}}^{\mathrm{ani}}$ becomes increasingly greater than $R_{\mathrm{e}}^{\mathrm{iso}}$. Likewise, the $R_{\mathrm{e}}^{\mathrm{ani}}$ of Cd and Zn, which have the highest A^L (¿ 0.3), deviate the most from their isotropic $R_{\mathrm{e}}^{\mathrm{iso}}$ counterpart, although the effect is to shrink $R_{\mathrm{e}}^{\mathrm{ani}}$ with respect to $R_{\mathrm{e}}^{\mathrm{iso}}$.

The value for the pre-energy factor K/μ in Fig. 9(a), does not adequately reflect the variation of $R^{\text{ani}}/R^{\text{iso}}$. We find in Fig. 9(b) that the closer A^L is to zero, the closer the ratio $R^{\text{ani}}/R^{\text{iso}}$ unity, and vice versa, the higher the value of A^L, the greater the ratio $R^{\text{ani}}/R^{\text{iso}}$ diverges from unity. In this regard, the K/μ pre-factor does not work as well as A^L.

Table 3.3.2: *Log-Euclidean anisotropy index, A^L, calculated using Equation 3.3.1 and the bulk (κ^{V}, κ^{R}) and shear moduli (μ^{V}, μ^{R}) as defined by Voigt and Reuss are calculated for the ten HCP materials. All values are determined using DFT calculated elastic constants shown in Table 3.1.2.*

Material	A^L	κ^{V}	κ^{R}	μ^{V}	μ^{R}
Be	0.033	123.28	122.69	154.35	152.13
Mg	0.018	36.37	36.35	19.26	19.10
Y	0.005	40.01	40.01	25.65	25.58
Ti	0.173	118.21	118.17	35.67	33.01
Zr	0.092	97.74	97.36	30.23	29.01
Hf	0.021	114.34	114.26	54.05	53.55
Re	0.028	378.89	378.86	177.61	175.42
Co (FM)	0.075	210.18	210.16	106.11	102.61
Zn	0.509	71.43	60.11	39.58	31.95
Cd	0.341	46.64	42.01	12.51	10.82

The correlation is a significant result in light of the fact that three common indices are poor indicators of the degree of aniostropy. In Figure 3.D.1(a), shown in Appendix D, we plot the $R_{\text{e}}^{\text{ani}}/R_{\text{e}}^{\text{iso}}$ versus the other anisotropic indicator α (Eq. 3.D.1). This factor is defined by only four of the five constants.

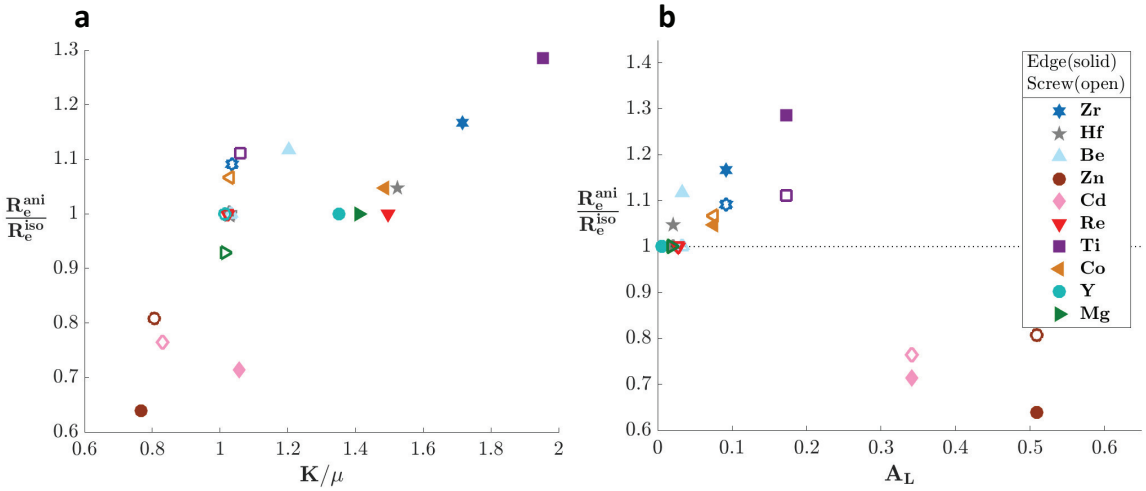

Figure 3.3.3: *The ratio of the anisotropic to the isotropic equilibrium SFW R_e^{ani}/R_e^{iso} plotted against (a) the anisotropic energy factor, K normalized by the shear modulus, μ, and (b) the Logarithmic Euclidean anisotropy index, A^L, for both edge and screw dislocation dissociation.*

Similar to A^L, for both the edge and screw character dislocations, larger α corresponds to higher deviations from ideally isotropic. Mg, Y, and Re present the lowest degree of anisotropy with the α indicator, and Zn and Cd, show the highest deviation from isotropy. However, Be has a negative value for this indicator and is an outlier. We also test, in Appendix D, the performances of the other anisotropic indicators β (Eq. 3.D.2) and γ (Eq. 3.D.3), as shown in Figure 3.D.1(b,c). As shown, the differences in the anisotropic and isotropic R_e exhibit no correlation with these other HCP anisotropy indicators for either the edge or screw-character dislocations. At least for dislocations, these anisotropy indicators do not gauge well the anisotropic effects on R_e.

3.4 Conclusions

In this work, we use phase-field dislocation dynamics (PFDD) to calculate the size and structural properties of pyramidal-II $\langle c+a \rangle$ dislocations in ten HCP metals: Be, Cd, Co, Hf, Mg, Re, Ti, Y, Zn, and Zr. These metals vary widely in their c/a ratio and degree of elastic anisotropy. As part of the formulation, the calculation incorporates generalized stacking fault energie (GSFE) curves for the pyramidal-II plane calculated from density functional theory (DFT). Among these metals, the GSFE curves are similar in shape but vary significantly in the location and value of their two local maxima and local minimum I. In addition, for Co, magnetism is shown to play a vital role in achieving a local minimum energy in its GSFE. With DFT informed PFDD simulations of the dissociation process of both perfect screw and edge dislocations to their low energy, equilibrium structures are obtained. For all metals, the equilibrium dislocation structures of both edge and screw character are not compact, but extended bounded by two partial dislocations. Their splitting distances, R_{e}, are found to range from 1.2–3 nm. We show that R_{e}/b scales inversely with the local minimum $I/(\mu b)$. For some metals, the structures are asymmetric, wherein the core widths of the two partial dislocations are not exactly equal, deviating from the classic picture from dislocation theory. The asymmetries in these cases can be explained by significantly unequal maxima in the GSFE curves. The elastic anisotropy is shown to not affect asymmetry between the partial Burgers vectors or core widths. We show that the stronger the degree of elastic anisotropy, as measured by the A^L factor, the stronger the effect on R_{e}. The influence, whether widening or narrowing the core relative to isotropy, depends on the degree of anisotropy and the screw/edge character of the dislocation.

3.5 Copyright

This chapter was reworked from our published research in the Physical Materials Review Journal [2].

Appendix

3.A GSFE surface

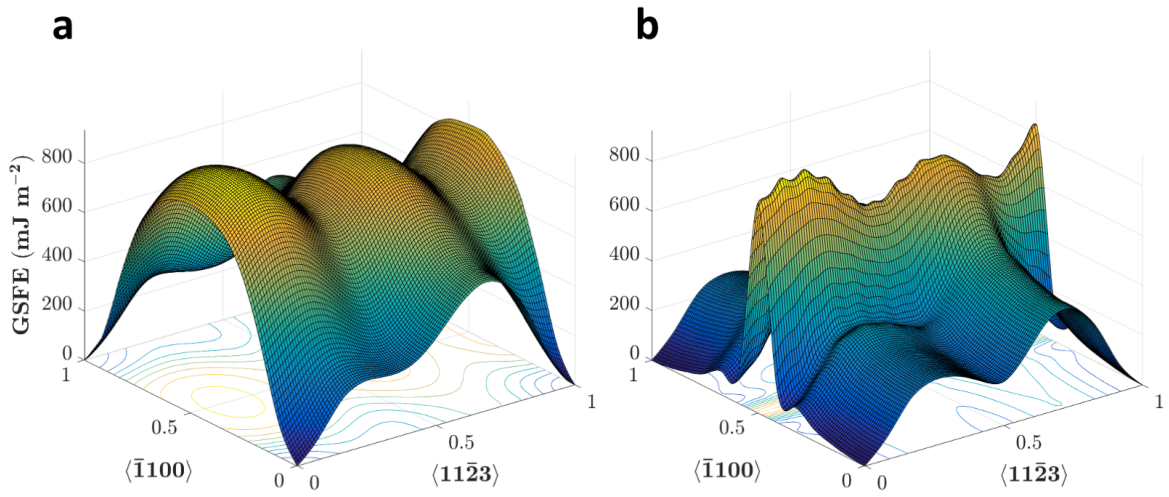

Figure 3.A.1: *The standard (a) and relaxed (b) GSFE surfaces for the pyramidal-II plane in Mg. The x-axis and y-axis values are normalized by the magnitude of a direct lattice translation vector along the* $\langle11\bar{2}3\rangle$ *and* $\langle\bar{1}100\rangle$ *directions, respectively.*

Figure 3.A.1 shows 2D GSFE surfaces for the pyramidal-II plane in Mg

calculated with standard and x-Relaxed methods for determining GSFEs [15, 78] using DFT. In the standard method, we shift the upper half of the crystal with respect to the lower half of the crystal on the pyramidal-II plane in small displacements and only allow atomic positions along the z-direction to relax. In the x-Relaxed method, we also allow for an additional relaxation along the $\langle \bar{1}100 \rangle$ direction. Additional relaxation normal to $\langle 11\bar{2}3 \rangle$ allows for local rearrangement of the atoms near the glide plane, which leads to a well-defined local minimum compared to a shallow minimum for the standard (unrelaxed) GSFE surface [78].

The lowest energetic path on the pyramidal-II GSFE surfaces, obtained using both the standard (Figure 3.A.1(a)) and x-Relaxed (Figure 3.A.1(b)) methods, lies along the $\langle c+a \rangle$ edge, collinear to the $\langle 11\bar{2}3 \rangle$ direction, energetically indicating that the partials will have only parallel components. This is similar to a recent finding that the $\langle 111 \rangle$ GSFE curves on $\{110\}$, $\{112\}$, and $\{123\}$ planes in BCC metals lie along local minimum lines on respective GSFE surfaces [6]. This allows us to simplify the input for the periodic potential ϕ, used in the E^{lattice} calculation, Equation 10, of the PFDD model, from the GSFE surface to the GSFE curve, that describes the governing energetics for the pyramidal-II plane. For this reason, we justify calculating only the GSFE curves for the remaining HCP materials, which would otherwise be too computationally time consuming when using DFT to calculate the full GSFE surface. The full GSFE surface could be calculated with MS, however this method is dependent on interatomic potentials and could impact the position of the minima, and thus impact the PFDD results.

3.B Experimental elastic constants

Table 3.B.1: *Experimentally determined elastic constants (in GPa) for the ten HCP metals [7] for comparison with the DFT derived values in Table 3.1.2.*

Material	C_{11}	C_{12}	C_{13}	C_{33}	C_{44}
Be	299.40	27.60	11.00	342.20	166.20
Mg	63.48	25.94	21.70	66.45	18.47
Y	83.40	29.10	19.00	80.10	26.90
Ti	176.10	86.90	68.30	190.50	50.80
Zr	155.40	67.20	64.60	172.50	36.30
Hf	190.10	74.50	65.50	204.40	60.00
Re	634.40	266.00	202.00	701.60	169.10
Co (FM)	319.50	166.10	102.00	373.60	82.40
Zn	179.09	37.50	55.40	68.80	45.95
Cd	129.23	39.99	40.95	56.68	24.20

3.C Variation of R_e with the lower unstable stacking fault energy

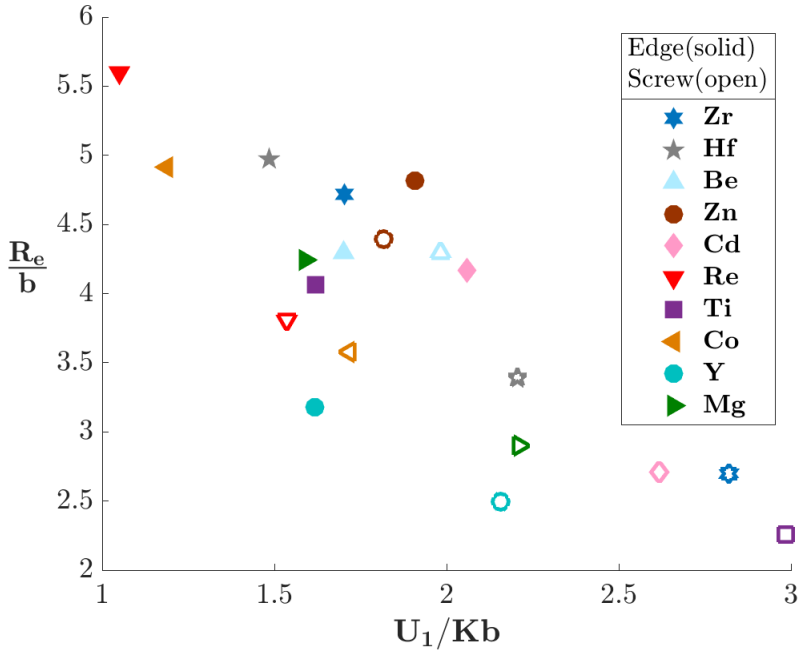

Figure 3.C.1: *The equilibrium SFW R_e plotted against the unstable SFE, U_1, normalized by the anisotropic energy factor, K, and the Burgers vector, b.*

3.D Additional measures of elastic anisotropy

Here we present results for the measures of elastic anisotropy in HCP materials conventionally referred to as α, β, and γ, and are related to the elastic constants by [151]

$$\alpha = \frac{C_{11} + C_{12} - C_{33}}{C_{13}} \tag{3.D.1}$$

$$\beta = \frac{C_{66}}{C_{44}} \tag{3.D.2}$$

$$\gamma = \frac{1}{2C_{44}}\left[\frac{C_{33} + C_{11} + C_{12}}{2} - \frac{C_{13}\sqrt{\alpha^2 + 8}}{2}\right] \tag{3.D.3}$$

We note that only the last anisotropy factor, γ, contains all five independent elastic constants of an HCP metal.

Table 3.D.1: *Traditionally used anisotropic indices α, β, and γ, calculated in Equations 3.D.1–3.D.3. All values are determined using DFT calculated elastic constants shown in Table 3.1.2.*

Material	α	β	γ
Be	−3.232	0.806	1.008
Mg	1.130	1.039	1.272
Y	0.953	0.984	1.120
Ti	0.913	0.670	1.401
Zr	0.697	1.050	1.681
Hf	0.833	0.952	1.230
Re	0.944	1.018	1.332
Co (FM)	1.076	1.044	1.610
Zn	2.661	1.908	0.564
Cd	2.150	2.218	1.390

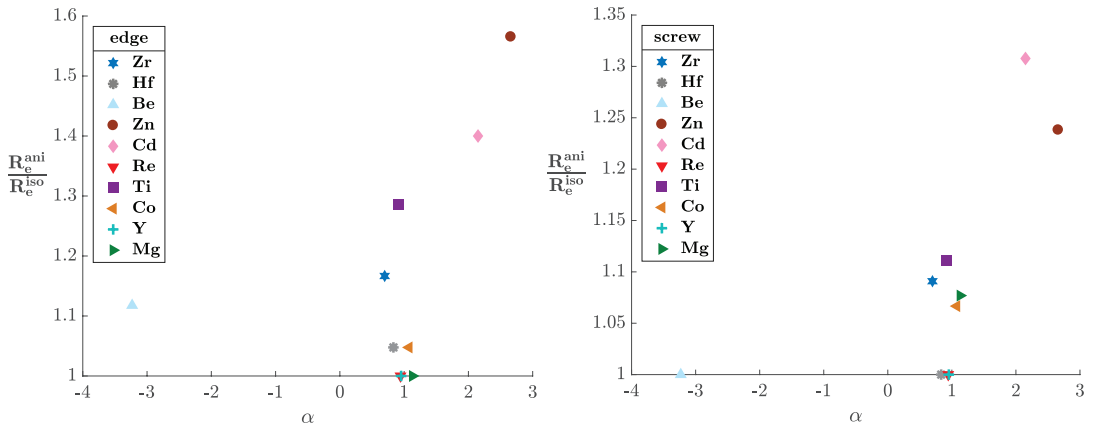

(a)

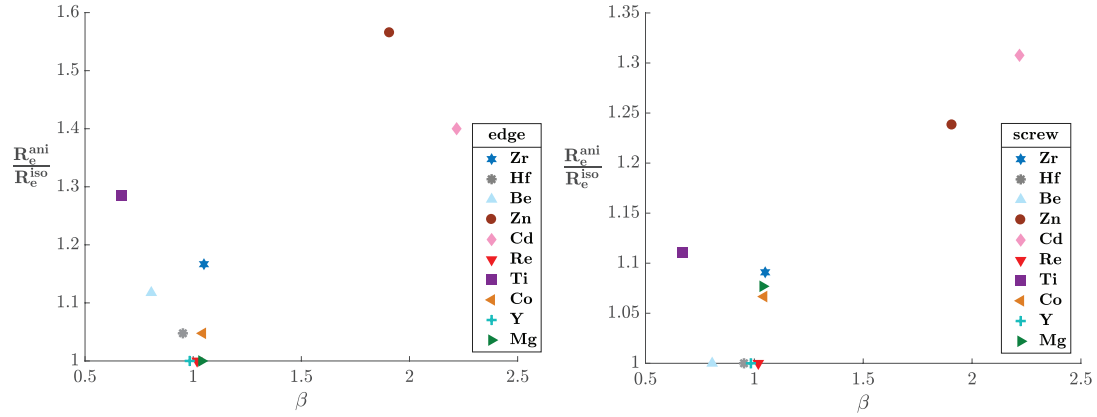

(b)

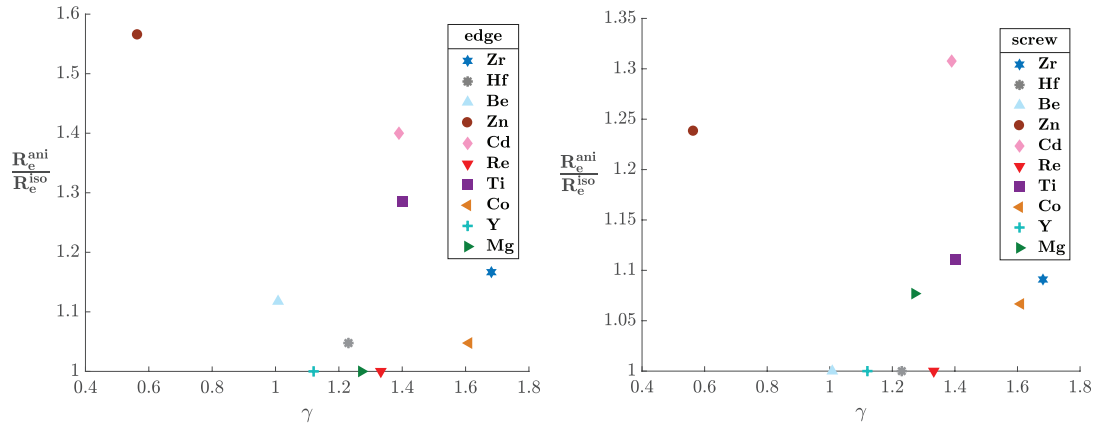

(c)

Figure 3.D.1: *The ratio of the anisotropic to the isotropic equilibrium SFW* R_e^{ani}/R_e^{iso} *plotted against the anisotropy indices (a)* α*, (b)* β*, and (c)* γ *for both edge and screw dislocation dissociation.*

Chapter 4

Dynamic dislocation core structures in HCP materials

In the previous chapters we developed and applied the PFDD model to explore the equilibrium stacking faults of dissociated dislocations and their cores on the basal and pyramidal II planes in HCP materials. In this chapter we will activate an externally applied shear stress in the PFDD model to explore the dynamic stacking faults of dissociated dislocations and their cores as they glide within their respective slip planes. First we will determine if there is any directional dependency on dislocation morphology using the same setup of an isolated infinitely long dislocation. We will then introduce a new initial dislocation configuration, the Frank-Read source, and explore how applied stress directionality influences dislocation loop formation morphology.

4.1 Directionally dependent dislocation glide on the pyramidal II plane

In this work we used the same version of the PFDD model that was developed and described in 3.1.

The previous studies show the partial dislocations on the pyramidal II plane under stress-free conditions exhibit asymmetric cores and morphology, and have Burgers vectors unequal in magnitude, corresponding to the position of the intrinsic stacking fault energy I [2]. However, we do not know how these dislocations behave under an applied stress. It is proposed that there is a directional dependency on the dSFW and critical stress required for dislocation glide. The simulations from that study are re-run for Mg, Be, and Ti starting with an initial stress $\sigma_i = 0.0000$, allowing the dissociation event to equilibrate before incrementally applying a shear stress until the dislocation becomes mobile. Simulations are ran with an applied stress in both a 'positive' and 'negative' direction, for an initial infinitely long edge dislocation. The equilibrium stacking fault width eSFW and the dynamic stacking fault width dSFW are quantified and given in dimensionless grid points with a grid spacing equal to d/b, where d is the interplanar spacing and b is the magnitude of the Burgers vector. The critical stress σ_c for the onset of dislocation glide is also determined and expressed in terms of the shear modulus μ. The model can be sped up by saving the data to an output file for every i^{th} time step evolution, which we have set to $i = 50$ for these simulations. The set-up of the infinitely long dislocation is the same as in the previous chapter (see Figure 3.1.2) with new cell dimension of $512 \times 64 \times 512$ grid points (we are able to reduced the length of the cell in the y-direction to cut down on computational time because the dislocations are infinitely

long with the periodic boundary conditions). However in this work we use a new data visualization tool, OVITO Basic (Open Visualization Tool) Version 3.1.3, which allows us to define and track the SF as it glides through our simulation cell (the SF is defined slightly differently in this work than it was in the previous chapters).

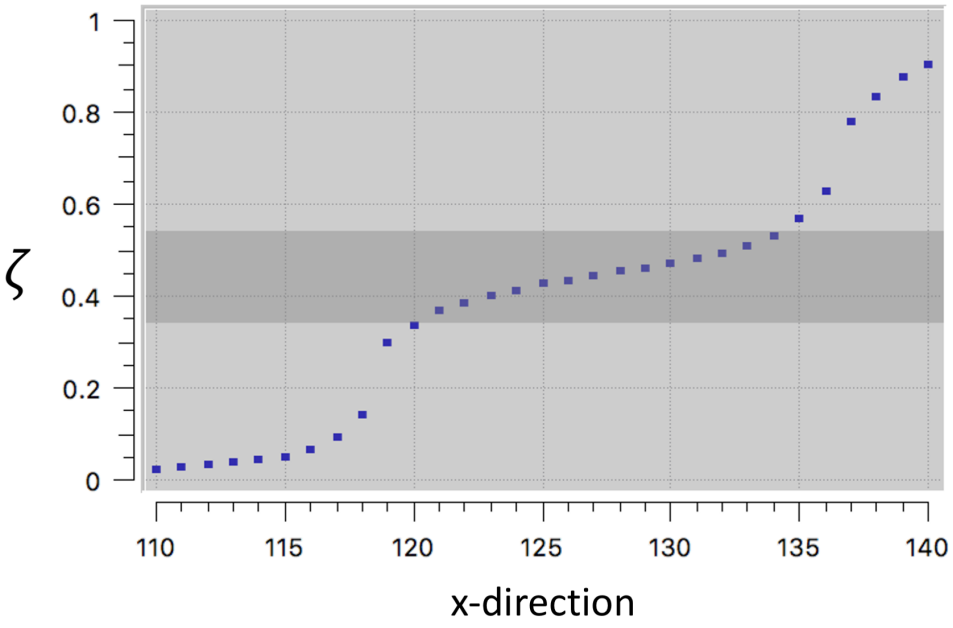

Figure 4.1.1: *The cross-section, showing the order parameter for grid points along the x-direction, of an infinitely long dislocation in Ti that has dissociated forming a stacking fault. The range of order parameter values in Ti that correspond to a stacking fault is* $\zeta = [0.34, 0.54]$ *(highlighted in dark gray).*

The stacking fault is defined according to a range of order parameters that corresponds to the presence of an intermediate step in the order parameter profile, specific to each material. Figure 4.1.1 shows the order parameter profile of the grid points perpendicular to the line sense of an infinitely long edge dislocation in Ti that has dissociated forming a stacking fault. The

order parameter values range from 0 (representing the unslipped regions) to 1 (representing a region that has been slipped by a dislocation). The region where the order parameter transitions from 0 and 1 describes the presence of a dislocation. The intermediate step in this order parameter profile shows that the dislocation has dissociated forming a stacking fault boardered by two partial dislocations. The range of order parameter values in Ti that correspond to a stacking fault is $\zeta = [0.34, 0.54]$ and the number of grid points with an order parameter in that range adds up to the SFW (in previous work the SF contained part of the partial, defined as the difference between the center of the two partials, the two points on the graph where the change in the order parameter was greatest). This new definition and tracking of the SF does not account for any portion of the partial dislocation cores. For ease of reference sake, the two partials will be identified as the left and right partial, corresponding to order parameters $\zeta_l = (0.00, 0.34)$ and $\zeta_r = (0.54, 1.00)$, respectively. This same dislocation reference can be made with the lower and upper bounds of the stacking fault order parameter range for the both Mg and Be as well, which are $\zeta = [0.40, 0.60]$ and $\zeta = [0.38, 0.58]$ respectively.

Figure 4.1.2 shows the generalized stacking fault energy GSFE profiles for the pyramidal II plane in Be, Ti, and Mg, along the $\langle c + a \rangle$ direction (normalized by the Burgers vector). The position of I for Ti is ~ 0.44 which corresponds to the middle of the order parameter range associated with a stacking fault in Ti. The same can be said for Mg and Be, which have an I position of 0.50 and 0.48, respectively. By incrementally applying a shear stress for opposite directions we notice directional dSFW and mobility dependencies that might also be connected to the asymmetries of the pyramidal II plane as captured by the GSFE curves.

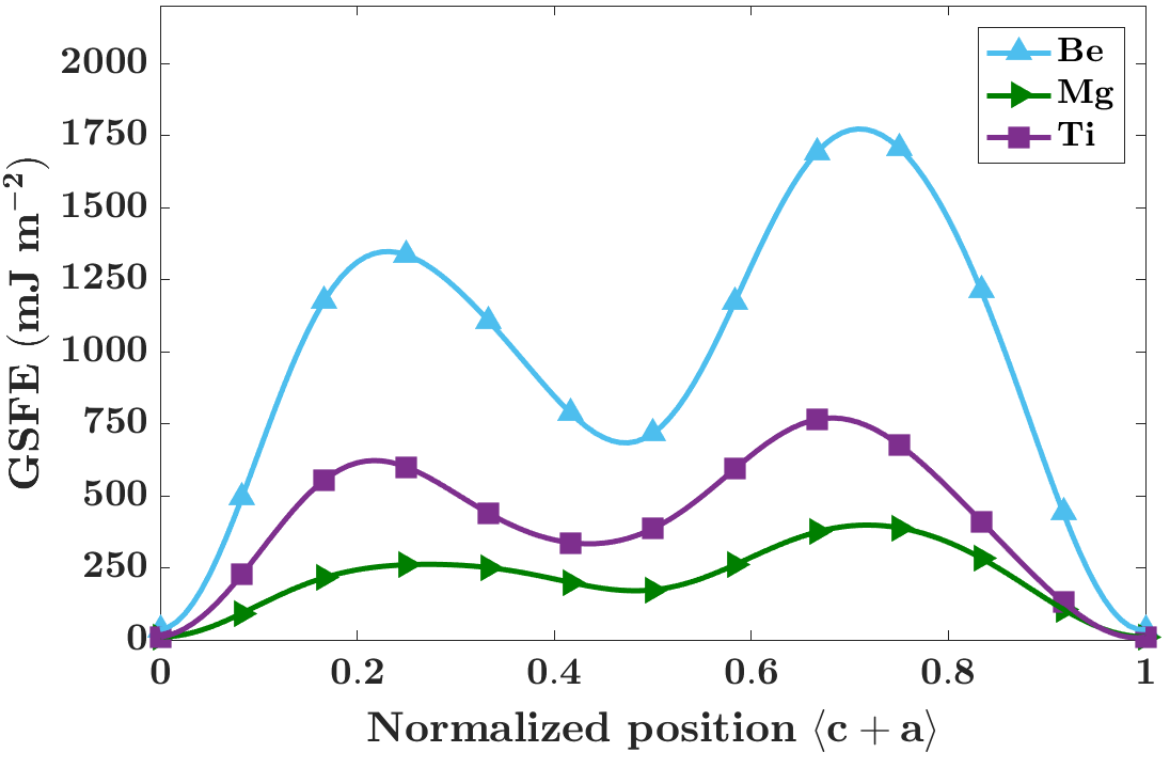

Figure 4.1.2: *The generalized stacking fault energy GSFE curves for Be, Ti, and Mg show various asymmetries for the positions of the local minimum, the intrinsic stacking fault energy I, and the two maxima, the unstable stacking fault energies U_1 and U_2, which correspond to the right and left respectively.*

Figure 4.1.3 demonstrates the directional dependency of the applied shear stress on the dynamic stacking fault width R_d and critical stress σ_c for dislocation glide in Ti. For Ti, $eSFW = 14$ (all SFW are normalized by the grid spacing). At $\sigma_c = 0.0065\mu \pm 0.0005\mu$ we see $dSFW = 15$. In the opposite direction the SFW increases to 15 at $\sigma = -0.002\mu$ as the right partial accommodates this expansion by shifting to the right, while the left partial remains static. At $\sigma = -0.003\mu$ and $\sigma = -0.005\mu$ we see an increase in SFW to 16 and 17, respectively, as the right partial continues to accommodate the

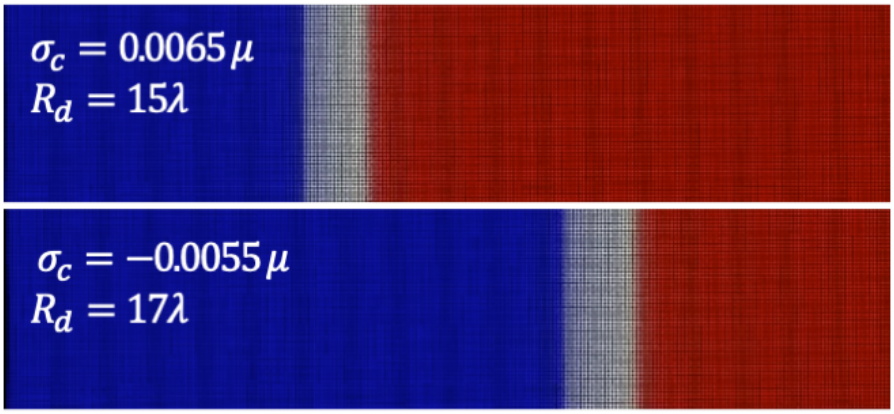

Figure 4.1.3: *Snapshot of dislocation glide in Ti on the pyramidal II plane under two different applied shear stresses. The stress is referred to as the positive in the top picture and the isolated dislocation glides to the left. The stress is referred to as negative in the bottom picture and the dislocation glides to the right. The dynamic stacking fault width R_d and critical stress σ_c for dislocation glide is dependent on the directionality of the applied shear stress.*

expanding stacking fault. At $\sigma_c = -0.0055\mu \pm 0.00005\mu$ we get full dislocation motion to the right and a $dSFW = 16$. This decrease could be due to the smaller Burgers vector associated with the left partial and unstable stacking fault energies that are closer in value (see the GSFE curve for Ti in Figure 4.1.2).

For Mg, $eSFW = 14$. The SF expands to $SFW = 15$ at $\sigma = 0.0002\mu$ as the left partial shifts while the right remains static. At $\sigma_c = 0.00105\mu \pm 0.00005\mu$ the SF begins to glide left with a $dSFW = 16$. In the opposite direction the $dSFW = eSFW$ and $\sigma_c = -0.00135\mu \pm 0.00005\mu$.

For Be, $eSFW = 16$. The static stacking fault SF expands under stress via the left partial to $SFW = 18$ and then at $\sigma_c = 0.00265\mu \pm 0.00005\mu$ we see the SF reduce to a $dSFW = 17$. Consider the GSFE curve for Be in Figure 4.1.2, it is proposed the decrease in the dSFW could result from

the right partial overcoming the maximum unstable stacking fault energy U_2 and having enough momentum to make it over the lower unstable stacking fault energy U_1. Immediately upon the application of stress in the opposite direction, the SF decreases to $SFW = 15$. The static SF eventually recovers and expands to $SFW = 17$ via the right partial dislocation until $\sigma_c = -0.00245\mu \pm 0.00005\mu$ initiates SF glide with a $dSFW = 18$.

Now that it has been established that directionality impacts dislocation behavior on the pyramidal II plane in ways that are intrinsic to each material, we will consider a Frank-Read FR source in Mg for both edge and screw dislocations on both the basal (no directional dependency) and pyramidal II planes (directional dependency).

4.2 Frank-Read source

The FR source is created by considering two slip systems in the PFDD formulation with the same Burgers vector but perpendicular slip plane normals. Figure 4.2.1 depicts this configuration. The first slip plane has a normal in the z-direction and corresponds to the slip plane of interest. The second slip plane has a normal in the x-direction. In the case of a basal plane of interest, both planes will have an $\langle a \rangle$ dislocation. In the case of a pyramidal II plane of interest, both planes have a $\langle c + a \rangle$ Burgers vector. A "prismatic loop" is created on the second plane that spans between $z = 0$ and $z = N/2$, where N is the number of grid points λ in the z-direction. The width of the prismatic loop is considered for both 20λ and 40λ cases. The order parameters for the second slip system are set to 1 for grid points within the prismatic loop, while all other order parameters are set to 0. Only the plane at $z = N/2$ is allowed to evolve during the simulation, so the prismatic loop remains sta-

tionary while a dislocation on the first slip system bows out onto the habit plane.

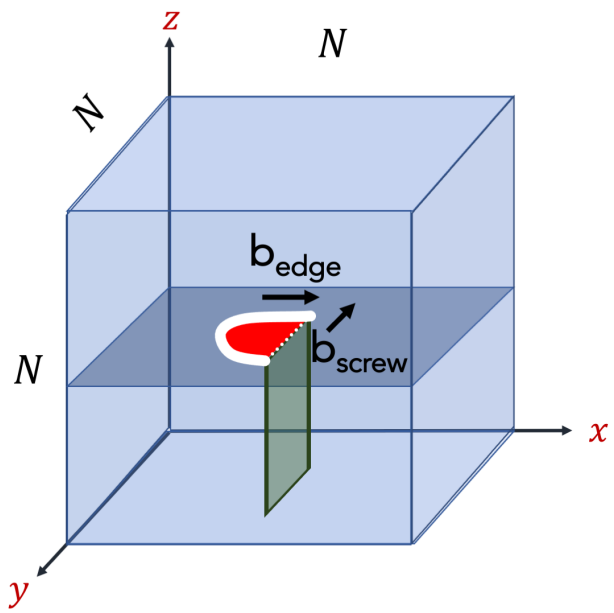

Figure 4.2.1: *The simulation setup for a Frank-Read source. A prismatic loop is shown in green. Under an applied load, a dislocation loop containing partials and a stacking fault, shown in white, bows out from the edges of the prismatic loop on the chosen isolated slip plane in the center of the cell. The blue-white boundary is the leading partial dislocation and the white-red boundary is the trailing partial dislocation. The The Frank-Read source is screw or edge-oriented depending on the orientation of the Burgers vector.*

For all FR simulations, a cubic grid of 256 $\times$ 256 $\times$ 256 is used, though the grid spacings vary between different planes. 3D periodic boundary conditions are used. A shear stress is applied in the Burgers vector direction, starting at zero stress and increasing by increments of 0.001μ. At each stress increment, the simulation evolves for 10000 time steps, Δt or until the simu-

lation converges, whichever comes first. Convergence is defined as when the norm of the change in order parameters is less than $\Delta\zeta = 0.0005$ between successive times. The time step used is $\Delta t = 0.02$ and is unitless in the code. The model can be sped up by saving the data to an output file for every i^{th} time step evolution, which we have set to $i = 100$ for all simulations.

The critical stress σ_c was also calculated for each configuration and is defined as the minimum applied shear stress under which the emitted FR loop will not stall in an equilibrium configuration or collapse back into a straight line if the stress stopped being applied; it is the first stress step in the simulation where the emitted loop continues to expand until the entire simulation cell is slipped. Figures 4.2.2-4.2.12 give detailed specifics on the variety of the FR simulations. These FR source stacking fault loop emissions are the first study of their kind for any hcp material and there are many interesting features that are not fully understood and could very well be different in other hcp materials.

4.2.1 Basal dynamics

Figures 4.2.2 and 4.2.3 show the evolution of a screw dislocation loop emission from a FR source on the basal plane. We consider two initial FR lengths of 20λ and 40λ, respectively, where λ is the grid spacing. The 20λ FR source has a critical stress $\sigma_c = 0.0505\mu \pm 0.0005\mu$ and the 40λ FR source has a critical stress of $\sigma_c = 0.0425\mu \pm 0.0005\mu$.

For an initial edge dislocation in a FR source of length 20λ and 40λ, the critical shear stress is $\sigma_c = 0.0445\mu \pm 0.0005\mu$ and $\sigma_c = 0.0395\mu \pm 0.0005\mu$, respectively. See Figures 4.2.4 and 4.2.5. The critical stresses for these initial edge configurations are less than those previously mentioned for screw. These critical stress values are meant to offer a reference point for those calculated

for the pyramidal II plane. However, this is the first time the evolution of a FR loop with a dissociated dislocation has been simulated on the basal plane in an HCP material, which reveals an interesting asymmetrical SF due to the differences in the directions of the Burgers vectors of the leading and trailing partials. The shape of each resulting dislocation loop, partial and variable dSFW is the result of the lower line energy associated with a screw dislocation versus that for an edge, thus the shape of the FR loop reflects a minimization of parts with an edge character, while maximizing parts with a screw character. We also note that the SF expands greatly before a trailing partial is emitted, which then quickly catches up to the leading partial and a stable dSFW is reached.

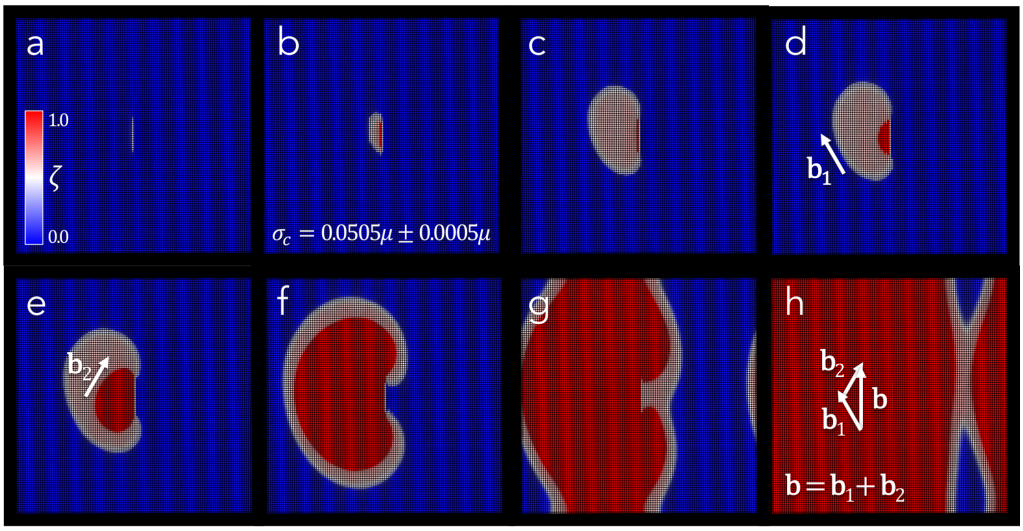

Figure 4.2.2: Screw, FR 20λ, $+\sigma$, basal plane in Mg. Successive snapshots of Frank-Read source loop expansion of an initial screw dislocation on the basal plane in Mg with a Frank-Read source length of 20 grid points (which equates to a normalized length of 16.25b in terms of the Burgers vector $b = 3.1900$ or 51.84 Å).The emitting loop reaches a critical stress of $\sigma_c = 0.0505\mu \pm 0.0005\mu$. Each snapshot shows the formation of a stacking fault at separate timess (τ) of the same simulation. (a) $\tau = 2$ and contains the color map describing the order parameter for Figures 4.2.2-4.2.13. (b) $\tau = 23$ at $\sigma = 0.0500\mu$ right before the critical stress is reached. The remaining snapshots are of the system under the final applied stress $\sigma_f = 0.0510\mu$ for timess (c) $\tau = 120$, where the largest stacking fault width $SFW = 23$ occurs before the emission of the trailing partial from the Frank-Read source, (d) $\tau = 126$, where $\mathbf{b}_1$ is the Burgers vector for the leading partial dislocation, (e) $\tau = 138$, where $\mathbf{b}_2$ is the Burgers vector for the trailing partial dislocation, (f) $\tau = 156$, which captures the equilibrated dynamic stacking fault under this applied stress (once the trailing partial has 'caught up' to leading partial, this stacking fault width remains constant for the remaining loop expansion, until the loop begins to interact with its image due to periodic boundary conditions, as shown in (g) $\tau = 166$, and (h) $\tau = 175$, showing the schematic for the linear combination of partial Burgers vectors on the basal plane for an initial screw dislocation.

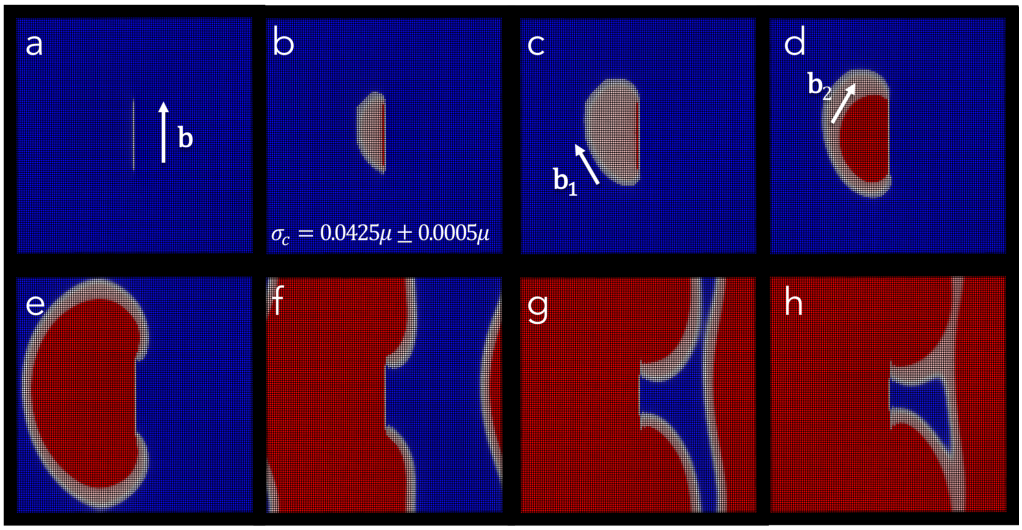

Figure 4.2.3: Screw, FR 40λ, $+\sigma$, basal plane in Mg. Successive snapshots of Frank-Read source loop expansion of an initial screw dislocation on the basal plane in Mg for a Frank-Read source length of 40 grid points (which equates to a normalized length of 32.5b or 103.68 Å). The emitting loop reaches a critical stress of $\sigma_c = 0.0425\mu \pm 0.0005\mu$. (a) is the snapshot at times $\tau = 2$. (b) is $\tau = 69$ at the applied stress $\sigma = 0.0420\mu$ right before the critical stress is reached. The remaining snapshots are of the system under the final applied stress $\sigma_f = 0.0430\mu$ for timesteps (c) $\tau = 162$, where the largest stacking fault width occurs $SFW = 24$, and $\mathbf{b}_1$ is the Burgers vector for the leading partial dislocation, (d) $\tau = 193$, where $\mathbf{b}_2$ is the Burgers vector for the trailing partial dislocation, (e) $\tau = 217$, shows the equilibrated dynamic stacking fault width (f) $\tau = 230$, (g) $\tau = 241$, and (h) $\tau = 243$, which shows the Frank-Read arms asymmetrically merging with their image before merging with each other, unlike in Figure 4.2.2, where the two arms of the Frank-Read source merge forming a complete dislocation loop before meeting its image.

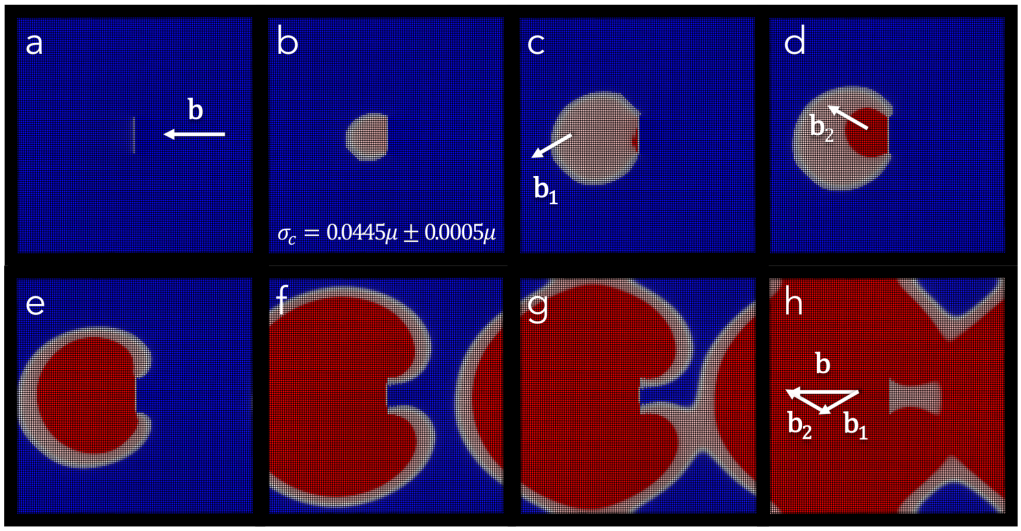

Figure 4.2.4: Edge, FR 20λ, $+\sigma$, basal plane in Mg. Successive snapshots of Frank-Read source loop expansion of an initial edge dislocation on the basal plane in Mg for a Frank-Read source length of 20 grid points The emitting loop reaches a critical stress of $\sigma_c = 0.0445\mu \pm 0.0005\mu$. Each sequential snapshot shows various normalized times τ of the same simulation. (a) is the snapshot at time $\tau = 2$. (b) is the last time $\tau = 213$ at the stress $\sigma = 0.0440\mu$ right before the critical stress is reached. The remaining snapshots are at the final applied stress $\sigma_f = 0.0450\mu$ for times (c) $\tau = 268$, where the largest stacking fault width occurs $SFW = 42$ before the emission of the trailing partial from the Frank-Read source, and $\mathbf{b}_1$ is the Burgers vector for the leading partial dislocation, (d) $\tau = 287$, where $\mathbf{b}_2$ is the Burgers vector for the trailing partial dislocation, (e) $\tau = 321$, shows the equilibrated dynamic stacking fault width, (f) $\tau = 356$, (g) $\tau = 361$, which shows an asymmetric attraction of the leading partial arm of the Frank-Read source with the merging leading partials of the image, and (h) $\tau = 367$, where the schematic for the linear combination of partial Burgers vectors on the basal plane for an initial edge dislocation is noted for the red region, which has been slipped by both the leading and trailing partial dislocations.

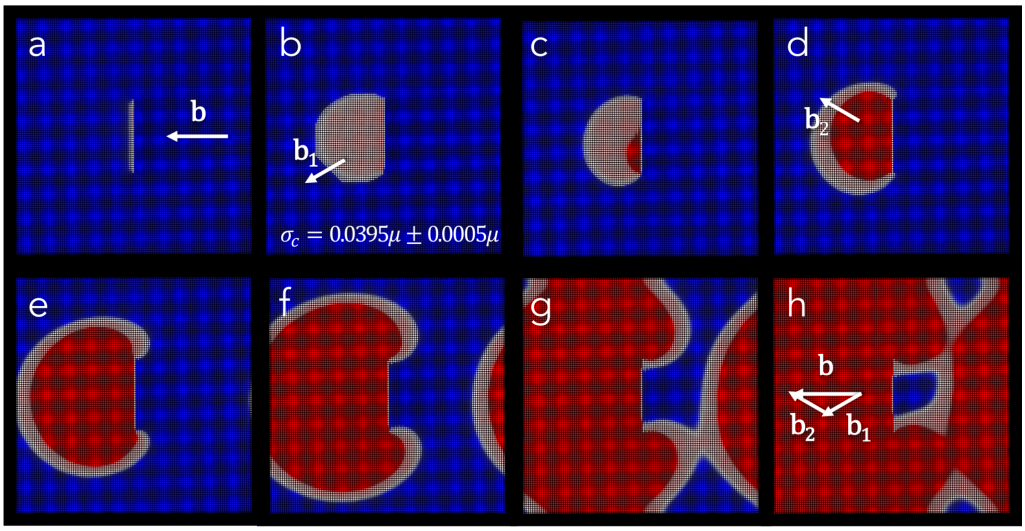

Figure 4.2.5: Edge, FR 40λ, $+\sigma$, basal plane in Mg. Successive snapshots of Frank-Read source loop expansion of an initial edge dislocation on the basal plane in Mg for a Frank-Read source length of 40 grid points The emitting loop reaches a critical stress of $\sigma_c = 0.0395\mu \pm 0.0005\mu$. (a) is the snapshot at time $\tau = 2$. (b) is $\tau = 315$ at $\sigma = 0.0390\mu$ with a maximum $SFW = 46$ right before the critical stress is reached. Both (a) and (b) are from the first simulation, which timed out before completion. The remaining snapshots are representative of a stress greater than $\sigma_c = 0.0395\mu \pm 0.0005\mu$ for times (c) $\tau = 19$, where the largest stacking fault width occurs as the trailing partial begins to emit from the Frank-Read source (d) $\tau = 29$, (e) $\tau = 42$, shows the equilibrated dynamic stacking fault width, (f) $\tau = 51$, (g) $\tau = 57$, which shows an asymmetric attraction of the leading partial arm of the Frank-Read source with the merging leading partials of the image, and (h) $\tau = 60$, where the schematic for the linear combination of partial Burgers vectors on the basal plane for an initial edge dislocation is noted for the red region.

4.2.2 Pyramidal II dynamics

The critical stresses for the pyramidal II plane are larger than those for basal, but not by as much as we would expect. We expected the differences in critical stresses calculated using PFDD to resemble the differences observed in the critical resolved shear stresses CRSS measured for single crystal deformation of the basal and pyramidal II plane (4MPa and 63MPa, respectively). This is perhaps due to the simulations being athermal and thus reflecting what we might expect at 0K, which there are not any experiments on pyramidal II dislocations in Mg at 0K for comparison. For the screw dislocation with a FR length of 20λ and 40λ we see $\sigma_c = 0.0655\mu \pm 0.0005\mu$ and $\sigma_c = 0.0515\mu \pm 0.0005\mu$, respectively. In the negative direction we see very different results with $\sigma_c = -0.0735\mu \pm 0.0005\mu$ and $\sigma_c = -0.0545\mu \pm 0.0005\mu$ respectively. We also see very different morphology during evolution. For example, for the FR length of 40λ we get a maximum stacking fault width (measured perpendicular and across the center of the FR source) of $SFW = 64$, shown in Figure 4.2.8(g) compared to the maximum $SFW = 20$ in Figure 4.2.9(c). The directional dependency of the maximum stacking fault width is even greater for a FR length of 20λ, with $SFW = 110$ Figure 4.2.6(e) and $SFW = 36$ Figure 4.2.7(d) in the positive and negative applied stress directions, respectively.

For the edge dislocation with a FR length of 20λ and 40λ we see $\sigma_c = 0.0555\mu \pm 0.0005\mu$ and $\sigma_c = 0.0455\mu \pm 0.0005\mu$, respectively. In the negative direction we similar results for FR length 20λ with $\sigma_c = -0.0555\mu \pm 0.0005\mu$ and lower results for FR length 40λ with $\sigma_c = -0.0375\mu \pm 0.0005\mu$. We also see directional dependency on dislocation morphology during evolution. Where the FR length of 40λ produces a maximum stacking fault width of $SFW = 47$ early on, before emitting a trailing partial, shown in Figure

4.2.12(b), compared to the maximum $SFW = 21$ when the shear stress is applied in the negative direction, as shown in Figure 4.2.13(b). While the directional dependency of the maximum stacking fault width is smaller (which was not the case for the screw dislocation) for a FR lenghth of 20λ, with $SFW = 38$ Figure 4.2.10(c) and $SFW = 23$ Figure 4.2.11(c) in the positive and negative applied stress directions, respectively.

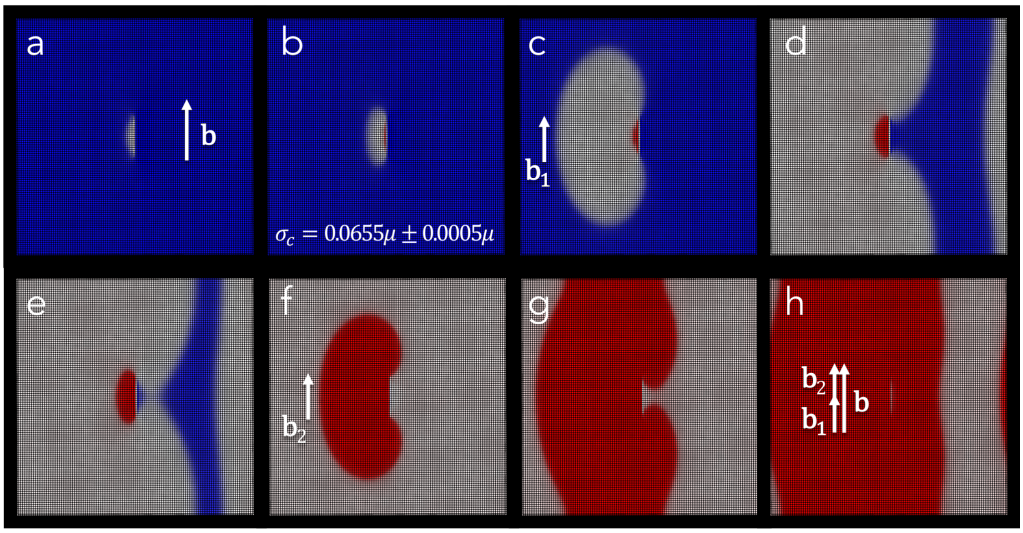

Figure 4.2.6: Screw, FR 20λ, $+\sigma$, pyramidal II plane in Mg. Successive snapshots of Frank-Read source loop expansion of an initial screw dislocation on the pyramidal II plane in Mg for a Frank-Read source length of 20 grid points (which equates to a normalized length of 4.464b or 27.17 Å) . The emitting loop reaches a critical stress of $\sigma_c = 0.0655\mu \pm 0.0005\mu$. (a) is at time $\tau = 2$. (b) is at $\tau = 68$ under the applied stress $\sigma = 0.0650\mu$ right before the critical stress is reached. The remaining snapshots are at the final applied stress $\sigma_f = 0.0660\mu$ for times (c) $\tau = 124$ just as the the trailing partial is emitted from the Frank-Read source, (d) $\tau = 130$, where we see the stacking fault width continuing to expand with the leading partial at a greater rate than the expansion of the trailing partial, (e) $\tau = 131$, where a maximum dSFW of 110 grid points across and a maximum stacking fault area of 15692 grid points are reach, (f) $\tau = 135$, the entire plane has turned into a stacking fault with the cancellation of the leading partials, except for the region that is finally being swept out by the expanding trailing partial (g) $\tau = 137$, and (h) $\tau = 138$, where the schematic for the linear combination of partial Burgers vectors on the pyramidal II plane for an initial screw dislocation is noted for the red region.

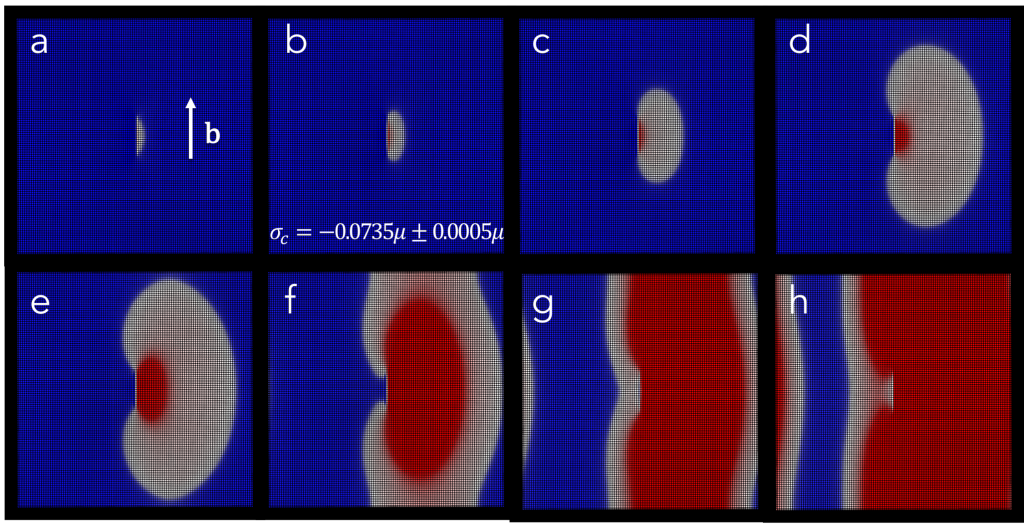

Figure 4.2.7: Screw, FR 20λ, $-\sigma$, pyramidal II plane in Mg. Successive snapshots of Frank-Read source loop expansion of an initial screw dislocation on the pyramidal II plane in Mg for a Frank-Read source length of 20 grid points with an shear stress applied in the negative direction. The emitting loop reaches a critical stress of $\sigma_c = -0.0735\mu \pm 0.0005\mu$. (a) is the snapshot at time $\tau = 2$. (b) is the last time $\tau = 49$ under the applied stress $\sigma = -0.0730\mu$ right before the critical stress is reached. The remaining snapshots are at the final applied stress $\sigma_f = -0.0740\mu$ for times (c) $\tau = 100$ just as the the trailing partial is emitted from the Frank-Read source, (d) $\tau = 112$, where we see the maximum stacking fault width of 36 grid points across, (e) $\tau = 114$, where we measure the larges stacking fault area of 4660 grid points, (f) $\tau = 116$, (g) $\tau = 117$, and (h) $\tau = 118$.

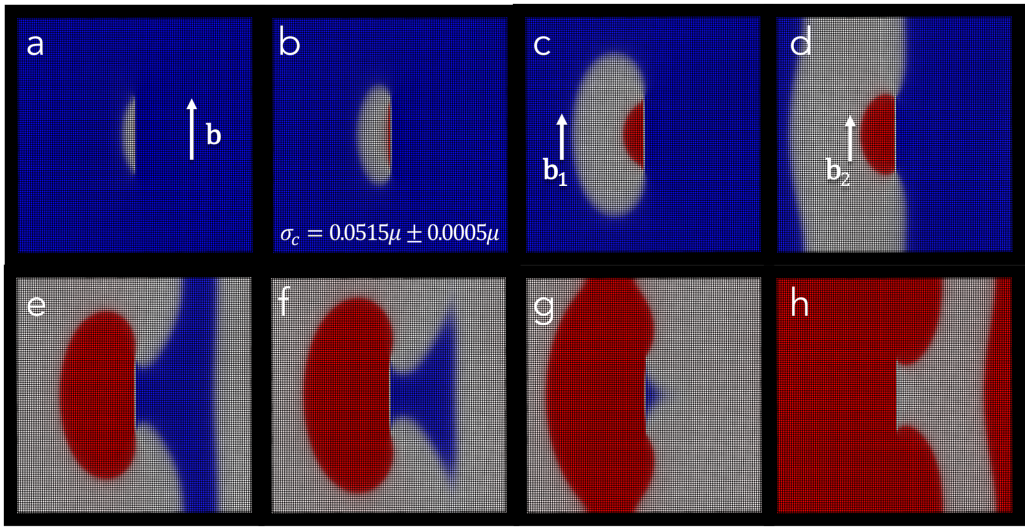

Figure 4.2.8: Screw, FR 40λ, $+\sigma$, pyramidal II plane in Mg. Successive snapshots of Frank-Read source loop expansion of an initial screw dislocation on the pyramidal II plane in Mg for a Frank-Read source length of 40 grid points (which equates to a normalized length of 8.927b or 54.34 Å) . The emitting loop reaches a critical stress of $\sigma_c = 0.0515\mu \pm 0.0005\mu$. (a) is the snapshot at time $\tau = 2$. (b) is at $\tau = 102$ with $\sigma = 0.0510\mu$ right before the critical stress is reached. The remaining snapshots are at the final, applied stress $\sigma_f = 0.0520\mu$ for times (c) $\tau = 154$ just as the the trailing partial is emitted from the Frank-Read source, (d) $\tau = 164$, (e) $\tau = 170$, (f) $\tau = 171$ with a maximum stacking fault area of 9662 grid points, (g) $\tau = 172$ with a maximum dSFW of 64 grid points across, and (h) $\tau = 175$.

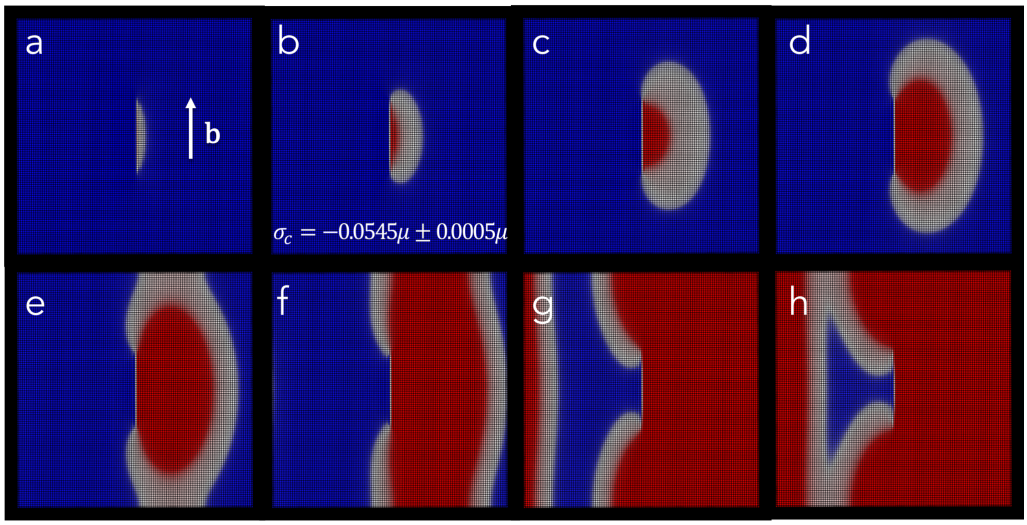

Figure 4.2.9: Screw, FR 40λ, $-\sigma$, pyramidal II plane in Mg. Successive snapshots of Frank-Read source loop expansion of an initial screw dislocation on the pyramidal II plane in Mg for a Frank-Read source length of 40 grid points with a shear stress applied in the negative direction. The emitting loop reaches a critical stress of $\sigma_c = -0.0545\mu \pm 0.0005\mu$. (a) is the snapshot at time $\tau = 2$. (b) is $\tau = 111$ at stress $\sigma = -0.0540\mu$ right before the critical stress is reached. The remaining snapshots are at the final, applied stress $\sigma_f = -0.0550\mu$ for times (c) $\tau = 187$ where we measure the maximum dynamic stacking fault width to be 20 grid points, (d) $\tau = 197$, (e) $\tau = 200$, where we measure the largest stacking fault area of 2540 grid points (this may be exaggerated due to interactions at the periodic boundary), (f) $\tau = 202$, (g) $\tau = 205$, and (h) $\tau = 206$.

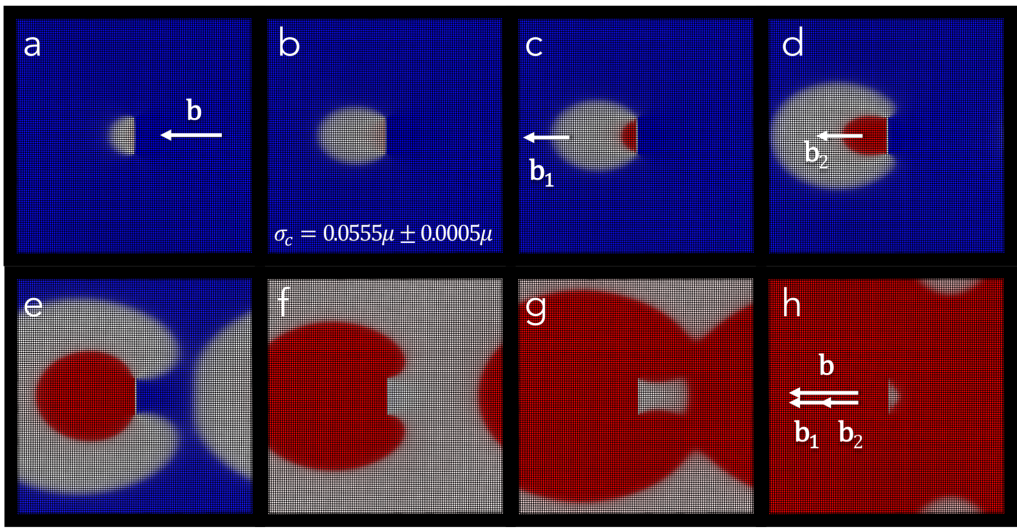

Figure 4.2.10: Edge, FR 20λ, $+\sigma$, pyramidal II plane in Mg. Successive snapshots of Frank-Read source loop expansion of an initial edge dislocation on the pyramidal II plane in Mg for a Frank-Read source length of 20 grid points (which equates to a normalized length of 4.464b or 27.17 Å). The emitting loop reaches a critical stress of $\sigma_c = 0.0555\mu \pm 0.0005\mu$. (a) is at $\tau = 2$. (b) is at $\tau = 95$ under the applied stress $\sigma = 0.0550\mu$ right before the critical stress is reached. The remaining snapshots are at the final, applied stress $\sigma_f = 0.0560\mu$ for times (c) $\tau = 125$ with the maximum dSFW of 38 grid points, (d) $\tau = 138$, (e) $\tau = 148$, (f) $\tau = 151$, shows the cancellation of the leading partial, generating a maximum stacking fault area of 11220 grid points, (g) $\tau = 153$, shows the merging of the trailing partial and (h) $\tau = 154$, where the schematic for the linear combination of partial Burgers vectors on the pyramidal II plane for an initial edge dislocation is noted for the red region.

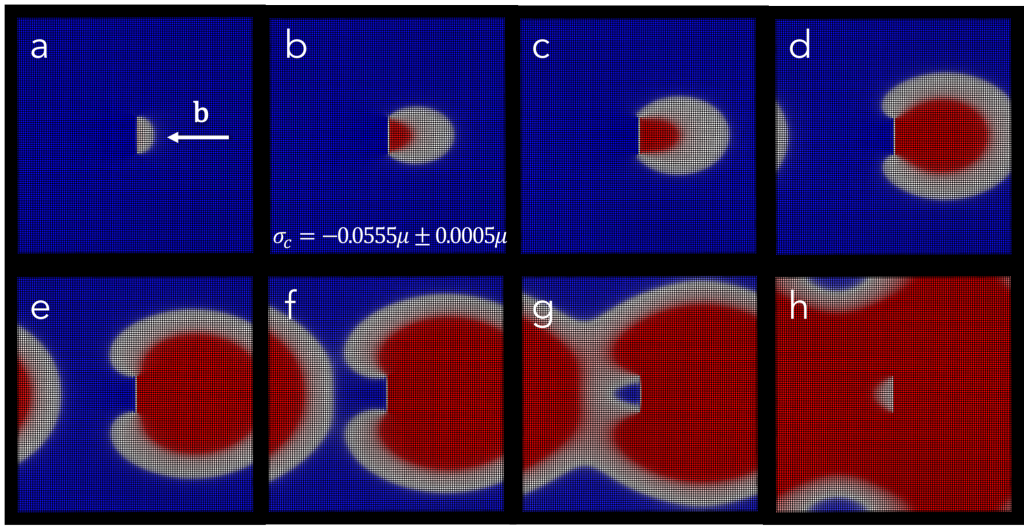

Figure 4.2.11: Edge, FR 20λ, $-\sigma$, pyramidal II plane in Mg. Successive snapshots of Frank-Read source loop expansion of an initial edge dislocation on the pyramidal II plane in Mg for a Frank-Read source length of 20 grid points with a shear stress applied in the negative direction. The emitting loop reaches a critical stress of $\sigma_c = -0.0555\mu \pm 0.0005\mu$. (a) is at $\tau = 2$. (b) is at $\tau = 154$ at the applied stress $\sigma = -0.0550\mu$ right before the critical stress is reached. The remaining snapshots are at the final, applied stress $\sigma_f = -0.0560\mu$ for times (c) $\tau = 202$ with a maximum dynamic stacking fault width of 23 grid points (d) $\tau = 221$, (e) $\tau = 226$, (f) $\tau = 228$, with a maximum stacking fault area of 3125 grid points (g) $\tau = 229$, (h) $\tau = 230$.

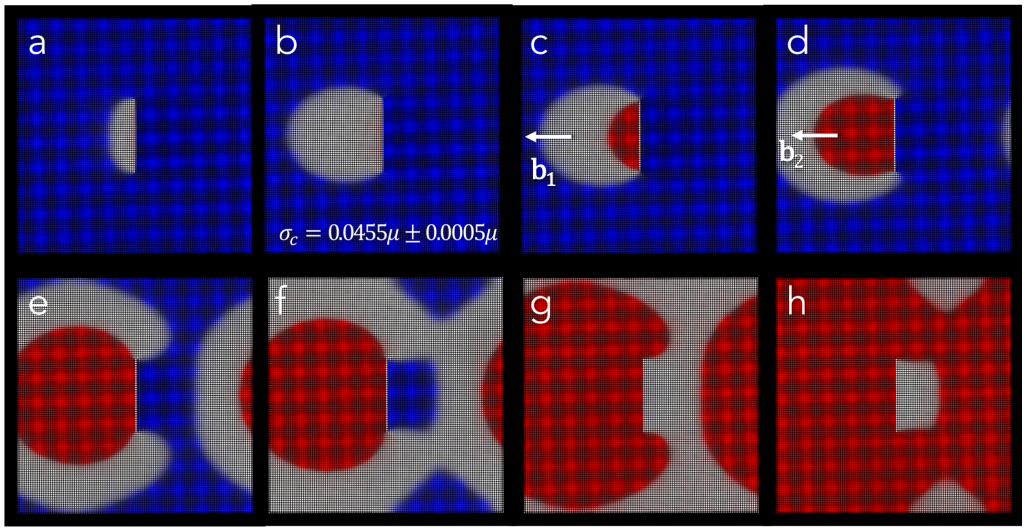

Figure 4.2.12: Edge, FR 40λ, $+\sigma$, pyramidal II plane in Mg. Successive snapshots of Frank-Read source loop expansion of an initial edge dislocation on the pyramidal II plane in Mg for a Frank-Read source length of 40 grid points (which equates to a normalized length of 8.927b or 54.34 Å). The emitting loop reaches a critical stress of $\sigma_c = 0.0455\mu \pm 0.0005\mu$. (a) is at $\tau = 2$. (b) is at $\tau = 121$ at the stress $\sigma = 0.0450\mu$ right before the critical stress is reached and has the largest stacking fault width of 47 grid points. The remaining snapshots are at the final, applied stress $\sigma_f = 0.0460\mu$ for times (c) $\tau = 131$, (d) $\tau = 141$, (e) $\tau = 151$, (f) $\tau = 152$, (g) $\tau = 155$, and (h) $\tau = 156$.

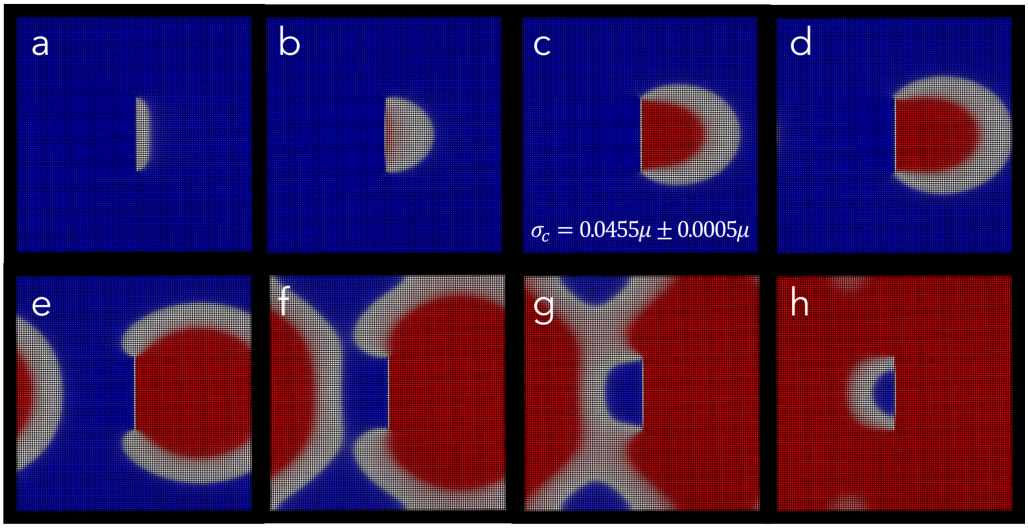

Figure 4.2.13: Edge, FR 40λ, $-\sigma$, pyramidal II plane in Mg. Successive snapshots of Frank-Read source loop expansion of an initial edge dislocation on the pyramidal II plane in Mg for a Frank-Read source length of 40 grid points with a shear stress applied in the negative direction. The emitting loop reaches a critical stress of $\sigma_c = -0.0375\mu \pm 0.0005\mu$. (a) is at $\tau = 2$. (b) is at $\tau = 20$ where the maximum SFW is 21 grid points across, which is interesting because this is the first time the maximum SFW is reached before the critical stress. (c) is at $\tau = 316$ at $\sigma = -0.0370\mu$ right before the critical stress is reached. The remaining snapshots are at the final, applied stress $\sigma_f = -0.0380\mu$ for times (d) $\tau = 370$, (e) $\tau = 410$, (f) $\tau = 416$, which has a maximum stacking fault area of 3624 grid points, (g) $\tau = 417$, and (h) $\tau = 418$.

4.3 Summary

The dSFWs on the pyramidal II plane show a directional dependency on the applied stress that is the result of the variations in the GSFE curves that influence the mobility of the leading and trailing partials.

On planes where the partial Burgers vectors are not colinear (i.e. the basal plane) we see large variations in the dSFW between the leading leading and trailing partial of a FR loop, which expand with different preferential direction depending on the orientation of their partial Burgers vector. We note this for both the initial edge and screw FR source dislocations on the basal plane and that the resulting loop shape varied for each initial dislocation character. The shape of each resulting dislocation loop, partial and variable dSFW is the result of the lower line energy associated with a screw dislocation versus that for an edge. Thus, the shape of the FR loop reflects a minimization of parts with an edge character, while maximizing parts with a screw character.

In both edge and screw initial FR dislocation sources the SF emitted on the pyramidal II plane was symmetric about the axis perpendicular to the FR source, unlike the loop we saw on the basal plane. This is because the Burgers vectors for the partials on the pyramidal II plane are colinear. It is also noted that in all planes the initial screw dislocations formed SF that preferred to spread wider along the y-axis direction parallel to the FR source, while the initial edge dislocation formed SF that preferred to spread more widely along the x-axis direction, perpendicular to the FR source. In all cases this is again the result of the lower line energy associated with a screw dislocation versus that for an edge, thus the shape of the FR loop reflects a minimization of parts with an edge character, while maximizing parts with

a screw character.

Chapter 5

Langevin thermal noise addition to the PFDD model

Thermal fluctuations can arise from dissipation mechanisms due to collision of dislocations with surrounding particles, such as phonons or electrons. Rapid collisions and momentum transfers result in random forces on dislocations. These stochastic collisions, in turn, can be regarded as time-independent noise of thermal forces acting on the dislocations. Suppose the exertion of thermal forces follows a Gaussian distribution. Then, thermal fluctuations most likely result in very small net forces due to mutual cancellations. However, they sometimes become large and may cause diffusive dislocation motion, stacking fault width changes, or thermal activation events such as overcoming obstacle barriers. Therefore, a dislocation dynamics simulation model should also account not only for deterministic effects but also for stochastic forces. In this work, accounting for thermal fluctuations will be explored by using the Langevin force equations to include a thermal noise term (also referred to as Langevin force term or thermal fluctuation term) in the Time-Dependent Ginzberg Landau equation (the energy minimization

equation) of the PFDD model.

5.1 PFDD background

The Time-Dependent Ginzburg-Landau (TDGL) phase field (PF) approach has proven to be a powerful technique for probing the kinetics and dynamics of a system [152, 90, 31, 153, 154]. PF formulations utilize a set of order parameters that track a property of interest as the system evolves spatially and/or temporally. Systems in which researchers have employed PF theory include, but are not limited to, phase transformation [155], microstructure formation [156], phase nucleation/decomposition [157], fracture [158], and defect processes [33]. In this work, we utilize PF formulation for the study of dislocation movement, known as Phase Field Dislocation Dynamics (PFDD) [31]. Detailed overviews of the mesoscale PFDD methodology can be found elsewhere [31, 38, 95], but briefly, a set of order parameters are introduced into the formulation to track slipped vs. unslipped regions during dislocation glide. The system evolution is governed by a minimization of total energy, and the order parameter is solved for at each time step as the system moves towards equilibrium.

Initially, the PFDD formulation was limited to simulations of FCC crystal structures, which provided insight into the nucleation and motion of defects (e.g., screw-, edge-, and mixed-type dislocations, twins). More recently, significant advancements have been made to study BCC [41, 96] and HCP [1, 2] crystal structures, multiple slip systems [159], and chemically disordered crystals [160, 159, 161](i.e., multi-principal element alloys). In this chapter, we introduce a thermal component to the previously static (0 K) PFDD code to capture the role that temperature plays on dislocation nucleation, mi-

gration, and glide. Though temperature capabilities have been successfully introduced into PF phase transformation models [162, 163, 164, 165], applications to dislocation dynamics have not yet been reported in literature. This work is the first treatment of thermal fluctuations in PF dislocation mechanics. We demonstrate the viability of the thermal noise addition with three exemplar HCP crystal systems. Thermal and applied stress effects are investigated on the multiplication of dislocations from a Frank-Read source. Ultimately, the thermal addition to the PFDD model will help to elucidate the temperature- and stress-dependent deformation mechanisms in metals and metal alloys.

5.2 PFDD formulation

As previously mentioned we will be using a computational approach, using a phase field dislocations dynamics PFDD model. In this section we will review the PFDD formulation through the lens of potential development to include thermal fluctuations. The subsequent advancement of the PFDD to account for thermal noise will then be reviewed in the next section

PFDD is a mesoscale model that uses an energy-minimization phase field approach to study dislocations in FCC, BCC, and HCP metals [1, 160, 31]. The energetics used in the PFDD method are informed by first principle calculations.

The PFDD model uses a non-conserved scalar order parameter $\zeta_\alpha(\mathbf{r})$ to track the dislocation structure, where $\mathbf{r} = (x, y, z)$ is the position in space and α is the slip system with normal $\mathbf{m}^\alpha$ and slip direction $\mathbf{s}^\alpha$. At any point $\mathbf{r}$, $\zeta_\alpha(\mathbf{r})$ will describe the structural state at that point, equalling 0 if unslipped and 1 if slipped by a dislocation. Points that lie along the boundary between

the slipped and unslipped regions have an $\zeta_\alpha(\mathbf{r})$ with an intermediate value, which corresponds to the presence of a dislocation core, including stacking faults. The total energy of the dislocation system is expressed in terms of the order parameters.

$$E(\zeta) = E^{elas}(\zeta) + E^{latt}(\zeta) - E^{ext}(\zeta) \tag{5.2.1}$$

where E^{elas} is the internal elastic strain energy from dislocation interactions with obstacles and other dislocations, E^{latt} is the energy penalty of the strained lattice around the core of a dislocation, and E^{ext} is the external energy resulting from an applied stress. In order to relate the internal elastic energy and the external energy to the system describing order parameters, the plastic strain is utilized. The plastic strain, expressed in terms of the order parameter is

$$\boldsymbol{\epsilon}^p(\zeta) = \frac{1}{2}\sum_{\alpha=1}^{n} \frac{b_\alpha \zeta_\alpha}{d_\alpha}(\mathbf{s}^\alpha \otimes \mathbf{m}^\alpha + \mathbf{m}^\alpha \otimes \mathbf{s}^\alpha) \tag{5.2.2}$$

where n is the number of active slip systems, b is the magnitude of the Burgers vector corresponding with each slip system, and d_α is the interplanar spacing for the slip plane. The standard expression for the elastic and external energy are expressed as

$$E^{elas}(\boldsymbol{\epsilon}, \zeta) = \frac{1}{2}[\boldsymbol{\epsilon} - \boldsymbol{\epsilon}^p(\zeta)] \cdot \mathbf{C}[\boldsymbol{\epsilon} - \boldsymbol{\epsilon}^p(\zeta)] \tag{5.2.3}$$

$$E^{ext}(\zeta) = \boldsymbol{\sigma}^{appl} \cdot \boldsymbol{\epsilon}^p(\zeta) \tag{5.2.4}$$

where $\mathbf{C}$ is the elastic stiffness tensor, $\boldsymbol{\epsilon}$ is the total strain, and $\boldsymbol{\sigma}^{appl}$ is the externally applied stress tensor [90]. In general, the lattice energy $E^{lattice}$ can be written as

$$E^{latt} = \sum_{\alpha=1}^{n} \phi_\alpha(\zeta_1(\mathbf{r}), ..., \zeta_i(\mathbf{r})) \tag{5.2.5}$$

where $\phi_\alpha(\zeta_1(\mathbf{r}), ..., \zeta_i(\mathbf{r}))$ is a periodic potential describing either the $\gamma-$surface in the case of the basal plane which requires the use of three order parameters ($i = 3$), or the generalize stacking fault energy GSFE profile in the case of the pyramidal II plane, which only requires one order parameter ($i = 1$) [1].

The PFDD formulation is general and application to different material systems falls largely on choice of energetic terms, and their parameters and functional forms. Up to now research has focused on deterministic effects, but the PFDD model should also account for stochastic forces. The conventional phase field dynamics equations, i.e. time-dependent Ginzburg Landau (TDGL) equation, are athermal deterministic, describing only dissipative processes because the time derivatives of the total energy functional, by integrating the dynamic equations, are always non-positive

$$\frac{\partial \zeta(\mathbf{r}, t)}{\partial t} = -L \frac{\delta E(\zeta)}{\delta \zeta(\mathbf{r}, t)} \tag{5.2.6}$$

where ζ is a scalar order parameter used to describe the state of a system i.e. dislocation events, L is the coefficient of mobility, and E is the total athermal energy of the system i.e. elastic interaction energy, lattice energy, externally applied stress energy. Thus, modeling thermally aided events i.e. emission of a dislocation loop from a Frank-Read FR source, requires incorporation of additional physical terms that describe thermally activated processes. This can be achieved using the Langevin force approach [166, 167]. The approach is an analogue to the treatments for Brownian motion in non-equilibrium statistical mechanics, which mimics the thermal interactions between the system and the environment in terms of phenomenological force terms [168, 163]. That is to say, when there is a process that dissipates energy, turning it into heat (i.e. friction), there is a reverse process related to thermal fluctuations (noise). Both friction and noise come from the interaction with the environ-

ment, related by the Fluctuation-Dissipation Theorem [169, 170, 171].

The essence of Langevin's method is to rewrite his Newtonian-like equation of motion of the random variable describing the dynamics of a representative point in phase space in variables corresponding to the desired observable(s). Then one averages the new equation over its realizations, yielding the deterministic evolution equation for the observable(s). Once a potential is involved, the Langevin equation generates coupled stochastic differential-recurrence equations which, when averaged using the properties of Gaussian white noise, become a deterministic hierarchy of coupled equations for the observables [172].

The TDGL equation (Equation 5.2.6), used in the phase field dislocation dynamics PFDD model, assumes the rate of evolution of a field is a linear function of the thermodynamic driving forces. This allows for the addition of a Langevin thermal force term , $\theta(\mathbf{r}, t)$, to the TDGL equation to reproduce thermal fluctuations [89] as

$$\frac{\partial \zeta(\mathbf{r}, t)}{\partial t} = -L \frac{\delta E(\zeta)}{\delta \zeta(\mathbf{r}, t)} + \theta(\mathbf{r}, t) \tag{5.2.7}$$

In the next section we will look at the derivation of $\theta(\mathbf{r}, t)$ from the Langevin force equations.

5.3 Langevin force equations

The effects of the fluctuating force due to thermal noise θ can be summarized by giving its first and second moments, as averages in space and time over infinitesimal space and time intervals [165, 163, 173]. The Langevin force terms are assumed uncorrelated in both space and time, requiring their first and second moments to satisfy

$$\langle \theta(\mathbf{r}, t) \rangle = 0 \tag{5.3.1}$$

$$\langle \theta(\mathbf{r}, t)\theta(\mathbf{r}', t')\rangle = 2k_B T L\delta(t - t')\delta(\mathbf{r} - \mathbf{r}') \tag{5.3.2}$$

where k_B is Boltzmann's constant, relating the average kinetic energy for each degree of freedom of a physical system in equilibrium to its absolute temperature in Kelvin, T; L is the mobility coefficient from the time-dependent Ginzburg-Landau equation; $\mathbf{r}$ and t represent any point in space and time respectively, and $\mathbf{r}'$ and t' also represent any point in space and time respectively. The delta function in space and time indicate that there is no correlation between impacts in any distinct time and space intervals [169].

Thermal noise is a statistical noise and is often described as a Gaussian white noise, in which the values at any pair of times are identically distributed and statistically independent (and hence uncorrelated). Thus, thermal noise has a probability distribution function equal to that of a Gaussian distribution. The results of a calculation using the Langevin equation are expected to be independent of the initial state and to involve only the statistical distribution of the noise [163]. In this view, the averages in Equations 5.3.1 and 5.3.2 come from averages over initial states, yielding a Gaussian distribution in discrete form as

$$\langle \theta(n, m)\rangle = 0 \tag{5.3.3}$$

$$\langle \theta(n, m)\theta(n', m')\rangle = 2k_B T L\frac{\delta_{mm'}}{\Delta t}\frac{\delta_{nn'}}{d_x d_y d_z} \tag{5.3.4}$$

where n (and n') and m (and m') are respectively the indices of discrete spatial position corresponding to the structured grid of the simulation cell, and the indices of discrete temporal moments corresponding to the time step interval over which the simulation is evolved; d is the grid spacing in the x, y, and z direction; Δt is the time step; and δ_{ij} is the Kronecker delta.

In order to write these discrete Langevin equations into the PFDD model, the Kronecker deltas can be expressed with a computer-generated Gaussian distribution [163]. If $\{\rho : \rho_i, i = 1, ...\}$ represents a series of computer-generated Gaussian distributed random numbers that satisfy $\langle \rho_i \rangle = 0$ and $\langle \rho_i \rho_{i'} \rangle = \delta_{ii'}$ then the discrete Gaussian thermal noise term can be rewritten as

$$\theta(n, m) = \sqrt{\frac{2k_B TL}{d_x d_y d_z \Delta t}} \rho \tag{5.3.5}$$

satisfying the same first and second moment requirements given in Equations 5.3.3 and 5.3.4.

The PFDD model will be able to evolve the metastable states of the phase field, accounting for the additional Langevin force perturbations associated with temperature. At these metastable states, the balance between this perturbing Langevin force and the restoring total phase-field energy gradient determines the fluctuation amplitude of the phase fields according to the fluctuation–dissipation theorem.

5.4 Addition of thermal noise to the energy functional in PFDD

Now that we have thoroughly covered the PFDD formulation (Section 5.2) and the derivation of the Langevin force equations (Equation 5.3.1 and 5.3.2) into a thermal noise term (Equation 5.3.5), we will walk through the addition of this thermal noise term to the PFDD code, accounting for normalizations and scaling factors utilitzed in the code.

To start, the free energy density $e \Longrightarrow [J/m^3] = [Pa]$ is

$$e = e_{work} + e_{lattice} + e_{elastic} \tag{5.4.1}$$

Our TDGL equation is

$$\dot{\zeta} = -L\frac{e}{\zeta} + \theta \tag{5.4.2}$$

where ζ is a non-conserved order parameter, $L \Longrightarrow [1/Pa.s]$ is a mobility coefficient, and θ is the Langevin force term on ζ due to thermal fluctuations.

In discrete form the TDGL equation is

$$\Delta\zeta = -L\Delta t e' + \theta\Delta t \tag{5.4.3}$$

Note, that $L\Delta t$ are a product and that $e' = \Delta e/\Delta\zeta = e'_{work} + e'_{lattice} + e'_{elastic}$. Each order parameter ζ corresponds with a voxel volume $\Omega = d_x d_y d_z$ around a point in our simulation cell. The discrete TDGL per voxel is then expressed as

$$\Delta\zeta = \frac{-L\Delta t}{\Omega}\Omega e' + \theta\Delta t = \frac{-L\Delta t}{\Omega}E' + \theta\Delta t \tag{5.4.4}$$

where $E' = e'\Omega$ is the change in free energy in ζ

If we normalize the time and energy, we need to choose a material constant, which we've chosen to be the effective shear modulus μ

$$\Delta\zeta = \frac{-L\Delta t}{\Omega}E'\frac{\mu}{\mu} + \theta\Delta t\frac{L\mu}{L\mu} \tag{5.4.5}$$

The TDGL equation written in normalized terms now looks like

$$\Delta\zeta = \Delta t^* E'^* + \theta^*\Delta t^* \tag{5.4.6}$$

where the normalized time increment Δt^* is

$$\Delta t^* = L\mu\Delta t = \mu L\Delta t \tag{5.4.7}$$

and the normalized free energy change is

$$E'^{*} = E'/\phi \tag{5.4.8}$$

where ϕ is an energy scaling factor

$$\phi = \Omega\mu \Longrightarrow [J] \tag{5.4.9}$$

We express the normalized Langevin force term θ^{*} as

$$\theta^{*} = \theta/L\mu \tag{5.4.10}$$

We start with the Langevin term θ in real dimension

$$\theta = \sqrt{\frac{2k_BTL}{\Omega\Delta t}}\rho \tag{5.4.11}$$

where ρ is a set of random numbers with a Gaussian distribution. Our normalized Langevin term in the code is

$$\theta^{*} = \frac{\theta}{L\mu} = \sqrt{\frac{2k_BTL}{\Omega L^2\mu^2\Delta t}}\rho = \sqrt{\frac{2k_BT}{\phi\Delta t^{*}}}\rho \tag{5.4.12}$$

Note that k_BT/ϕ is dimensionless

We generate the Gaussian distributed random numbers using the Box-Muller transform. Since the PFDD model is parallelized, we generate the Gaussian distributed random number set for the entire simulation cell on the master processor and send equipartitioned slices to the parallel processors.

An ad hoc convergence criterion is chosen for $\Delta t^{*} = L\mu\Delta t$ above which the PFDD model fails to run properly as the timestep is too large to meaningfully capture the evolution of our simulation.

Table 5.4.1: *Normalized quantities in the PFDD code.*

Physical parameters	Normalized quantity
timestep, Δt (s)	$\Delta t^* = \Delta t L \mu$
energy, E (Pa m^3)	$E^* = E/\Omega\mu$
Langevin force term, θ (1/s)	$\theta^* = \theta/L\mu$

5.5 Results

We consider dislocation behavior at various temperatures in Mg, Ti, and Zr, as they are the more commonly studied of the HCP materials, with Mg being the most studied. We focus on the pyramidal II plane and start with a Frank-Read dislocation source with an initial edge Burgers vector. Since different deformation processes turn on at higher temperatures we limit the temperatures we explore to $T/T_m \leq 0.5$, where T_m is the melting temperature for each material. i.e. we would expect diffusion processes to turn on for temperatures above $T/T_m = 0.5$ and the PFDD model does not account for these diffusion processes so any results would not fully capture all that is physically taking place at those higher temperatures. For Mg with a melting temperature less than half of that of Ti and Zr we consider T = 0K, 4.2K, 77K, 100K, 200K, 300K, and $T/T_m = 0.5$, where $T_m^{Mg} = 923.1$K. We chose 4.2K and 77K since they are the liquid temperatures for helium and nitrogen, respectively, the primary cooling agents used in experiments. While 300K is approximately room temperature. For Ti and Zr with $T_m^{Ti} = 1941$K and $T_m^{Zr} = 2128$K we consider T = 0K, 4.2K, 77K, 100K, 200K, 300K, 400K, 500K, 600K, 700K, 800K, and $T/T_m = 0.5$.

Our empirical convergence criterion for the pyramidal II plane in all mate-

rials is $\Delta t^* = L\mu\Delta t = 0.02$. Our mobility coefficient L is calculated by taking the inverse of the single crystal drag coefficients calculated for pyramidal slip in Reference [174].

Table 5.5.1: *Values used in PFDD.*

Material	mobility, L ($Pa^{-1}s^{-1}$)	shear modulus, μ (Pa)	timestep, Δt (s)
Mg	2.591×10^{-5}	19.260×10^{9}	4.009×10^{-18}
Ti	1.124×10^{-5}	35.667×10^{9}	4.626×10^{-18}
Zi	1.764×10^{-5}	30.226×10^{9}	3.758×10^{-18}

One of the benefits of the PFDD model is it is set up to mathematically evolve the simulation at every timestep Δt, but we are able to speed up the process by not saving that data at every Δt, instead choosing to save the data for every i^{th} timestep. Each output file occurs at what we call a normalized time τ. e.g. if we set our output files to capture every 10^{th} timestep ($i = 10$), then the normalized time of $\tau = 5$, is the 50^{th} timestep, and the amount of time that has actually passed is $t = \tau i\Delta t = 5 * 10 * 3.758 \times 10^{-18}s = 1.8790 \times 10^{-16}s$. So our normalized time $\tau = t/i\Delta t$. This is the measure of time we refer to in all subsequent result graphs.

5.5.1 FR simulation set-up

The FR source is created by considering two slip systems in the PFDD formulation with the same Burgers vector but perpendicular slip plane normals. Figure 5.5.1 depicts this configuration. The first slip plane has a normal in the z-direction and corresponds to the slip plane of interest. The second slip plane has a normal in the x-direction. In the case of a pyramidal II plane

of interest, both planes have a $\langle c+a \rangle$ Burgers vector. A "prismatic loop" is created on the second plane that spans between $z = 0$ and $z = N_z/2$, where N_z is the number of grid points in the z-direction. The width of the prismatic loop is considered for a length of 40 grid points. The order parameters for the second slip system are set to 1 for grid points within the prismatic loop, while all other order parameters are set to 0. Only the plane at $z = N_z/2$ is allowed to evolve during the simulation, so the prismatic loop remains stationary while a dislocation on the first slip system bows out onto the habit plane.

Notice we use a different color bar in this work than in previous visualizations to further emphasize the dislocation dissociation (instead of the order parameter values for slip and unslipped regions). Here the partials (in white), the stacking fault (in red), and the perfect HCP lattice structure (in blue) are easy to identify and track through the system evolution. This proves helpful when multiple dislocation loops are emitted from the FR source. For multiple dislocation loops the stacking faults are given different colors to help differentiate between loops.

The simulation cell with dimension $N_x \times N_y \times N_z$ are set as $512 \times 1024 \times 64$ for these series of simulations. This extended length in the y-direction allows us to observe the expanding loop without mirror image dislocation interactions across the periodic boundaries. Since we are only interested on the unconfined slip plane at $N_z/2$ we are able to reduced the height of the simulation cell, cutting down on the simulation run time. We have made sure to keep N_z large enough that the interaction between mirror image slip planes across periodic boundaries is negligible.

We apply a shear stress large enough to overdrive our FR source at all temperatures ($\sigma > \sigma_c$ from Chapter 4) to ensure the dislocation emissions are

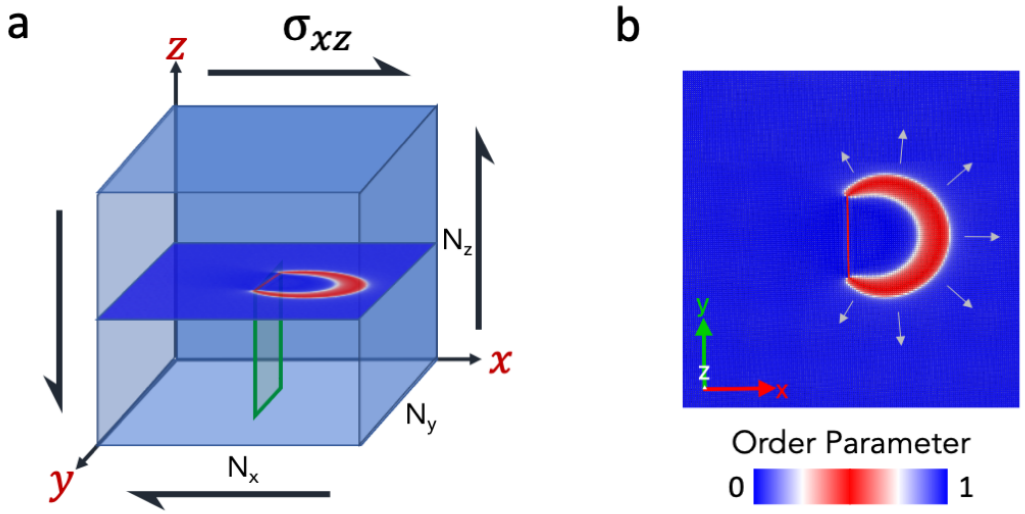

Figure 5.5.1: *Schematic of the evolved, bowed-out dislocation emitted from a Frank-Read source under a shear stress a) as it is initialized in the PFDD simulation cell by the input of a prismatic dislocation loop (in green) and b) a closer look at the slip plane where the stacking fault (red) is preceded by a leading partial (white) and followed by a trailing partial (white).*

under enough stress to reach a steady-state loop formation and not "stall" dislocation glide. We set the shear stress for all simulations (every material at every temperature) to be $\sigma = 0.055\mu$ so we can better compare between each material and temperature effects. Where μ is the shear modulus for each material used to normalize the applied stress. We set the number of timestep evolutions between output files to be i=50, which is small enough to capture key moments in the dislocation loop expansion at all temperatures simulated.

5.5.2 Frank-Read results

First we label some key moments in the FR dislocation loop evolution as shown in Figure 5.5.2 (shown for first and second dislocation loops from the

FR source): emission of leading (a,g) and trailing partials (b,h) from the FR source; critical bowing shape (c,i), after which the loop has overcome the resistant force of the FR source (lowest energy configuration as a straight line between the two pinned ends of the FR source) from which it was emitted; the leading partials meeting (d,j) to form a partial dislocation loop that is separated from the FR source bordering a stacking fault SF that is still attached to the FR source along with the trailing partial; complete dislocation loop formation (e,k) where the trailing partials have also met, annihilating along the small section of meeting, and separating the dislocation loop from the FR source; this leaves a remaining portion of the initial dislocation emission (that has been detached from the outer loop) to be attracted back into alignment with the pinned ends of the FR source (f,l) before bowing out as a 2^{nd} full dislocation from the FR source. This process will continue over and over again, producing successive concentric dislocation loops, as long as the FR source is under a shear stress that exceeds the critical stress needed to bow out beyond the critical shape, which is again depicted in 5.5.2 (c,i). As mentioned earlier, we set our shear stress to be $\sigma = 0.055\mu$ in all simulations.

Using Figure 5.5.2 as a reference for important events captured in each simulation, we made note of the times for each snapshot in each material at each temperature. When considering the time it took for a complete loop to form around the FR source, we first measured from the time the whole dislocation (leading and trailing partials) began to bow out from the FR source (b,h) to the time that the dislocation loop had detached from the FR source (e,k). This time to loop formation was measured for the first and second dislocation emissions for each material at each temperature, the plots for which are shown in 5.5.3 (a). We noticed the similar shape of the curves between the first and second loops and thought to redefine the time

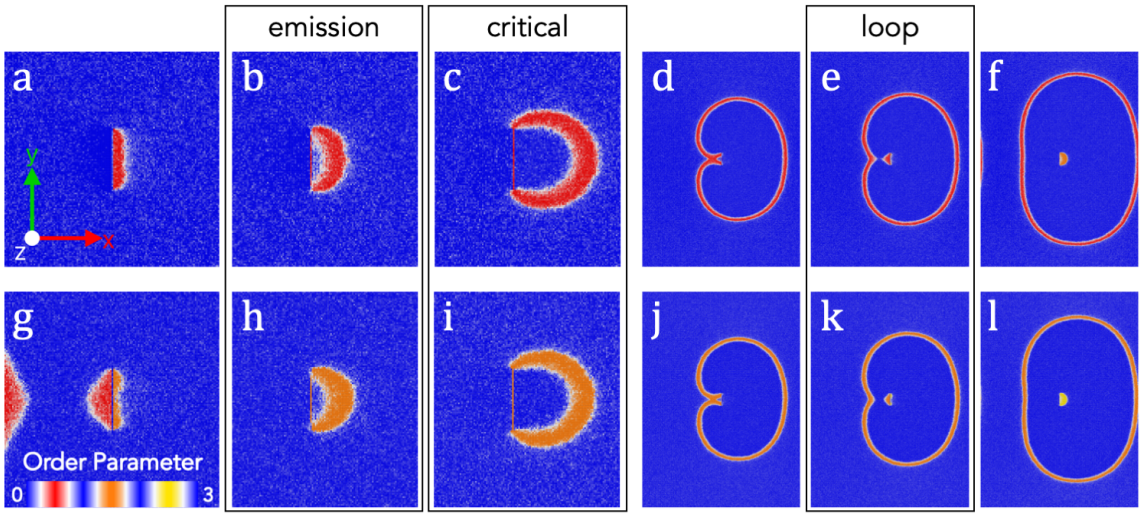

Figure 5.5.2: *Snapshots of dislocation loops emitting from a FR source of* 40 *grid points in length on the pyramidal II plane in Mg at T= 77K under constant shear stress of* $\sigma = 0.055\mu$. *The top row (a-f) show the first loop evolution and the bottom row (g-l) show the second loop. The left three snapshots in each row are a close up on the FR source (a-c,g-i), while the right snapshots have zoomed out to the full width of the simulation cell* ($N_x = 512$) *to capture the full loop evolution (d-f,j-l). The leading partial is emitted for loops 1 and 2 in (a) and (g) respectively. The complete dislocation emission occurs in (b) and (h) when the trailing partial is finally emitted. In (c) and (i) the dislocation has reached its critical bowed out shape. The leading partials first merge, forming a SF loop in (d) and (j). The full dislocation forms a loop in (e) and (k) when the trailing partials meet, detatching the dislocation loop from the FR source. (f) and (l) just show the loop as it continues to expand around the FR source.*

to loop formation to be measured from the time from the critical bowing shape 5.5.2 (c,i) to the loop (e,k). This not only collapsed the graphs for

each loop onto one another (as shown in 5.5.3 (b)), meaning each successive loop once exceeding the critical shape behaved with the same mobility, but we also noted that at higher temperatures $T/T_m \geq 0.4$ the trends for each material aligned, implying that perhaps some kind of "terminal velocity" for dislocation glide exists at high temperatures where the resistance from the lattice energy is negligible.

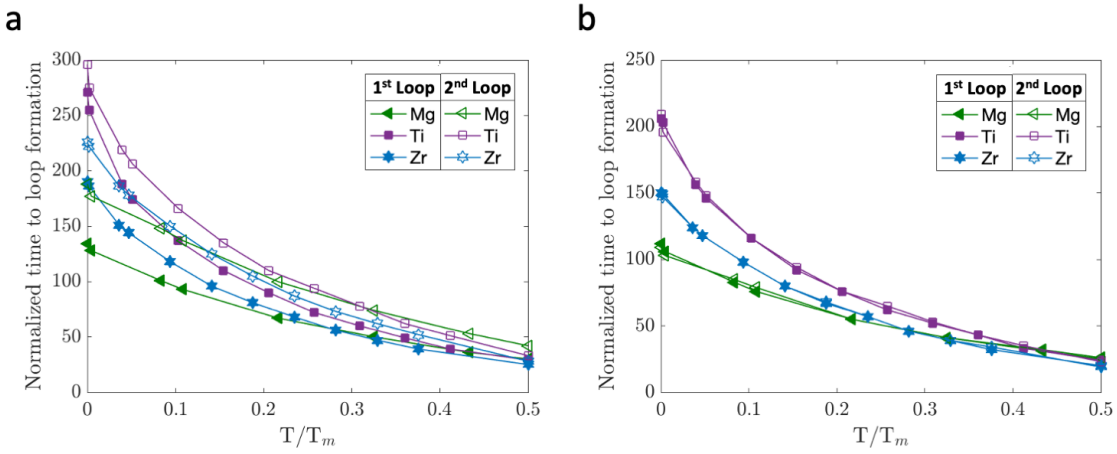

Figure 5.5.3: *The normalized time to loop formation for the first and second loops emitted from a FR source plotted against the temperature at which each simulation was run, normalized by the melting temperature for each material (Mg, Ti, Zr). In (a) the time to loop formation was measured from the moment a full dislocation was emitted from the FR source until the full dislocation loop was detatched from the FR source (See Figure 5.5.2 (b and h) to (e and k)). In (b) the time to loop formation was measured from the critical bow-out shape of the dislocation to the full dislocation loop was formed (See Figure 5.5.2 (c and i) to (e and k)).*

We notice when comparing the loop shape for each material that the dislocation loops are smaller at increasing temperatures (see Figure 5.5.4 and Appendix 5.B). This makes sense when we consider the internal stress

field the two parallel legs of the dislocation bow-out will feel due to one another (see Figure 5.B.2). At higher temperatures this attractive stress field will result in quicker glide and annihilation of the two legs of the dislocation bow-out, before the rest of the loop can expand, which explains the reduction in loop size as temperature increases (see Figure 5.B.1). This trend begins to break down when temperatures near $T/T_m = 0.5$ for Ti and Zr, where we notice a more dramatic oblong shape with a smearing of the stacking fault along the screw portion of the loops (see 5.5.4(d,f).

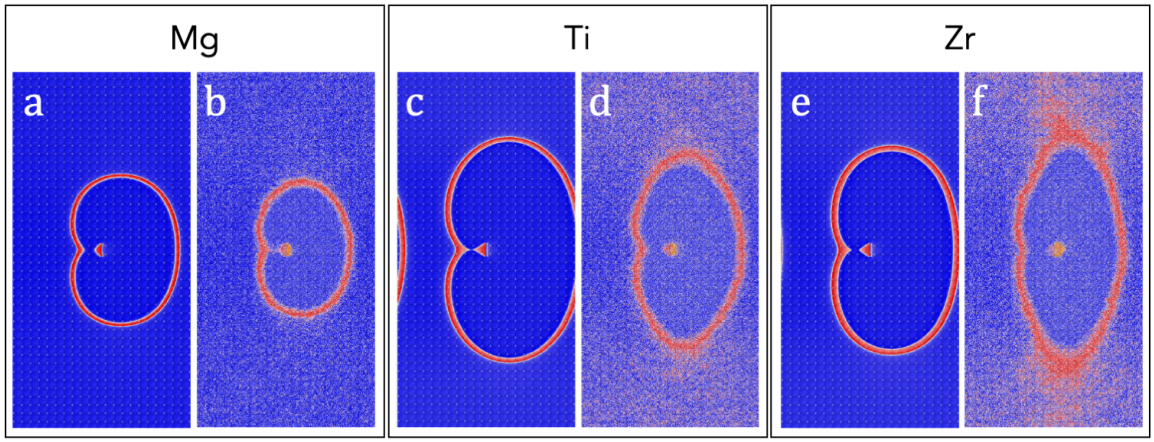

Figure 5.5.4: *For each material Mg, Ti, and Zr we compare the FR loop at the time of full formation at the temperature of liquid helium T=4.2 (a,c,e) and at T/Tm=0.5 (b,d,f)*

This lead us to question how the mobility of dissociated screw and edge dislocations behave differently at different temperatures. We explore this further in the next section where we consider pure edge and screw dislocations using the dipole set-up used in Chapter 3.

5.5.3 Straight edge and screw dislocations

Because of the unique shape of the dislocation loop from the FR source. We wanted to conduct a second set of simulations where we consider infinitely long dislocations with pure edge or pure screw character under the same shear stress of $\sigma = 0.055\mu$ and at the same various temperatures as were used in the FR source simulation. We initialized the same dipole set-up as in Section 3.1.3 with a cell size of $1024 \times 4 \times 64$. The only parameter we changed for this set-up was the number of timesteps between output files, which we decreased to $i = 10$, since the infinitely long pure dislocation will glide faster than the dislocation loop pinned on both end of the FR source. This allows us to capture in more detail the evolution of the dislocation as it glides across the pyramidal II plane. In Figure 5.5.5 the normalized velocities of pure edge and screw dislocations are plotted for each material with respect to the normalized temperatures.

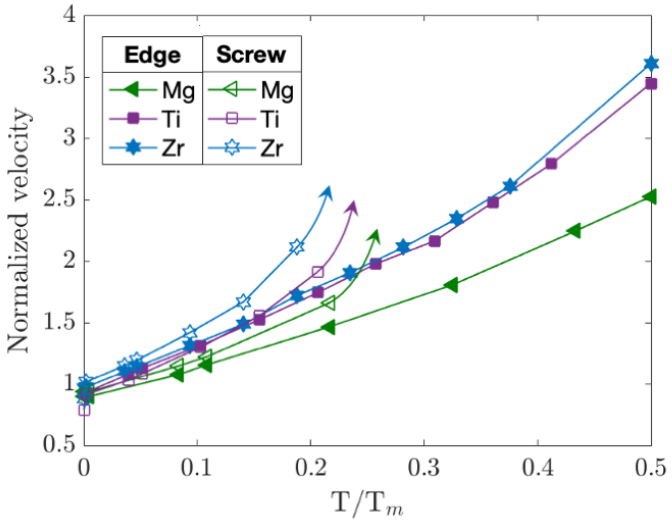

Figure 5.5.5: *The normalized velocity of edge and screw dislocations in Mg, Ti, and Zr at a shear stress of* $\sigma = 0.055\mu$*, with respect to* T/T_m

Notice in Figure 5.5.5 how the screw dislocations glide with a greater normalized velocity than the edge dislocations. This explains why the shape of the loop from the FR source is oblong, with the screw portions of the loop traveling faster than the edge portions (See Figure 5.5.2 and 5.5.4). Also note that in this graph for $T/T_m > 0.2$ the screw plots velocity increases exponentially. This is because the leading partial breaks away from the trailing partial, which can be seen in Figure 5.5.4 (d) and (f), where the loop seems to smear out along the screw portions of the loop. This break-away of a leading partial from the trailing partial is something that J. A. Venables has explored as a potential source for deformation twinning in fcc materials [175], but to the extent of this author's knowledge it has not been observed or studied in hcp materials, until this work.

This simulation was re-run for Mg at the lower shear stress of $\sigma = 0.035\mu$ at T= 400K to see if breakaway occurred for the leading screw partial in a similar fashion as was observed at $\sigma = 0.055\mu$. We did not observe any breakaway of the leading partial for the leading screw dislocation at this lower stress, indicating the breakaway phenomenon is also stress dependent, in addition to being temperature and character dependent.

5.6 Conclusions

Implementation of the Langevin force equations into the PFDD model through the addition of a thermal noise term to the energy minimization equation is used to study temperature dependent dislocation behavior across materials. We find that the mobility of dissociated screw and edge dislocations in HCP materials on the pyramidal II plane have different temperature dependencies. Screw type dislocations glide with velocities increasingly greater than

edge dislocations as temperatures increase. When under a shear stress of $\sigma = 0.055\mu$ at temperatures $T/T_m \geq 0.2$ we observe for a pure screw dislocation a breakaway of the leading partial dislocation from the trailing partial, resulting in an increasing stacking fault width. This is the first time this author has observed this in HCP materials. The study of this breakaway leading partial in FCC materials and it's potential link to twinning [175] suggests that there could be a similar link in HCP worth further exploration. At lower stresses ($\sigma = 0.035\mu$) the temperature at which this breakaway occurs is higher, so the breakaway phenomenon is also stress dependent. With a greater understanding of how this breakaway phenomenon impacts deformation and material properties, there is potential to be able to turn it on and off as desired depending on the stress and temperature combination chosen.

When we considered a FR dislocation source we observed that the mixed character of the expanding dislocation loop under the shear stress of $\sigma = 0.055\mu$ held the screw portion of the leading partial from breaking away until nearing temperatures of $T/T_m = 0.5$. We also noticed that at every temperature tested, all subsequent dislocation loops from a FR source glide with the same time to loop formation after they have exceeded their critical bowing shape. The steady-state time to loop formation was calculated from the time of the first loop formation until the second loop formation. This means the amount of slip we could expect from a single FR source on a pyramidal II plane under stress will scale linearly over time for temperature $0 \leq T/T_m 0.5$.

All of this suggests that slip on the pyramidal II plane is strongly dependent on temperature, stress, and the majority character type for dislocation ensembles. It is no wonder then that dislocation behavior on the pyramidal II plane has been so much more difficult to study and understand than

dislocation behavior on the close-packed planes (basal or prismatic) in HCP materials. There is still much more to understand about dislocation slip along the pyramidal II plane and the overall deformation in HCP materials, but the addition of the Langevin thermal term to the PFDD model offers another layer of fruitful insight into the temperature dependencies of the dislocation mobilities that govern plasticity in materials.

Appendix

5.A Steady-state time to loop formation

By comparing (a) and (b) in Figure 5.5.3, we can also infer that the result of the first loop must in some way slow down the progression of the second dislocation bowing out from the FR source to the critical shape. Where the previous loop will always have a similar effect on the dislocation from emission to critical shape for every subsequent loop. Only the first loop would behave differently since there are no other loops interacting with it. From this we consider what the steady-state time to loop formation is for every loop after the first loop. We measure the time it takes from the first loop formation (Figure 5.5.2(e)) to the second loop formation (k). We have plotted this for each material in Figure 5.A.1 and we see that Ti and Zr act very similarly across all temperatures. They have very similar GSFE profiles (see Appendix 5.A). However, the GSFE curve for Mg is noticeably different, but for $T/T_m \geq 0.1$ the Mg plot aligns fairly well with those for Ti and Zr. The shear moduli (see Table 5.5.1) is a good estimation of the elastic differences between the materials, but if that were the reason for the differences in the steady-state time to loop formation we would expect to see some more variation between the three materials. So we have considered the lattice and elastic energy, two of the three energy terms from the Ginzburg-Landau equation. The

only remaining energetic consideration is the externally applied stress, the normalized value of which is the same in every simulation. More materials will need to be modeled to further explore the impact of the various energetics on steady-state time to loop formation.

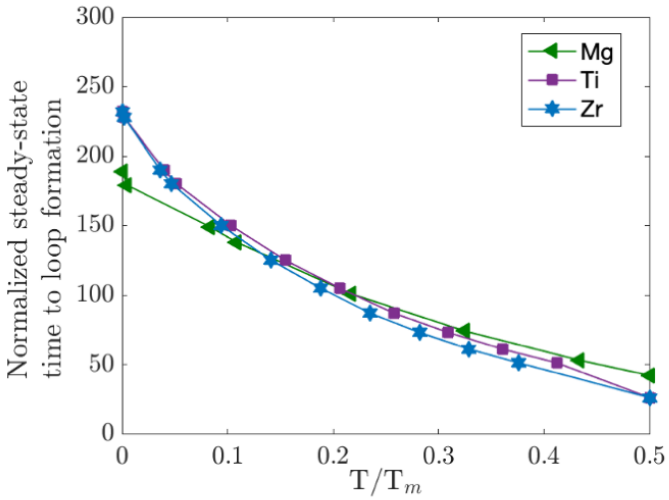

Figure 5.A.1: *The normalized steady-state time to loop formation for every subsequent loop after the first loop, plotted with respect to the normalized temperature. The steady-state time is measured from the time that the first loop is fully formed until the time that the second loop is fully formed (See Figure 5.5.2)*

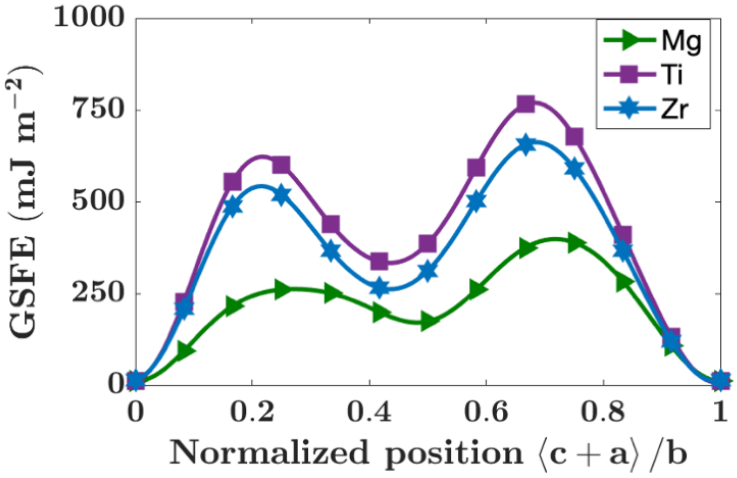

Figure 5.A.2: *GSFE curves for Mg, Ti, and Zr.*

5.B FR loop shape

Let τ be the number of timesteps that each snapshot has evolved, normalized by the number of timesteps per each output file, i.e. if we set our output files to capture every 10^{th} timestep ($i = 10$), then at $\tau = 5$, it is the 50^{th} timestep, and the amount of time that has actually passed is $t = \tau i \Delta t$. Consider Figure 5.B.2, which shows the loop evolution of a dislocation from a FR source on the pyramidal II plane in Zr at $T = 0K$. In this simulation $i = 50$, at $\tau = 192$ (e) the loop has fully separated from the FR source, and the amount of time that has actually passed is $t = \tau i \Delta t = 192 * 50 * 3.758 \times 10^{-18} s = 3.6077 \times 10^{-14} s$. At higher temperatures the "legs" of the FR dislocation loop feel the same attractive interaction energy due to one another as at $t = 0K$, however the resistance due to the lattice energy due to the unstable stacking fault energies in GSFE curves are more easily overcome when thermal fluctuations are accounted for. Thus the loop closes at a smaller shape at higher temperatures, which is what we see in 5.B.1.

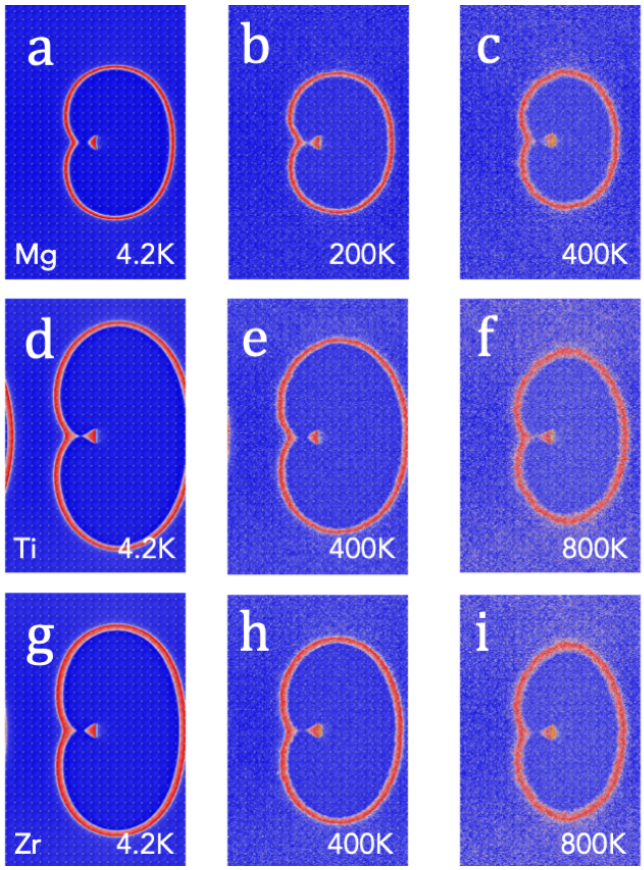

Figure 5.B.1: *Snapshots of the complete dislocation loop shape right after it separates from the FR source for each material Mg (a-c), Ti (d-f), Zr(g-i) at increasing temperatures.*

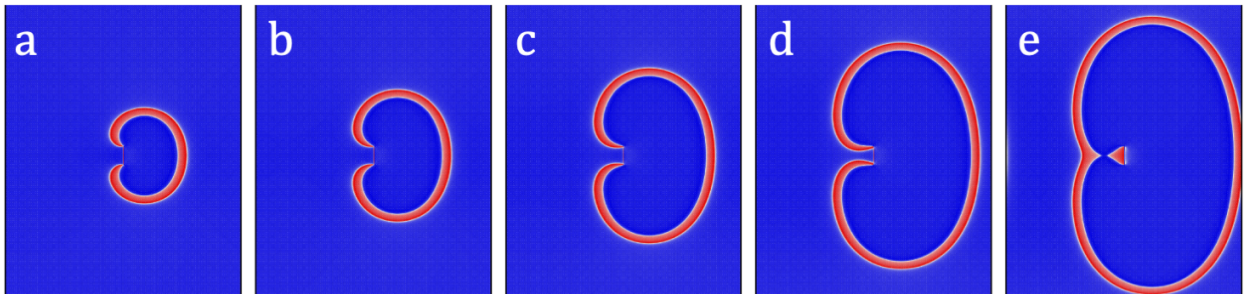

Figure 5.B.2: *Zr FR source at $T = 0K$, snapshots of the dislocation loop wrapping around the FR source creating "legs", dislocations with the same Burgers vector and opposite line sense, that experience an attractive interaction force due to one another. (a) is at τ =115, (b) 135, (c) 155, (d) 175.*

Chapter 6

Conclusions

This work spanned 6 years and followed the evolution and application of the phase field dislocation dynamics PFDD model through several code developments to account for 1) the lower symmetry of hexagonal close-packed HCP crystallography and its unique slip plane energetics, 2) elastic anisotropy, and 3) thermal fluctuations. This work explores dislocation dissociation, eSFW, mobility, dSFW, and morphology on the basal, prismatic and pyramidal II slip planes in HCP materials, taking a special focus on the relatively unstudied pyramidal-II plane. 10 different HCP materials are modeled over the course of this work, but special attention is given to understanding dislocations in Mg for its potential in lightweighting applications, as well as Ti and Zr which are also the more commonly studied of the HCP materials. The temperature dependencies of dislocation glide are studied by the addition of a stochastic thermal noise term to the energy minimization framework of the model.

The PFDD model is first extended to determine the properties of discrete dislocations belonging to all types of slip modes in the HCP crystal, such as the basal $\langle a \rangle$, prismatic $\langle a \rangle$, and pyramidal $\langle c + a \rangle$ slip modes [1]. The

dissociation simulations using the HCP PFDD method incorporate directly density functional theory DFT-calculated generalized stacking fault energy GSFE surfaces and curves for the different HCP slip planes and employ isotropic elasticity. The results demonstrated good agreement with available results from molecular statics MS, DFT, or experimental observations of dislocations structures in Mg.

In our deeper exploration of the pyramidal II plane, we employed an elastically anisotropic version of the PFDD approach [95], to compute the equilibrium structures of pyramidal-II $\langle c+a \rangle$ dislocations in ten HCP metals: Be, Co, Mg, Re, Ti, Zn, Cd, Hf, Y, and Zr. In all these metals, the $\langle c+a \rangle$ pyramidal dislocations dissociated into two partials that separate in plane, creating extended structures, with nm-sized splitting distances referred to as equilibrium stacking fault widths eSFW. The eSFWs for these 10 metals scale inversely with their normalized intrinsic stacking fault energy I from their GSFE curves. In most cases, the dislocation partial core widths and Burgers vectors were not ideally equal. These asymmetries in the dislocation structures are explained by deviations in the pyramidal II GSFE landscape from that expected of a metal with an ideal c/a ratio and symmetric landscape. Metals with higher levels of elastic anisotropy showed a wider separation distances (20–35%) for both screw and edge character dislocations than what is expected with effective isotropic constants.

The application of an external shear stress resulted in dislocations on the pyramidal II plane with dynamic stacking fault widths dSFW that are directionally dependent due to the asymmetries in GSFE curves and the decomposition of the Burgers vector. We explored this further by using a Frank-Read source to generate expanding dislocation loops. We considered both the basal and the pyramidal II plane and found the loop shape is dom-

inated by screw type sections to minimize the line tension energy of the expanding loop.

In our final PFDD development we derived the Langevin force equations for the phase field framework to account for thermal fluctuations at variable temperatures. This produced a thermal noise term that we added to the energy minimization equation in the PFDD model. This advanced PFDD model with thermal capabilities is then used to explore how temperature effects the time to dislocation loop formation from a Frank-Read FR source. We studied Mg, Ti, and Zr. We also looked at the velocity of infinitely long screw and edge type dislocations under the same applied shear stress. We find the leading partial for the screw dislocation "breaks away" at a greater velocity than the trailing partial at lower temperatures creating a growing dSFW. In the FR source simulations this resulted in the screw portions "smearing" out at higher temperatures. This breakaway phenomenon observed on the pyramidal II plane is both stress and temperature dependent.

All of this suggests that slip on the pyramidal II plane is strongly dependent on temperature, stress, and the majority character type for dislocation ensembles. It is no wonder then that c-axis deformation in HCP materials has been the hardest to predict and control in fabrication and application.

There is still much to be understood about HCP materials, especially so much more that can be explored about the activation of slip, dislocation morphology, and the competing dependencies on dislocation dynamics in the pyramidal II plane. However, with this more advanced and capable PFDD model we have a valuable tool to continue the work of expanding our understanding.

Chapter 7

Recommendations for future work

The PFDD model has been further advanced to account for the lower symmetry of HCP materials, parameterization of its unique slip planes, elastic anisotropy, and thermal fluctuations at variable temperatures. With these new advances to the PFDD model there are many promising possibilities for future applications. There is still so much to learn and understand about dislocation morphology and mobility in HCP materials especially on the pyramidal II plane. There are different set-ups and dislocation ensembles to explore. There are different materials to explore at different processing temperatures.

Circling back to the initial motivation in lightweighting with Mg alloys. We could used PFDD to paint more detail onto the picture linking the atomic/quantum energetics of a material with the dislocation dynamics that impact material properties (i.e. ductility, strength, and formability). We would need to use DFT to calculate the γ-surfaces or GSFE curves for the slip planes of interest in promising Mg alloys. If there is a novel material

with promising properties we could determine the stiffness tensor through experimentation. The PFDD model, accounting for the aforementioned energetics, could help us understand how dislocation mobility on each plane contributes to the (un)desireable properties through variable temperatures. If the material hasn't been successfully manufactured yet, we could also use DFT to best calculate the elastic stiffness tensor terms for input into the code, along with the lattice parameters (i.e. $\vec{a}$, $\vec{c}$, which are used to calculate important normalization constants in the PFDD code, such as, the Burgers vectors and inter-planar spacing). By analysing the dislocation dynamics on these theoretically possible materials, we can save material manufactures' time and money, by prioritizing manufacturing the novel materials that show the most promising dislocation dynamics in PFDD simulations for increased ductility. This would also require collaboration with larger scale modeling and experimentalists to better understand the connection between the PFDD observed dislocation mobility and morphology in each slip plane with the material properties. With PFDD linking the quantum/atomic energetics with the material properties, we can map out the ideal combination and ranges of material energetics that will produce a material with the desired material properties.

We can also use the PFDD model to explore various set-ups, different than the previously studied infinitely long dipole dislocations and the Frank-Read dislocation loop source. For example, we can study dislocation mobility through various fields of obstacles (i.e.inclusions). Is there some kind of combination between the favorable governing energetics in an alloy and a field of strategically placed obstacles where we can slow down dislocations on close-packed planes (i.e. basal, prismatic) without slowing down or better yet speeding up dislocation glide on the pyramidal II plane. This would increase

the number of independent active slip systems, meeting the requirements for plastic deformation.

Additionally, there are a number of PFDD applications beyond the pursuit of lightweighting with HCP materials. Dislocation dynamics can be modeled in any number of materials if we know the input energetics, slip planes, and lattice parameters for the material of interest. Group members Lauren Fey and Morgan Jones are currently using PFDD to study refractory multi-principal element alloys MPEAs, which are promising material candidates for high-temperature, high-strength applications [160, 176]. With our addition of the Langevin thermal noise term to the PFDD formulation, dislocation dynamics in these promising MPEAs can be studied at the various running temperatures for material applications.

Finally, if we combine the thermal noise term additions from this work with the additional PFDD advancements by other collaborators to model dislocation cross-slip, we can further explore the temperature dependency of dislocation cross-slip, which can have a significant impact on material properties. All of these PFDD model advancements make this a strong versatile tool for understanding the scalable physics the drive dislocation mediate plasticity.

References

[1] C. Albrecht, A. Hunter, A. Kumar, and I. J. Beyerlein. A phase field model for dislocations in hexagonal close packed crystals. *J. Mech. Phys. Solids*, 137:103823, 2020.

[2] Claire Albrecht, Anil Kumar, Shuozhi Xu, Abigail Hunter, and Irene J. Beyerlein. Asymmetric equilibrium core structures of pyramidal-II c + a dislocations in ten hexagonal-close-packed metals . *Physical Review Materials*, 5(4):43602, 2021.

[3] C. Shen and Y. Wang. Incorporation of γ-surface to phase field model of dislocation: simulating dislocation dissociation in fcc crystals. *Acta Mater.*, 52:683–691, 2004.

[4] M. M. Savin, V. M. Chernov, and A. M. Strokova. Energy factor of dislocations in hexagonal crystals. *Phys. Status Solidi A*, 35:747–754, 1976.

[5] Yanqing Su, Shuozhi Xu, and Irene J. Beyerlein. Density functional theory calculations of generalized stacking fault energy surfaces for eight face-centered cubic transition metals. *J. Appl. Phys.*, 126(10):105112, September 2019.

[6] Xiaowang Wang, Shuozhi Xu, Wu-Rong Jian, Xiang-Guo Li, Yanqing Su, and Irene J Beyerlein. Generalized stacking fault energies and peierls stresses in refractory body-centered cubic metals from machine learning-based interatomic potentials. *Comput. Mater. Sci.*, 192:110364, 2021.

[7] G. Simmons and H. Wang. *Single Crystal Elastic Constants and Calculated Aggregate Properties: A Handbook*. The M.I.T. Press, Cambridge, Massachusetts, 1971.

[8] ShunLi Shang, Hui Zhang, Swetha Ganeshan, and Zi-Kui. Liu. The development and application of a thermodynamic database for magnesium alloys. *JOM*, 60(12):45–47, 2008.

[9] Tresa M. Pollock. Weight loss with magnesium alloys. *Science*, 328:986–987, 2010.

[10] Z. Yang, J. P. Li, J. X. Zhang, G. W. Lorimer, and J. Robson. Review on Research and Development of Magnesium Alloys. *Acta Metallurgica Sinica (English Letters)*, 21(5):313–328, 2008.

[11] S. Sandlöbes, Z. Pei, M. Friák, L. F. Zhu, F. Wang, S. Zaefferer, D. Raabe, and J. Neugebauer. Ductility improvement of Mg alloys by solid solution: Ab initio modeling, synthesis and mechanical properties. *Acta Materialia*, 70:92–104, may 2014.

[12] P. G. Partridge. The crystallography and deformation modes of hexagonal close-packed metals. *Metall. Rev.*, 12(1):169–194, 1967.

[13] M.H. Yoo. Interaction of slip dislocations with twins in HCP metals. *Trans. Metall. Sco. AIME*, 245:2051–2060, 1969.

[14] N. Bertin, C. N. Tomé, I. J. Beyerlein, M. R. Barnett, and L. Capolungo. On the strength of dislocation interactions and their effect on latent hardening in pure magnesium. *International Journal of Plasticity*, 62:72–92, 2014.

[15] A. Kumar, B. Morrow, R. J. McCabe, and I. J. Beyerlein. An atomic-scale modeling and experimental study of $\langle c + a \rangle$ dislocations in Mg. *Mater. Sci. Eng. A*, 695:270–278, 2017.

[16] Z. Wu, M. F. Francis, and W. A. Curtin. Magnesium interatomic potential for simulating plasticity and fracture phenomena. *Modelling Simul. Mater. Sci. Eng.*, 23(1):1–19, 2015.

[17] B. Yin, Z. Wu, and W. A. Curtin. Comprehensive first-principles study of stable stacking faults in hcp metals. *Acta Mater.*, 123:223–234, 2017.

[18] J. P. Hirth and J. Lothe. *Theory of Dislocations*. McGraw-Hill, New York, 1968.

[19] J. A. Yasi, T. Nogaret, D. R. Trinkle, Y. Qi, G. Hector, and W. A. Curtin. Basal and prism dislocation cores in magnesium: Comparison of first-principles and embedded-atom-potential methods predictions. *Modelling and Simulation in Materials Science and Engineering*, 17(5), 2009.

[20] L. Shen, G. Proust, and G. Ranzi. An atomistic study of dislocation-solute interaction in mg-al alloys. *IOP Conference Series: Materials Science and Engineering*, 10(1), 2014.

[21] E. Clouet. Screw dislocation in zirconium: An ab initio study. *Physical Review B*, 86:144104, 2012.

[22] E. Clouet, D. Caillard, N. Chaari, F. Onimus, and D. Rodney. Dislocation locking versus easy glide in titanium and zirconium. *Nature Materials*, 14:931–936, 2015.

[23] C. Domain and A. Besson. Atomic-scale ab initio study of the zr-h system: Ii. interaction of h with plane defects and mechanical properties. *Acta Materialia*, 52:1495–1502, 2004.

[24] Y. Udagawa, M. Yamaguchi, T. Tsuru, H. Abe, and N. Sekimura. Effect of sn and nb on generalized stacking fault energy surfaces in zirconium and gamma hydride habit planes. *Philosophical Magazine*, 58:3927–3938, 2010.

[25] J. Wang, I. J. Beyerlein, and J. P. Hirth. Nucleation of elementary $\{\bar{1}011\}$ and $\{\bar{1}013\}$ twinning dislocations at a twin boundary in hexagonal close-packed crystals. *Modelling and Simulation in Materials Science and Engineering*, 20:024001, 2012.

[26] J. Wang, I. J. Beyerlein, and C. N. Tomé. Reactions of lattice dislocations with grain boundaries in mg: implications on the micro scale from atomic-scale. *International Journal of Plasticity*, 56:156–172, 2014.

[27] J. Wang and I. J. Beyerlein. Atomic structures of symmetric tilt grain boundaries in hexagonal close packed (hcp) crystals. *Modelling and Simulation in Materials Science and Engineering*, 20:024002, 2012.

[28] L. Capolungo, I. J. Beyerlein, and Z. Q. Wang. The role of elastic anisotropy on plasticity in hcp metals: a three-dimensional dislocation dynamics study. *Modelling and Simulation in Materials Science and Engineering*, 18:085002, 2010.

[29] R. Wang, S. F. Wang, X. Z. Wu, and Q. Y. Wei. First-principles determination of dislocation properties in magnesium based on the improved peierls-nabarro equation. *Physica Scripta*, 81(6), 2010.

[30] L. Cao, A. Hunter, I. J. Beyerlein, and M. Koslowski. The role of partial mediated slip during quasi-static deformation of 3D nanocrystalline metals. *J. Mech. Phys. Solids*, 78:415–426, 2015.

[31] I. J. Beyerlein and A. Hunter. Understanding dislocation mechanics at the mesoscale using phase field dislocation dynamics. *Philos. Trans. R. Soc. A*, 374:20150166, 2016.

[32] A. Hunter, B. Leu, and I. J. Beyerlein. A review of slip transfer: applications of mesoscale techniques. *Journal of Materials Science*, 53:5584–5603, 2018.

[33] Y Wang and J. Li. Phase field modeling of defects and deformation. *Acta Materialia*, 58:1212–1235, 2010.

[34] I. Steinbach. Phase-field models in materials science. *Modelling and Simulation in Materials Science and Engineering*, 17:073001, 2009.

[35] B. Svendsen, P. Shanthraj, and D. Raabe. Finite-deformation phase-field chemomechanics for multiphase, multicomponent solids. *Journal of the Mechanics and Physics of Solids*, 112:619–636, 2018.

[36] J. W. Cahn and J. E. Hilliard. Free energy as a non-uniform system. i. interfacial energy. *Journal of Chemical Physics*, 28:258–267, 1958.

[37] L. Lei, J. L. Marian, and M. Koslowski. Phase-field modeling of defect nucleation and propagation in domains with material inhomo-

geneities. *Modelling and Simulation in Materials Science and Engineering*, 21(025009):1–15, 2013.

[38] Y. Zeng, A. Hunter, I. J. Beyerlein, and M. Koslowski. A phase field dislocation dynamics model for a bicrystal interface system: An investigation into dislocation slip transmission across cube-on-cube interfaces. *International Journal of Plasticity*, 79:293–313, 2016.

[39] A. Hunter and I. J. Beyerlein. Relationship between monolayer stacking faults and twins in nanocrystals. *Acta Mater.*, 88:207–217, 2015.

[40] D. Qiu, P. Zhao, C. Shen, W. Lu, D. Zhang, M. Mrovec, and Y. Wang. Predicting grain boundary structure and energy in bcc metals by integrated atomistic and phase-field modeling. *Acta Materialia*, 164:799–809, 2019.

[41] X. Peng, N. Mathew, I. J. Beyerlein, K. Dayal, and A. Hunter. A 3D phase field dislocation dynamics model for body-centered cubic crystals. *Comput. Mater. Sci.*, 171:109217, 2020.

[42] M. A. Louchez, L. Thuinet, R. Besson, and A. Legris. Microscopic phase-field modeling of hcp—fcc interfaces. *Computational Materials Science*, 132:62–73, 2017.

[43] P. Zhao, C. Shen, M. F. Savage, J. Li, S. R. Niezgoda, M. J. Mills, and Y. Wang. Slip transmission assisted by Shockley partials across α/β interfaces in Ti-alloys. *Acta Mater.*, 171:291–305, 2019.

[44] M. Knezevic, I. J. Beyerlein, T. A. Sisneros, and C. N. Tomé. A polycrystal plasticity model for predicting mechanical response and texture evolution during strain-path changes: Application to beryllium. *Int. J. Plast.*, 49:185–198, 2013.

[45] E. Cerreta, C. A. Yablinsky, G. T. Gray III, S. V. Vogel, and D. W. Brown. The influence of grain size and texture on the mechanical response of high purity hafnium. *Mater. Sci. Eng. A*, 456(1-2):243–251, 2007.

[46] L. B. Addessio, E. K. Cerreta, and G. T. Gray III. Mechanical behavior of zirconium and hafnium in tension and compression. *Metall. Mater. Trans. A*, 36A:2893–2903, 2005.

[47] S. I. Choi and J. H. Kim. Radiation-induced dislocation and growth behavior of zirconium and zirconium alloys - A review. *Nucl. Eng. Tech.*, 45(3):385–392, 2013.

[48] Y. Q. Guo, S. H. Zhang, I. J. Beyerlein, D. Legut, S. L. Shang, Z. K. Liu, and R. F. Zhang. Synergetic effects of solute and strain in bio-compatible Zn-based and Mg-based alloys. *Acta Mater.*, 181:423–438, 2019.

[49] I. J. Beyerlein, X. Zhang, and A. Misra. Growth twins and deformation twins in metals. *Ann. Rev. Mater. Res.*, 44:329–363, 2014.

[50] D. Coutsouradis, A. Davin, and M. Lamberigts. Cobalt-based superalloys for applications in gas turbines. *Mater. Sci. Eng.*, 88:11–19, 1987.

[51] J. K. Tien, T. E. Howson, G. L. Chen, and X. S. Xie. Cobalt availability and superalloys. *JOM*, 32:12–20, 1980.

[52] T. Obara, H. Yoshinga, and S. Morozumi. $11\bar{2}2\langle 1123\rangle$ Slip system in magnesium. *Acta Metall.*, 21(7):845–853, July 1973.

[53] M. Zecevic, I. J. Beyerlein, and M. Knezevic. Activity of pyramidal I and II $\langle c+a \rangle$ slip in Mg alloys as revealed by texture development. *J. Mech. Phys. Solids*, 111:290–307, 2018.

[54] Hideki Tonda and Shinji Ando. Effect of temperature and shear direction on yield stress by $11\bar{2}2\langle\bar{1}\bar{1}23\rangle$ slip in HCP metals. *Metall. Mat. Trans. A*, 33(3):831–836, March 2002.

[55] Cynthia M. Byer, Bin Li, Buyang Cao, and K. T. Ramesh. Microcompression of single-crystal magnesium. *Scr. Mater.*, 62(8):536–539, April 2010.

[56] Shinji Ando and Hideki Tonda. Non-basal slip in magnesium-lithium alloy single crystals. *Mater. Trans.*, 41(9):1188–1191, 2000.

[57] Z. Ding, W. Liu, H. Sun, S. Li, D. Zhang, Y. Zhao, E. J. Lavernia, and Y. Zhu. Origins and dissociation of pyramidal $\langle c+a \rangle$ dislocations in magnesium and its alloys. *Acta Mater.*, 146:265–272, 2018.

[58] Q. Yu, L. Qi, R. K. Mishra, J. Li, and A. M. Minor. Reducing deformation anisotropy to achieve ultrahigh strength and ductility in Mg at the nanoscale. *Proc. Natl. Acad. Sci. USA*, 110(33):13289–13293, 2013.

[59] M. A. Kumar and I. J. Beyerlein. Local microstructure and micromechanical stress evolution during deformation twinning in hexagonal polycrystals. *J. Mater. Res.*, 35(3):217–241, 2020.

[60] M.H. Yoo. Slip, twinning, and fracture in hexagonal close-packed metals. *Metall. Trans. A*, 12A:409–418, 1981.

[61] N. J. Kim. Critical Assessment 6: Magnesium sheet alloys: viable alternatives to steels? *Mater. Sci. Tech.*, 30(15):1925–1928, 2014.

[62] B.-C. Shuh, M. S. Shim, K. S. Shin, and N. J. Kim. Current issues in magnesium sheet alloys: Where do we go from here? *Scr. Mater.*, 84-85:1–6, 2014.

[63] J. P. Hirth and J. Lothe. *Theory of Dislocations*. Krieger Pub. Co., Florida, second edition, 1982.

[64] J. Han, S. L. Thomas, and D. J. Srolovitz. Grain-boundary kinetics: A unified approach. *Progress in Material Sciences*, 98:386–476, 2018.

[65] M. A. Meyers, A. Mishra, and D. J. Benson. Mechanical properties of nanocrystalline materials. *Progress in Material Sciences*, 51:427–556, 2006.

[66] M. H Yoo, S. R Agnew, J. R Morris, and K. M Ho. Non-basal slip systems in HCP metals and alloys: source mechanisms. *Mater. Sci. Eng. A*, 319-321:87–92, December 2001.

[67] Y. Tang and J. A. El-Awady. Formation and slip of pyramidal dislocations in hexagonal close-packed magnesium single crystals. *Acta Mater.*, 71:319–332, 2014.

[68] S. Sandlöbes, M. Friák, S. Zaefferer, A. Dick, S. Yi, D. Letzig, Z. Pei, L. F. Zhu, J. Neugebauer, and D. Raabe. The relation between ductility and stacking fault energies in Mg and Mg-Y alloys. *Acta Mater.*, 60(6):3011–3021, April 2012.

[69] M. Itakura, H. Kaburaki, M. Yamaguchi, and T. Tsuru. Novel cross-slip mechanism of pyramidal screw dislocations in magnesium. *Phys. Rev. Lett.*, 116:225501, 2016.

[70] D. Buey, L. G. Hector Jr., and M. Ghazisaeidi. Core structure and solute strengthening of second-order pyramidal $\langle c + a \rangle$ dislocations in Mg-Y alloys. *Acta Mater.*, 147:1–9, 2018.

[71] D. H. Kim, F. Ebrahimi, M. V. Manuel, J. S. Tulenko, and S. R. Phillpot. Grain-boundary activated pyramidal dislocations in nano-textured Mg by molecular dynamics simulation. *Mater. Sci. Eng. A*, 528(16-17):5411–5420, 2011.

[72] R. L. Bell and R. W. Cahn. The dynamics of twinning and the interrelation of slip and twinning in zinc crystals. *Proc. R. Soc. A*, 239(1219):494–521, 1957.

[73] S. Mendelson. Dislocation dissociations in hcp metals. *J. Appl. Phys.*, 41(5):1893–1910, 1970.

[74] K. Yaddanapudi, B. Leu, M. A. Kumar, X. Wang, J. M. Schoenung, E. J. Lavernia, T. Rupert, I. J. Beyerlein, and S. Mahajan. Accommodation and formation of $\{\bar{1}012\}$ twin tips in an Mg-Y alloys. *Acta Mater.*, 204:116514, 2021.

[75] Y. Dou and J. Zhang. Effects of structural relaxation on the generalized stacking fault energies of hexagonal-close-packed system from first-principles calculations. *Comput. Mater. Sci.*, 98(15):405–409, 2015.

[76] P. Kwaśniak, P. Śpiewak, H. Garbacz, and K. J. Kurzydłowski. Plasticity of hexagonal systems: Split slip modes and inverse Peierls relation in α-Ti. *Phys. Rev. B*, 89:144105, 2014.

[77] M. Ardeljan, D. J. Savage, A. Kumar, I. J. Beyerlein, and M. Knezevic. The plasticity of highly oriented nano-layered Zr/Nb composites. *Acta Mater.*, 115:189–203, 2016.

[78] Anil Kumar, M. Arul Kumar, and Irene J. Beyerlein. First-principles study of crystallographic slip modes in ω-Zr. *Scientific Reports*, 7(1), dec 2017.

[79] B. Syed, J. Geng, R. K. Mishra, and K. S. Kumar. [0001] Compression response at room temperature of single-crystal magnesium. *Scr. Mater.*, 67(7):700–703, October 2012.

[80] K. Y. Xie, Z. Alam, A. Caffee, and K. J. Hemker. Pyramidal I slip in c-axis compressed Mg single crystals. *Scr. Mater.*, 112:75–78, 2016.

[81] J. F. Stohr and J. P. Poirier. Etude en microscopie electronique du glissement pyramidal $\{1122\}\langle 1123\rangle$ dans le magnesium. *Philos. Mag.*, 25(6):1313–1329, 1972.

[82] F. Long, M. R. Daymond, Z. Yao, and M. A. Kirk. Deformation mechanism study of hot rolled Zr-2.5Nb alloy by transmission electron microscopy. II. *In situ* transmission electron microscopy study of deformation mechanism change of a Zr-2.5Nb alloy upon heavy ion irradiation. *J. Appl. Phys.*, 117:104302, 2015.

[83] F. Long, L. Balogh, and M. R. Daymond. Evolution of dislocation density in a hot rolled Zr-2.5Nb alloy with plastic deformation studied by neutron diffraction and transmission electron microscopy. *Philos. Mag.*, 97(31):2888–2914, 2017.

[84] F. Long, J. Kacher, Z. Yao, and M. R. Daymond. A tomographic TEM study of tension-compression asymmetry response of pyramidal dislocations in a deformed Zr-2.5Nb alloy. *Scr. Mater.*, 153:94–98, 2018.

[85] Y. Minonishi, S. Morozumi, and H. Yoshinaga. $\{1122\}$ $\langle 1123\rangle$ slip in titanium. *Scr. Metall.*, 16(4):427–430, 1982.

[86] K. Kishida, J. G. Kim, T. Nagae, and H. Inui. Experimental evaluation of critical resolved shear stress for the first-order pyramidal c+a slip in commercially pure Ti by micropillar compression method. *Acta Mater.*, 196:168–174, 2020.

[87] H. Fan and J. A. El-Awady. Towards resolving the anonymity of pyramidal slip in magnesium. *Mater. Sci. Eng. A*, 644:318–324, 2015.

[88] J. Geng, M. F. Chisholm, R. K. Mishra, and K. S. Kumar. An electron microscopy study of dislocation structures in Mg single crystals compressed along [0001] at room temperature. *Philos. Mag.*, 95(35):3910–3932, 2015.

[89] Y. U. Wang, Y. M. Jin, A. M. Cuitiño, and A. G. Khachaturyan. Nanoscale phase field microelasticity theory of dislocations: model and 3D simulations. *Acta Mater.*, 49:1847–1857, 2001.

[90] M. Koslowski, A. Cuitiño, and M. Ortiz. A phase-field theory of dislocations dynamics, strain hardening and hysteresis in ductile single crystals. *J. Mech. Phys. Solids*, 50(12):2597–2635, 2002.

[91] Vasily V. Bulatov and Efthimios Kaxiras. Semidiscrete variational Peierls framework for dislocation core properties. *Phys. Rev. Lett.*, 78(22):4221–4224, June 1997.

[92] G. Schoeck. The generalized Peierls-Nabarro model. *Philos. Mag. A*, 69(6):1085–1095, 1994.

[93] Y. Wang and J. Li. Phase field modeling of defects and deformation. *Acta Mater.*, 58(4):1212–1235, 2010.

[94] S. Xu, J. R. Mianroodi, A. Hunter, I. J. Beyerlein, and B. Svendsen. Phase-field-based calculations of the disregistry fields of static extended dislocations in FCC metals. *Philos. Mag.*, 99(11):1400–1428, 2019.

[95] Shuozhi Xu, Yanqing Su, and Irene J. Beyerlein. Modeling dislocations with arbitrary character angle in face-centered cubic transition metals using the phase-field dislocation dynamics method with full anisotropic elasticity. *Mech. Mater.*, 139:103200, December 2019.

[96] Shuozhi Xu, Yanqing Su, Lauren T. W. Smith, and Irene J. Beyerlein. Frank-Read source operation in six body-centered cubic refractory metals. *J. Mech. Phys. Solids*, 141:104017, 2020.

[97] B. L. Mordike and T. Ebert. Magnesium Properties - applications - potential. *Materials Science and Engineering A*, 302(1):37–45, apr 2001.

[98] V. V. Ogarevic and R. I. Stephens. Fatigue of magnesium alloys. *Annual Review of Materials Science*, 20(1):141–177, 1990.

[99] Gi Dong Sim, Kelvin Y. Xie, Kevin J. Hemker, and Jaafar A. El-Awady. Effect of temperature on the transition in deformation modes in Mg single crystals. *Acta Materialia*, 178:241–248, oct 2019.

[100] Sean R. Agnew. Wrought magnesium: A 21st century outlook. *JOM*, 56(5):20–21, 2004.

[101] Bud Caesar Wonsiewicz and W.A. Backofen. PLASTICITY OF MAGNESIUM CRYSTALS. *T. Metall. Soc. Aime*, 239(9):1422–1431, 1967.

[102] Shinji Ando, Masayuki Tsushida, and Hiromoto Kitahara. Deformation Behavior of Magnesium Single Crystal in c-Axis Compression and a-Axis Tension. *Materials Science Forum*, 654-656:699–702, 2010.

[103] J. W. Christian and S. Mahajan. Deformation twinning. *Progress in Material Sciences*, 39:1–157, 1995.

[104] Hideo Yoshinaga and Ryo Horiuchi. On the Nonbasal Slip in Magnesium Crystals. *Transactions of the Japan Institute of Metals*, 5(1):14–21, 1964.

[105] Adrien Chapuis and Julian H. Driver. Temperature dependency of slip and twinning in plane strain compressed magnesium single crystals. *Acta Materialia*, 59(5):1986–1994, mar 2011.

[106] M. H. Yoo, J. R. Morris, K. M. Ho, and S. R. Agnew. Nonbasal deformation modes of HCP metals and alloys: Role of dislocation source and mobility. *Metallurgical and Materials Transactions A: Physical Metallurgy and Materials Science*, 33(3):813–822, 2002.

[107] T. Obara, H. Yoshinga, and S. Morozumi. {1122}1123 Slip system in magnesium. *Acta Metallurgica*, 21(7):845–853, jul 1973.

[108] A. Hunter and I. J. Beyerlein. Predictions of an alternative pathway for grain-boundary driven twinning. *Applied Physics Letters*, 104(233112):1–4, 2014.

[109] A. Hunter and I. J. Beyerlein. Unprecedented grain size effect on stacking fault width. *Applied Physics Letters Materials*, 1(032109):1–9, 2013.

[110] J. R. Mianroodi and B. Svendsen. Atomistically determined phase-field modeling of dislocation dissociation, stacking fault formation, disloca-

tion slip, and reactions in fcc systems. *J. Mech. Phys. Solids*, 77:109–122, 2015.

[111] J. R. Mianroodi, A. Hunter, I. J. Beyerlein, and B. Svendsen. Theoretical and computational comparison of models for dislocation dissociation and stacking fault/core formation in fcc systems. *J. Mech. Phys. Solids*, 95:719–741, 2016.

[112] Z. P. Pi, Q. H. Fang, C. Jiang, B. Liu, Y. Liu, P. H. Wen, and Y. W. Liu. Stress dependence of the dislocation core structure and loop nucleation for face-centered-cubic metals. *Acta Materialia*, 131:380–390, 2017.

[113] A. Hunter, I. J. Beyerlein, T. C. Germann, and M. Koslowski. Infuence of the stacking fault energy surface on partial dislocations in fcc metals with a three-dimensional phase field model. *Physical Review B*, 84(144108):1–10, 2011.

[114] C. Shen and Y. Wang. Phase field model of dislocation networks. *Acta Mater.*, 51:2595–2610, 2003.

[115] G. Schoeck. The core structure, recombination energy and Peierls energy for dislocations in Al. *Philosophical Magazine A*, 81(5):1161–1176, 2001.

[116] A. Hunter, R. F. Zhang, and I. J. Beyerlein. The core structure of dislocation and their relationship to the material γ-surface. *J. Appl. Phys.*, 115:134314, 2014.

[117] V. Vitek. Intrinsic stacking faults in body-centered cubic crystals. *Philosophical Magazine*, 18(154):773–786, 1968.

[118] G. Schoeck. The peierls model: Progress and limitations. *Materials Science and Engineering A*, 400-401:7–17, 2005.

[119] G. Lu, N. Kioussis, V. V. Bulatov, and E. Kaxiras. Generalized-stacking-fault energy surface and dislocation properties of aluminum. *Physical Review B*, 62(5):3099–3108, 2000.

[120] E. Kaxiras and M. S. Duesbery. Free energies of generalized stacking faults in si and implications for the brittle-ductile transition. *Physical Review Letters*, 70(24):3752–3755, 1993.

[121] S. L. Shang, W. Y. Wang, B. C. Zhou, Y. Wang, K. A. Darling, L. J. Kecskes, S. N. Mathaudhu, and Z. K. Liu. Generalized stacking fault energy, ideal strength and twinnability of dilute mg-based alloys: A first-principles study of shear deformation. *Acta Materialia*, 67:168–180, 2014.

[122] Z. Pei, L.-F. Zhu, M. Friak, S. Snadlobes, J. von Pezold, H.W. Sheng, C.P. Race, S. Zaefferer, B. Svendsen, D. Raabe, and J. Neugebauer. Ab initio and atomistic study of generalized stacking fault energies in mg and mg-y alloys. *New Journal of Physics*, 15:043020, 2013.

[123] C. Domain. Ab initio modelling of defect properties with substitutional and interstitials elements in steels and zr alloys. *Journal of Nuclear Materials*, 351:1–19, 2006.

[124] M. Ardeljan, M. Knezevic, M. Jain, S. Pathak, A. Kumar, N. Li, N. A. Mara, J. K. Baldwin, and I. J. Beyerlein. Room temperature deformation mechanism of Mg/Nb nanolayered composites. *J. Mater. Res.*, 33(10):1311–1332, 2018.

[125] D. Rodney, L. Ventelon, E. Clouet, L. Pizzagalli, and F. Willaime. Ab initio modeling of dislocation core properties in metals and semiconductors. *Acta Materialia*, 124:663–659, 2017.

[126] G. Kresse and J. Furthmüller. Efficiency of ab initio total energy calculations for metals and semiconductors using a plane-wave basis set. *Comput. Mater. Sci.*, 6(1):15–50, 1996.

[127] G. Kresse and J. Furthmüller. Efficient iterative schemes for ab initio total-energy calculations using a plane-wave basis set. *Phys. Rev. B*, 54(16):11169–11186, 1996.

[128] J. P. Perdew, K. Burke, and M. Ernzerhof. Generalized gradient approximation made simple. *Phys. Rev. Lett.*, 77(18):3865–3868, 1996.

[129] R. Hill. The elastic behavior of a crystalline aggregate. *Proceedings of the Physical Society Section A*, 65:349–354, 1952.

[130] The MathWorks, Inc., Natick, Massachusetts, United States. *MATLAB and Curve Fitting Toolbox Release*, 2016b.

[131] M. S. Daw and M. I. Baskes. Embedded-atom method: Derivation and application to impurities, surfaces, and other defects in metals. *Physical Review B*, 29(12):6443–6453, 1984.

[132] T. W. Fan, Q. Zhang, L. Ma, P. Y. Tang, B. Y. Tang, L. M. Peng, and W. J. Ding. First-principles study of the dislocation core structures on basal plane in magnesium. *European Journal of Mechanics, A/Solids*, 45:1–7, 2014.

[133] S. Groh, E. B. Marin, M. F. Horstemeyer, and D. J. Bammann. Dislocation motion in magnesium: A study by molecular statics and molec-

ular dynamics. *Modelling and Simulation in Materials Science and Engineering*, 17(7), 2009.

[134] S. Naka, A. Lasalmonie, P. Costa, and L.P. Kubin. The low-temperature plastic deformation of titanium and the core structure of a-type screw dislocations. *Philosophical Magazine A*, 57(5):717–740, 1988.

[135] S. Farenc, D. Caillard, and A. Couret. An in situ study of prismatic glide in titanium at low temperatures. *Acta Metallurgica et Materialia*, 41(9):2701–2709, 1993.

[136] S. Farenc, D. Caillard, and A. Couret. A new model for the peak of activation area of titanium. *Acta Metallurgica et Materialia*, 43(10):3669–3678, 1995.

[137] M. Ghazisaeidi, L. G. Hector, and W. A. Curtin. First-principles core structures of $\langle c + a \rangle$ edge and screw dislocations in Mg. *Scr. Mater.*, 75:42–45, 2014.

[138] I. J. Beyerlein and J. Wang. Interface-driven mechanisms in cubic/noncubic nanolaminates at different scales. *MRS Bulletin*, 44:31–39, 2019.

[139] J. Wang, Q. Yu, Y. Jiang, and I. J. Beyerlein. Twinning-associated boundaries in hexagonal close-packed metals. *Journal of the Minerals, Metals and Materials Society*, 66:95–101, 2014.

[140] J. Wang, S. K. Yadav, C. N. Hirth, C. N. Tomé, and I. J. Beyerlein. Pure-shuffle nucleation of deformation twins in hexagonal-close-packed metals. *Materials Research Letters*, 1:126–132, 2013.

[141] J. Wang and I. J. Beyerlein. Atomic structures of [1011] symmetric tilt grain boundaries in hexagonal close packed (hcp) crystals. *Metallurgical and Materials Transactions A*, 43:3556–3569, 2012.

[142] L. Capolungo and I. J. Beyerlein. Nucleation and stability of twins in hcp metals. *Physical Review B*, 78:024117, 2010.

[143] I. J. Beyerlein, J. Wang, M. R. Barnett, and C. N. Tomé. Double twinning mechanisms in magnesium alloys via dissociation of lattice dislocations. *Proc. R. Soc. A*, 468:1496–1520, 2012.

[144] Yanqing Su, Milan Ardeljan, Marko Knezevic, Manish Jain, Siddhartha Pathak, and Irene J. Beyerlein. Elastic constants of pure body-centered cubic Mg in nanolaminates. *Comput. Mater. Sci.*, 174:109501, March 2020.

[145] Shuozhi Xu, Emily Hwang, Wu-Rong Jian, Yanqing Su, and Irene J Beyerlein. Atomistic calculations of the generalized stacking fault energies in two refractory multi-principal element alloys. *Intermetallics*, 124:106844, 2020.

[146] D. Chiba, S. Fukami, K. Shimamura, N. Ishiwata, K. Kobayashi, and T. Ono. Electrical control of the ferromagnetic phase transition in cobalt at room temperature. *Nature Mater.*, 10(3):853–856, 2011.

[147] Jia-An Yan, Chong-Yu Wang, and Shan-Ying Wang. Generalized-stacking-fault energy and dislocation properties in bcc Fe: A first-principles study. *Phys. Rev. B*, 70(17):174105, November 2004.

[148] S. Xu, J. R. Mianroodi, A. Hunter, B. Svendsen, and I. J. Beyerlein. Comparative atomistic and continuum modeling of the disregistry and

Peierls stress for dissociated edge and screw dislocations in Al. *Int. J. Plast.*, 129:102689, 2020.

[149] Z. Wu, B. Yin, and W. A. Curtin. Energetics of dislocation transformations in hcp metals. *Acta Mater.*, 119:203–217, 2016.

[150] Christopher M. Kube. Elastic anisotropy of crystals. *AIP Adv.*, 6(9):095209, September 2016.

[151] U. F. Kocks, C. N. Tomé, and H.-R. Wenk. *Texture and Anisotropy: Preferred Orientations in Polycrystals and their Effect on Materials Properties*. Cambridge University Press, Cambridge, August 2008.

[152] L. Wang, Y. Yang, P. Eisenlohr, T. R. Bieler, M. A. Crimp, and D. E. Mason. Twin nucleation by slip transfer across grain boundaries in commercial purity titanium. *Metallurgical and Materials Transactions A*, 41A(2):412–430, 2010.

[153] Seong Gyoon Kim, Won Tae Kim, and Toshio Suzuki. Phase-field model for binary alloys. *Physical review e*, 60:7186, 1999.

[154] Ingo Steinbach. Phase-field model for microstructure evolution at the mesoscopic scale. *Annual Review of Materials Research*, 43:89–107, 2013.

[155] Mahmood Mamivand, Mohsen Asle Zaeem, and Haitham El Kadiri. A review on phase field modeling of martensitic phase transformation. *Computational Materials Science*, 77:304–311, 2013.

[156] Long-Qing Chen. Phase-field models for microstructure evolution. *Annual review of materials research*, 32:113–140, 2002.

[157] J P Simmons, Youhai Wen, C Shen, and Y Z Wang. Microstructural development involving nucleation and growth phenomena simulated with the phase field method. *Materials Science and Engineering: A*, 365:136–143, 2004.

[158] Charlotte Kuhn and Ralf Müller. A continuum phase field model for fracture. *Engineering Fracture Mechanics*, 77:3625–3634, 2010.

[159] Lauren T W Fey, Abigail Hunter, and Irene J Beyerlein. Phase-field dislocation modeling of cross-slip. *Journal of Materials Science*, 2022.

[160] L. T. W. Smith, Y. Su, S. Xu, A. Hunter, and I. J. Beyerlein. The effect of local chemical ordering on Frank-Read source activation in a refractory multi-principal element alloy. *Int. J. Plast.*, 134:102850, 2020.

[161] Hui Zheng, Lauren T W Fey, Xiang-Guo Li, Yong-Jie Hu, Liang Qi, Chi Chen, Shuozhi Xu, Irene J Beyerlein, and Shyue Ping Ong. Multi-scale investigation of chemical short-range order and dislocation glide in the monbti and tanbti refractory multi-principal element alloys. *arXiv preprint arXiv:2203.03767*, 2022.

[162] Y. Shen and P. M. Anderson. Transmission of a screw dislocation across a coherent, non-slipping interface. *Journal of the Mechanics and Physics of Solids*, 55:956–979, 2007.

[163] C. Shen, J. P. Simmons, and Y. Wang. Effect of elastic interaction on nucleation: II. Implementation of strain energy of nucleus formation in the phase field method. *Acta Materialia*, 55(4):1457–1466, feb 2007.

[164] Y. Wang and A. G. Khachaturyan. Three-dimensional field model and computer modeling of martensitic transformations. *Acta Materialia*, 45(2):759–773, 1997.

[165] Tetsu Ichitsubo and Katsushi Tanaka. Thermal fluctuation for the time-dependent Ginzburg-Landau simulation. *Physical Review E - Statistical Physics, Plasmas, Fluids, and Related Interdisciplinary Topics*, 63(6):1–4, 2001.

[166] Nele Moelans, Bart Blanpain, and Patrick Wollants. An introduction to phase-field modeling of microstructure evolution. *Calphad: Computer Coupling of Phase Diagrams and Thermochemistry*, 32(2):268–294, 2008.

[167] E. Martinez, J. Marian, A. Arsenlis, M. Victoria, and J.M. Perlado. Atomistically informed dislocation dynamics in fcc crystals. *Journal of the Mechanics and Physics of Solids*, 56:869–895, 2008.

[168] Hazime Mori. Transport, Collective Motion, and Brownian Motion. *Progress of Theoretical Physics*, 33(3), 1965.

[169] Robert Zwanzig. *NONEQUILIBRIUM STATISTICAL MECHANICS*. Oxford University Press, New York, 2001.

[170] Alain Karma and Wouter Jan Rappel. Phase-field model of dendritic sidebranching with thermal noise. *Physical Review E - Statistical Physics, Plasmas, Fluids, and Related Interdisciplinary Topics*, 60(4 A):3614–3625, 1999.

[171] Kyozi Kawasaki. Simple derivation of generalized linear and nonlinear Langevin equations. *Journal of Physics A: Mathematical, Nuclear, and General*, 6:1289, 1973.

[172] Irwin Oppenheim. The Langevin equation with applications in physics, chemistry and electrical engineering. *Journal of Statistical Physics*, 88(1-2):519–520, 1997.

[173] D. Rönnpagel, Th. Streit, and Th. Pretorius. Including Thermal Activation in Simulation Calculations of Dislocation Glide. *Physica Status Solidi (a)*, 135(2):445–454, feb 1993.

[174] Daniel N. Blaschke. Properties of dislocation drag from phonon wind at ambient conditions. *Materials*, 16(6), 2019.

[175] J. A. Venables. The electron microscopy of deformation twinning. *Journal of Physics and Chemistry of Solids*, 25(7):685–692, 1964.

[176] Lauren T W Smith, Shuozhi Xu, Yanqing Su, Abigail Hunter, and Irene J Beyerlein. Multi-Modal Glide of Dislocations in a Refractory Multi-Principal Element Alloy.